EUROPEAN ORGANIZATION FOR NUCLEAR RESEARCH

The exotic meson $\pi_1(1600)$ with $J^{PC} = 1^{-+}$ and its decay into $\rho(770)\pi$

The COMPASS Collaboration

Abstract

We study the spin-exotic $J^{PC} = 1^{-+}$ amplitude in single-diffractive dissociation of $190\,\text{GeV}/c$ pions into $\pi^-\pi^-\pi^+$ using a hydrogen target and confirm the $\pi_1(1600) \to \rho(770)\pi$ amplitude, which interferes with a nonresonant 1^{-+} amplitude. We demonstrate that conflicting conclusions from previous studies on these amplitudes can be attributed to different analysis models and different treatment of the dependence of the amplitudes on the squared four-momentum transfer and we thus reconcile their experimental findings. We study the nonresonant contributions to the $\pi^-\pi^-\pi^+$ final state using pseudo-data generated on the basis of a Deck model. Subjecting pseudo-data and real data to the same partial-wave analysis, we find good agreement concerning the spectral shape and its dependence on the squared four-momentum transfer for the $J^{PC} = 1^{-+}$ amplitude and also for amplitudes with other J^{PC} quantum numbers. We investigate for the first time the amplitude of the $\pi^-\pi^+$ subsystem with $J^{PC} = 1^{--}$ in the 3π amplitude with $J^{PC} = 1^{-+}$ employing the novel freed-isobar analysis scheme. We reveal this $\pi^-\pi^+$ amplitude to be dominated by the $\rho(770)$ for both the $\pi_1(1600)$ and the nonresonant contribution. We determine the $\rho(770)$ resonance parameters within the three-pion final state. These findings largely confirm the underlying assumptions for the isobar model used in all previous partial-wave analyses addressing the $J^{PC} = 1^{-+}$ amplitude.

(to be submitted to Physical Review D)

The COMPASS Collaboration

G.D. Alexeev[7], M.G. Alexeev[26,27], A. Amoroso[26,27], V. Andrieux[9,29], V. Anosov[7],
K. Augsten[7,18], W. Augustyniak[30], C.D.R. Azevedo[1], B. Badełek[31], F. Balestra[26,27], M. Ball[3],
J. Barth[3], R. Beck[3], Y. Bedfer[20], J. Berenguer Antequera[26,27], J. Bernhard[12,9], M. Bodlak[17],
F. Bradamante[25], A. Bressan[24,25], V. E. Burtsev[28], W.-C. Chang[21], C. Chatterjee[24,25,a],
M. Chiosso[26,27], A. G. Chumakov[28], S.-U. Chung[15,b,c], A. Cicuttin[25,23], P. M. M. Correia[1],
M.L. Crespo[25,23], D. D'Ago[24,25], S. Dalla Torre[25], S.S. Dasgupta[6], S. Dasgupta[25], I. Denisenko[7],
O.Yu. Denisov[27], S.V. Donskov[19], N. Doshita[33], Ch. Dreisbach[15], W. Dünnweber[d],
R. R. Dusaev[28], A. Efremov[7,e], D. Eremeev[28], P.D. Eversheim[3], P. Faccioli[11], M. Faessler[d],
M. Finger[17], M. Finger jr.[17], H. Fischer[8], K. Floethner[3], C. Franco[11], J.M. Friedrich[15],
V. Frolov[7,9], L. Garcia Ordonez[25,23], F. Gautheron[2,29], O.P. Gavrichtchouk[7], S. Gerassimov[14,15],
J. Giarra[12], D. Giordano[26,27], M. Gorzellik[8,f], A. Grasso[26,27], A. Gridin[7], M. Grosse
Perdekamp[29], B. Grube[15], M. Grüner[3], A. Guskov[7], F. Haas[15], D. von Harrach[12], R. Heitz[29],
M. Hoffmann[3,a], N. Horikawa[16,g], N. d'Hose[20], C.-Y. Hsieh[21,h], S. Huber[15], S. Ishimoto[33,i],
A. Ivanov[7], T. Iwata[33], M. Jandek[18], V. Jary[18], R. Joosten[3], E. Kabuß[12], F. Kaspar[15],
A. Kerbizi[24,25,a], B. Ketzer[3], G.V. Khaustov[19], Yu.A. Khokhlov[19,k], Yu. Kisselev[7,e], F. Klein[4],
J.H. Koivuniemi[2,29], V.N. Kolosov[19], I. Konorov[14,15], V.F. Konstantinov[19], A.M. Kotzinian[27,l],
O.M. Kouznetsov[7], A. Koval[30], Z. Kral[17], F. Krinner[15,#], F. Kunne[20], K. Kurek[30],
R.P. Kurjata[32], A. Kveton[17], K. Lavickova[18], S. Levorato[9,25], Y.-S. Lian[21,m], J. Lichtenstadt[22],
P.-J. Lin[20,n], R. Longo[29], V. E. Lyubovitskij[28,o], A. Maggiora[27], A. Magnon[6], N. Makins[29],
N. Makke[25], G.K. Mallot[9,8], A. Maltsev[7], S. A. Mamon[28], B. Marianski[30,e], A. Martin[24,25],
J. Marzec[32], J. Matoušek[17], T. Matsuda[13], G. Mattson[29], F. Metzger[3], M. Meyer[29,20],
W. Meyer[2], Yu.V. Mikhailov[19], M. Mikhasenko[3,9], E. Mitrofanov[7], Y. Miyachi[33], A. Moretti[24,25],
A. Nagaytsev[7], C. Naim[20], D. Neyret[20], J. Nový[18], W.-D. Nowak[12], G. Nukazuka[33],
A.G. Olshevsky[7], M. Ostrick[12], D. Panzieri[27,p], B. Parsamyan[27,7,#], S. Paul[15], H. Pekeler[3],
J.-C. Peng[29], M. Pešek[17], D.V. Peshekhonov[7], M. Pešková[17], N. Pierre[12,20], S. Platchkov[20],
J. Pochodzalla[12], V.A. Polyakov[19], J. Pretz[4,q], M. Quaresma[21,11], C. Quintans[11], G. Reicherz[2],
C. Riedl[29], T. Rudnicki[31], D.I. Ryabchikov[19,15,#], A. Rychter[32], A. Rymbekova[7],
V.D. Samoylenko[19], A. Sandacz[30], S. Sarkar[6], I.A. Savin[7], G. Sbrizzai[24,25], S. Schmeing[15],
H. Schmieden[4], A. Selyunin[7], K. Sharko[28], L. Sinha[6], M. Slunecka[7,17], D. Spülbeck[3], A. Srnka[5],
D. Steffen[9,15], M. Stolarski[11], O. Subrt[9,18], M. Sulc[10], H. Suzuki[33,g], S. Tessaro[25],
F. Tessarotto[25,9,#], A. Thiel[3], J. Tomsa[17], F. Tosello[27], A. Townsend[29], T. Triloki[25,a],
V. Tskhay[14], S. Uhl[15], B. Valinoti[25,23], A. Vauth[4,9,r], B. M. Veit[12,9], J. Veloso[1], B. Ventura[20],
A. Vidon[20], M. Virius[18], M. Wagner[3], S. Wallner[15], K. Zaremba[32], M. Zavertyaev[14],
M. Zemko[17,9], E. Zemlyanichkina[7], Y. Zhao[25,s] and M. Ziembicki[32]

1 University of Aveiro, I3N, Dept. of Physics, 3810-193 Aveiro, Portugal
2 Universität Bochum, Institut für Experimentalphysik, 44780 Bochum, Germany[t,u]
3 Universität Bonn, Helmholtz-Institut für Strahlen- und Kernphysik, 53115 Bonn, Germany[t]
4 Universität Bonn, Physikalisches Institut, 53115 Bonn, Germany[t]
5 Institute of Scientific Instruments of the CAS, 61264 Brno, Czech Republic[v]
6 Matrivani Institute of Experimental Research & Education, Calcutta-700 030, India[w]
7 Joint Institute for Nuclear Research, 141980 Dubna, Moscow region, Russia[x]
8 Universität Freiburg, Physikalisches Institut, 79104 Freiburg, Germany[t,u]
9 CERN, 1211 Geneva 23, Switzerland
10 Technical University in Liberec, 46117 Liberec, Czech Republic[v]
11 LIP, 1649-003 Lisbon, Portugal[y]
12 Universität Mainz, Institut für Kernphysik, 55099 Mainz, Germany[t]
13 University of Miyazaki, Miyazaki 889-2192, Japan[z]

[14] Lebedev Physical Institute, 119991 Moscow, Russia

[15] Technische Universität München, Physik Dept., 85748 Garching, Germany[t]

[16] Nagoya University, 464 Nagoya, Japan[z]

[17] Charles University, Faculty of Mathematics and Physics, 12116 Prague, Czech Republic[v]

[18] Czech Technical University in Prague, 16636 Prague, Czech Republic[v]

[19] State Scientific Center Institute for High Energy Physics of National Research Center 'Kurchatov Institute', 142281 Protvino, Russia

[20] IRFU, CEA, Université Paris-Saclay, 91191 Gif-sur-Yvette, France[u]

[21] Academia Sinica, Institute of Physics, Taipei 11529, Taiwan[aa]

[22] Tel Aviv University, School of Physics and Astronomy, 69978 Tel Aviv, Israel[ab]

[23] Abdus Salam ICTP, 34151 Trieste, Italy

[24] University of Trieste, Dept. of Physics, 34127 Trieste, Italy

[25] Trieste Section of INFN, 34127 Trieste, Italy

[26] University of Torino, Dept. of Physics, 10125 Torino, Italy

[27] Torino Section of INFN, 10125 Torino, Italy

[28] Tomsk Polytechnic University, 634050 Tomsk, Russia[ac]

[29] University of Illinois at Urbana-Champaign, Dept. of Physics, Urbana, IL 61801-3080, USA[ad]

[30] National Centre for Nuclear Research, 02-093 Warsaw, Poland[ae]

[31] University of Warsaw, Faculty of Physics, 02-093 Warsaw, Poland[ae]

[32] Warsaw University of Technology, Institute of Radioelectronics, 00-665 Warsaw, Poland[ae]

[33] Yamagata University, Yamagata 992-8510, Japan[z]

Contents

I Introduction

The presently known meson spectrum is to a large extent attributed to quark-antiquark ($q\bar{q}'$) states. These states, i.e., the ground states and their excitations, are described by the constituent-quark model and are classified using $SU(3)_{\text{flavor}} \times SU(2)_{\text{spin}}$ symmetry. However, QCD in principle allows for a richer spectrum of excitations including multi-quark configurations as well as gluonic excitations, called "exotic" mesons hereafter. Such states are expected to be different from $q\bar{q}'$ states in terms of either their quantum numbers and/or their couplings to initial or final states, thus leaving their own fingerprints. In case of quantum numbers allowed for constituent-quark model states, they may, however, mix in configuration space.

Many model calculations for light-quark states comprising u, d or s quarks exist, predicting a variety of features (see e.g., Refs. [1–5]), but no clear signatures exist. More recently, first calculations of the excitation spectrum of light mesons have been performed by the authors of Refs. [6–9] using lattice QCD. They find exotic states with large contributions from excited gluonic field configurations, i.e., hybrid mesons, the lightest of which having so-called spin-exotic quantum numbers $J^{PC} = 1^{-+}$ that are forbidden for $q\bar{q}$ states.[a] However, the predictive power of these calculations is currently limited by the fact that all states are considered to be quasi-stable. Recently, the authors of Ref. [10] have performed the first lattice QCD calculation of the hadronic decays of the lightest 1^{-+} resonance. This calculation was performed using up, down, and strange-quark masses that approximately match the physical strange-quark mass. At this $SU(3)_{\text{flavor}}$ symmetric point, which corresponds to a pion mass of about $700\,\text{MeV}/c^2$, the scattering amplitudes of eight meson-meson systems were studied in a coupled-channel approach. Extrapolating the extracted resonance pole and its couplings to the physical light-quark masses suggests a broad π_1 resonance that decays predominantly into $b_1(1235)\pi$ and that has much smaller partial widths into $f_1(1285)\pi$, $\rho(770)\pi$, $\eta'\pi$, and $\eta\pi$. The present state-of-the-art method to calculate multi-body decays and scattering processes on the lattice requires using large pion masses to limit the analysis to coupled two-body channels only (see e.g., Ref. [11] and references therein). However, the extension of these calculations to three-body final states is under active development (see e.g., Ref. [12]).

The field of exotic hadrons has changed dramatically with the observations of the X, Y, Z states involving heavy quarks. In particular, the observation of charged quarkonium-like states, $Z_c^{\pm}$ [13, 14] and $Z_b^{\pm}$ [15], has been considered as clear evidence for the existence of exotic hadrons. They are characterized by an exotic combination of presumed flavor content and isospin quantum numbers. In addition, the P_c states are considered as the first observation of pentaquark states [16, 17]. The nature and internal structure of these states are discussed widely in the literature (see e.g. Refs. [18, 19]).

In the sector of light-quark mesons, several candidates for non-$q\bar{q}'$ states with conventional $q\bar{q}'$ quantum numbers are discussed in the literature, e.g., $f_0(1500)$, $\pi(1300)$, $\pi(1800)$, $a_1(1420)$, and $f_1(1420)$, although none of them was conclusively identified as such. While production and decay patterns constitute a mandatory but often strongly model-dependent signature, spin-exotic J^{PC} quantum numbers are generally considered the cleanest path to prove the existence of meson-like objects beyond $q\bar{q}'$. Three such states with $J^{PC} = 1^{-+}$, the $\pi_1(1400)$, $\pi_1(1600)$, and the $\pi_1(2015)$, have been discussed frequently as first evidence for exotic mesons and their observation was reported by various experiments [20]. Their masses agree qualitatively with lattice QCD calculations [9]. However, the existence of these states is disputed and the experimental situation requires clarification and further studies. The $\pi_1(1400)$ has been observed by several experiments [21–26] in the $\eta\pi$ final state produced in π^- diffraction at beam momenta ranging

---

[a]Here, J is the spin, P the parity, and C the charge conjugation quantum number of the state.

from 6.3 to $100\,\mathrm{GeV}/c$. It has also been observed in the $\eta\pi$ final state produced in $\bar{p}p$ and $\bar{p}n$ annihilations studied by the Crystal Barrel experiment [27–29] and in the $\rho(770)\pi$ channel by the Obelix experiment [30]. The $\pi_1(2015)$ has so far been observed only by the BNL E852 experiment in the $f_1(1285)\pi$ [31] and $b_1(1235)\pi$ [32] decay modes.

A Status of the $\pi_1(1600)$

The $\pi_1(1600)$ is the most extensively studied spin-exotic meson. Indications were found in $\eta'\pi$ [33–36], in $f_1(1285)\pi$ [31,35,37], and in $b_1(1235)\pi$ [32,33,35,37,38]. Recently, the COMPASS collaboration has published further studies on the $\eta'\pi$ and $\eta\pi$ final states in diffractive production relevant to the search for $\pi_1(1600)$. A reanalysis of these data that are discussed in Ref. [39] revealed a clear resonance pole in the spin-exotic wave [40]. This analysis could even reconcile the observations of the two spin-exotic states $\pi_1(1400)$ and $\pi_1(1600)$ to be the result of only a single pole with parameters that are consistent with the $\pi_1(1600)$.

In this paper, we focus on the $\pi^-\pi^-\pi^+$ final state including the $\rho(770)\pi$ intermediate state. An observation of the decay $\pi_1(1600) \to \rho(770)\pi$ was first reported by BNL E852 [41,42] followed by VES [37]. Later, the COMPASS experiment confirmed some of the previous findings [43]. For a review, we refer to Ref. [44]. All above experiments studied diffractive pion dissociation, but at different beam energies, different target materials, and in various ranges of the four-momentum transfer squared. Previous investigations of the 3π final state yielded contradicting conclusions on what concerns the proof of existence of the $\pi_1(1600)$ or the determination of its properties. While BNL E852 [41,42] and COMPASS have stressed the observation of the $\pi_1(1600)$, VES [37] and an analysis of BNL data by Dzierba *et al.* [45] have been inconclusive on its existence or even refuted it.

Recently, COMPASS published an extensive study of isovector mesons using a large data set for the $\pi^-\pi^-\pi^+$ final state [46]. In this analysis, we observed a strong modulation of the shape of the intensity distribution of the spin-exotic $\rho(770)\pi$ P-wave carrying $J^{PC} = 1^{-+}$ with the squared four-momentum t' transferred from the beam to the target particle [see Figs. 1(a) and 1(b) and definition in Eq. (2)]. This modulation is described by the resonance model as a t'-dependent interference between a $\pi_1(1600)$ resonance (blue curves) and a nonresonant wave component (green curves). The nonresonant component was found to dominate at low t' whereas the $\pi_1(1600)$ signal emerged at high t'. The resonance characteristics of the $\pi_1(1600)$ signal was clearly demonstrated through its phase variation with respect to 13 other waves. As an example, we show in Fig. 1(c) the phase motion with respect to the $\rho(770)\pi$ S-wave carrying $J^{PC} = 1^{++}$. In addition, the dashed red curves in Fig. 1 show the result of a fit, where the $\pi_1(1600)$ resonance was omitted from the fit model. Although at low t', where the nonresonant component is dominant, this model is in fair agreement with data, it fails to describe the data at high t'. This demonstrates that a $\pi_1(1600)$ resonance is needed to describe the COMPASS data.

The discrepancy of results and interpretations on the $\pi_1(1600)$ signal from the analyses discussed above requires detailed studies as the origin could be either inconsistent data sets or analysis artifacts. This paper aims at understanding three different aspects of the spin-exotic $\rho(770)\pi$ P-wave carrying $J^{PC} = 1^{-+}$ based on the large COMPASS data sample: (i) Can the different and partially inconsistent observations from previous analyses be reconciled through studies of the model dependence of the analyses? (ii) Are structures observed in this wave an artifact of the partial-wave analysis model? Since the resonant nature of the $\pi_1(1600)$ has been already studied extensively in Ref. [46], we will not readdress the determination the $\pi_1(1600)$ resonance parameters here. (iii) Can we model nonresonant production through the so-called Deck effect [48]?

This paper is organized as follows: After a short description of the COMPASS experiment in Sec. II, we will briefly review the analysis of our data in Sec. III. Sections IV to VI each will
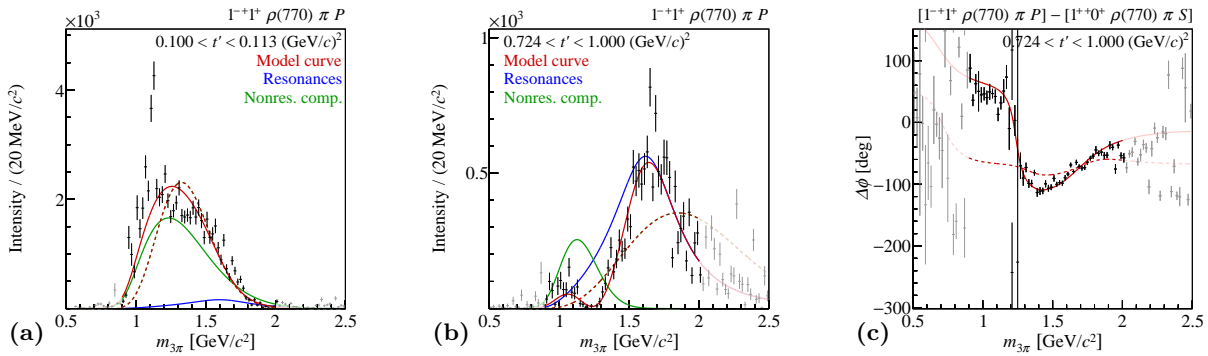
FIG. 1: Excerpt from the results of a previous study of resonance production in $\pi^- \; p \to \pi^- \pi^- \pi^+ \; p$ at $190 \, \mathrm{GeV}/c$ pion-beam momentum by the COMPASS collaboration [46, 47]. The partial-wave intensities of the spin-exotic $\rho(770)\pi$ P-wave carrying $J^{PC} = 1^{-+}$ are shown in panels (a) and (b) for the lowest and highest t' bins, respectively, covered by the experiment. Panel (c) shows the phase relative to the $\rho(770)\pi$ S-wave carrying $J^{PC} = 1^{++}$. The red solid curve represents the full resonance model (see Tab. II in Ref. [46]), which is the coherent sum of wave components that are represented by the other solid curves: $\pi_1(1600)$ resonance (blue curves) and nonresonant component (green curves). The extrapolation of the model and the wave components beyond the fit range are shown in lighter colors. The narrow enhancement at $1.1 \, \mathrm{GeV}/c^2$ in (a) is likely an artifact induced by imperfections in the analysis method (see Sec. IV A). The dashed red curves represent a fit, where the $\pi_1(1600)$ resonance was omitted from the fit model. This curve hence corresponds to a nonresonant $\rho(770)\pi$ P-wave.

address one of the three questions that we posed above. In Sec. IV, we will reconcile our analyses and previous ones performed by the BNL E852 [41, 42, 45] and VES [37] experiments and trace the discrepancies to the different analysis schemes used. Next, in Sec. V we will extract the amplitude of the $\pi^- \pi^+$ subsystem present in the $J^{PC} = 1^{-+}$ wave using the new scheme of freed-isobar analysis [49] proving the decay of $\pi_1(1600) \to \rho(770)\pi$. Finally, we compare in Sec. VI the observed intensity distributions (diagonal elements of the spin-density matrix) of selected partial waves to model calculations on nonresonant 3π production. Each of the three sections will provide evidence that further confirms the $\pi_1(1600)$ resonance and its decay into $\rho(770)\pi$. Since the three result sections are linked only weakly, we will summarize and conclude them individually and refrain from an additional summary and conclusion at the end of the paper.

II Analyzed data sample

The present study is based on a data set of 46×10^6 exclusive events of diffractively produced mesons decaying into three charged pions. The data were obtained by the COMPASS experiment and were already presented in detail in Ref. [47]. They contain exclusive events from the inelastic reaction

$$\pi^- + p \to \pi^- \pi^- \pi^+ + p, \tag{1}$$

which is induced by a high-energy π^- beam impinging on a hydrogen target. The dominant reaction mechanism is single-diffractive scattering, where the target particle scatters elastically and the beam pion is excited via the exchange of a Pomeron with the target nucleon to a short-lived intermediate state X^- that then decays into $\pi^- \pi^- \pi^+$ as shown in Fig. 2. The experimental setup and the criteria that were applied to select exclusive events of reaction (1) are described in detail in Refs. [47, 50]. Here, we give only a brief summary.
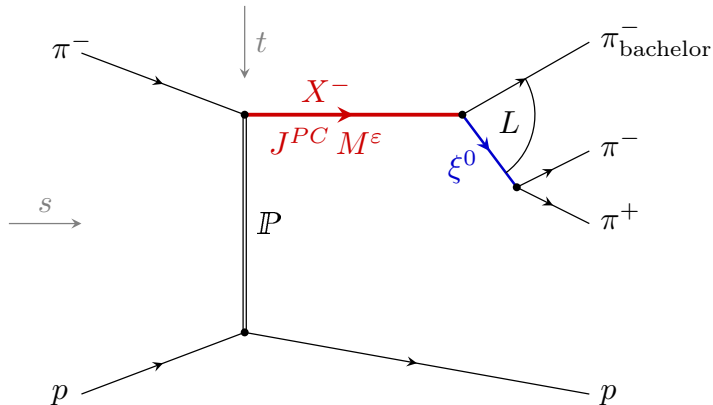
FIG. 2: Single-diffractive dissociation of a beam pion on a target proton into the $\pi^-\pi^-\pi^+$ final state via exchange of a Pomeron $\mathbb{P}$. In this scattering process, an intermediate 3π state X^- with well-defined quantum numbers is produced. The decay of X^- is described using the isobar model, which assumes that the decay proceeds via intermediate $\pi^-\pi^+$ states ξ^0, the so-called isobars, which also have well-defined quantum numbers. See Sec. III for details.

The COMPASS experiment [51, 52] is located at the M2 beam line of the CERN Super Proton Synchrotron. A beam of negatively charged secondary pions with $190\,\text{GeV}/c$ momentum was incident on a $40\,\text{cm}$ long liquid-hydrogen target. The data selection required a recoil-proton signal and an exclusive measurement was ensured through a variety of criteria [47].

Reaction (1) depends on two Mandelstam variables: the squared π^-p center-of-momentum energy s, which is fixed to about $(19\,\text{GeV})^2$ by the beam momentum, and the squared four-momentum t transferred from the beam to the target particle. It is convenient to define the *reduced four-momentum transfer squared*

$$t' \equiv |t| - |t|_{\min} \geq 0, \tag{2}$$

where

$$|t|_{\min} \approx \left(\frac{m_{3\pi}^2 - m_\pi^2}{2|\vec{p}_{\text{beam}}|} \right)^2 \tag{3}$$

is the minimum absolute value of the four-momentum transfer needed to excite the beam pion to a 3π state with invariant mass $m_{3\pi}$.[b] The beam momentum $\vec{p}_{\text{beam}}$ is defined in the laboratory frame. For the present analysis, t' was chosen to be in the range from 0.1 to 1.0 $(\text{GeV}/c)^2$, where the lower bound is dictated by the acceptance of the recoil-proton detector and the upper bound by the experimental decrease of the number of events with t'.

Since reaction (1) is dominated by Pomeron exchange, which conserves isospin I and G parity of the beam pion, only intermediate states X^- with $I^G = 1^-$ can be produced. This limits the analysis to meson states that belong to the π_J and a_J families. This analysis focuses on 3π resonances with masses up to about $2\,\text{GeV}/c^2$. We hence selected the $m_{3\pi}$ range from 0.5 to 2.5 GeV/c^2.

III Partial-wave analysis method

We extract the $\pi_1(1600)$ contribution with $J^{PC} = 1^{-+}$ from the COMPASS data through a partial-wave analysis (PWA) using a model comprising 88 partial waves (see Table 4 in

---

[b]For the kinematic range considered here, $|t|_{\min}$ is well below $10^{-3}\,(\text{GeV}/c)^2$ and hence $t' \approx -t$.

Appendix A). The PWA model has already been described in detail in Refs. [47, 53], so we will provide here only a brief description.

We subdivide the data into 100 equidistant $20\,\mathrm{MeV}/c^2$ wide bins of the invariant mass $m_{3\pi}$ of the 3π system and into 11 nonequidistant bins of the reduced four-momentum transfer squared t' (see Tab. IV in Ref. [47]) resulting in 1100 kinematic $(m_{3\pi}, t')$ cells. We fit each of these cells independently with a PWA model for the intensity distribution,

$$\mathcal{I}(\tau; m_{3\pi}, t') = \sum_{\varepsilon=\pm 1} \sum_{r=1}^{N_r^\varepsilon} \left| \sum_a^{N_{\mathrm{waves}}^\varepsilon} \mathcal{T}_a^{r\varepsilon}(m_{3\pi}, t')\, \Psi_a^\varepsilon(\tau; m_{3\pi}) \right|^2 + \mathcal{I}_{\mathrm{flat}}(m_{3\pi}, t'), \qquad (4)$$

using an unbinned extended maximum likelihood approach. Here, τ represents the five three-body phase-space variables in a given $(m_{3\pi}, t')$ cell (see Sec. III in Ref. [47] for a concrete choice for τ). The indices ε and r are explained below. The transition amplitude $\mathcal{T}_a^{r\varepsilon}$ encodes the (unknown) strength and phase of partial wave a, while the decay amplitude $\Psi_a^\varepsilon(\tau)$ encodes the (known) dependence on τ. Within a given $(m_{3\pi}, t')$ cell, we neglect the dependence on $m_{3\pi}$ and t', i.e., $\mathcal{T}_a^{r\varepsilon}$ is constant and Ψ_a^ε depends only on τ. The term $\mathcal{I}_{\mathrm{flat}}$ is the intensity of the so-called flat wave, which represents three uncorrelated final-state pions that are distributed isotropically in the three-body phase space. The flat wave contributes only $3.1\,\%$ to the total intensity.

The partial waves that enter Eq. (4) are uniquely defined by the quantum numbers of the intermediate state X^- and its decay mode (see Fig. 2). The X^- quantum numbers are: isospin I, G parity, spin J, parity P, C parity, and the projection M of J along the beam axis.[c] We express the amplitudes in Eq. (4) in the reflectivity basis [54]. As a consequence, $M \geq 0$ and an additional quantum number of X^-, the reflectivity $\varepsilon = \pm 1$, is introduced. The formulation in the reflectivity basis allows us to take into account parity conservation in the scattering process by summing incoherently over ε. In addition, at high s and neglecting corrections of order $1/s$, ε corresponds to the naturality of the exchange particle in the scattering process [55–57]. Since at high s the scattering process is dominated by Pomeron exchange, which has $\varepsilon = +1$, partial-wave amplitudes with $\varepsilon = -1$ are suppressed. Hence the two reflectivity sectors are in general described using wave sets with different numbers $N_{\mathrm{waves}}^\varepsilon$ of waves.

For the COMPASS data, we find that a PWA model with $N_{\mathrm{waves}}^{\varepsilon=+1} = 80$, $N_{\mathrm{waves}}^{\varepsilon=-1} = 7$, and the flat wave describes the data well [47]. This 88-wave set is listed in Table 4 in Appendix A. As we will show in Sec. IV, the wave set has a strong influence on the shape and intensity of the spin-exotic $J^{PC} = 1^{-+}$ wave with $M^\varepsilon = 1^+$, which contains a potential $\pi_1(1600)$ signal.

The incoherent sum over the index r in Eq. (4) is used to model the incoherence in the scattering process. Incoherences may, for example, arise due to spin flip and spin non-flip of the target proton. Also performing the PWA over wide t' ranges may lead to effective incoherence because the transition amplitudes of the various waves have different t' dependences (see discussion below). The number N_r^ε of incoherent terms corresponds to the rank of the spin-density submatrix with reflectivity ε. Since the two values of ε correspond to different production mechanisms, the rank may be different for different ε. For the COMPASS data, we find that a PWA model with $N_r^{\varepsilon=+1} = 1$ and $N_r^{\varepsilon=-1} = 2$ describes the data well [47]. This means that all positive-reflectivity waves are assumed to be fully coherent. The sum of the negative-reflectivity amplitudes contributes only $2.2\,\%$ to the total intensity confirming the dominance of positive-reflectivity waves.

We construct the decay amplitudes in Eq. (4) using the helicity formalism and the isobar model

---

[c]Although the C parity is not defined for charged systems, it is customary to quote the J^{PC} quantum numbers of the corresponding neutral partner state in the isospin triplet. For nonstrange light mesons, the C parity is related to the G parity via $G = C\, e^{i\pi I_y}$, where I_y is the y component of the isospin.

(see Sec. III in Ref. [47] for details), i.e., we assume that the decay $X^- \to \pi^-\pi^-\pi^+$ proceeds via two subsequent two-particle decays, $X^- \to \xi^0\pi^-$ and $\xi^0 \to \pi^-\pi^+$, with intermediate two-pion states ξ^0, which are called isobars (see Fig. 2). The decay amplitude of a partial wave contains a propagator term $\Delta_a(m_{\pi^-\pi^+})$ that describes this isobar resonance and that we refer to as dynamic isobar amplitude. In the case of the $\rho(770)$ resonance, which dominates the $J^{PC}M^\varepsilon = 1^{-+}1^+$ wave, we use a relativistic Breit-Wigner amplitude with mass-dependent width as given by Eqs. (31) and (40) in Ref. [47] as the dynamic isobar amplitude.

In the following, we adopt the partial-wave notation $J^{PC}M^\varepsilon\xi^0\pi L$, where $\xi^0\pi L$ defines the decay mode of X^- and L is the orbital angular momentum between the isobar and the bachelor π^- (see Fig. 2). This means that the wave index in Eq. (4) is given by

$$a = J^{PC}M^\varepsilon\xi^0\pi L. \tag{5}$$

The t' dependence of the transition amplitudes $\mathcal{T}_a^{r\varepsilon}(m_{3\pi}, t')$ in Eq. (4) is in general unknown and may be different for different waves a. In diffractive reactions, the t' spectra of the transition amplitudes exhibit an approximately exponential decrease with t' in the range $t' \lesssim 1\,(\mathrm{GeV}/c)^2$. This behavior can be explained in the framework of Regge theory [58]. For partial waves with $M \neq 0$, the t' spectra are modified by an additional factor $(t')^{|M|}$, which is given by the forward limit of the Wigner D-functions [58]. This factor suppresses the intensity of the waves toward small t', i.e., the transition amplitude is approximately proportional to $(t')^{|M|/2}$. Diffractive production of $J^{PC} = 1^{-+}$ waves requires $M = 1$. This follows from parity conservation and the dominance of natural-parity exchange in hadronic high-energy scattering reactions [54].[d] As a consequence, 1^{-+} partial-wave amplitudes with positive reflectivity are suppressed at low t'.

In the analyses of small data sets (some of which will be discussed in Sec. IV below), where a binning in t' is not possible, the t' dependence of the transition amplitudes is often modeled by replacing the transition amplitudes via

$$\mathcal{T}_a^{r\varepsilon}(m_{3\pi}, t') \to \mathcal{T}_a^{r\varepsilon}(m_{3\pi}, t')\, f_a^\varepsilon(t'), \tag{6}$$

where the $f_a^\varepsilon(t')$ are empirical real-valued functions. The parameters of these functions are usually determined from data by performing the PWA in wide $m_{3\pi}$ ranges and narrow t' bins. This approach assumes that the shapes of the t' spectra of the partial waves are largely independent of $m_{3\pi}$ and also does not take into account possible t' dependences of the relative phases between the partial waves. However, we have shown in Ref. [47], by performing the PWA in 11 narrow t' bins and extracting the t' dependences in a model-independent way, that for some waves the above assumptions do not hold.

IV Previous results on $\pi_1(1600) \to \rho(770)\pi$

In the past two decades, several experiments studied the $1^{-+}1^+\rho(770)\pi P$ wave in the 3π final state. The key parameters of the analyzed data samples and the employed PWA models are listed in Table 1. A list of the wave sets can be found in Table 4 in Appendix A. In Fig. 3, we show the intensity distributions of the $1^{-+}1^+\rho(770)\pi P$ wave as obtained in the previous analyses. Based on these distributions, the previous experiments arrived at seemingly contradictory conclusions concerning the existence of a $\pi_1(1600)$ signal in the $\rho(770)\pi$ channel. We will briefly summarize these findings in the following.

The BNL E852 experiment was the first to claim a signal for $\pi_1(1600) \to \rho(770)\,\pi$ based on a PWA performed on 250×10^3 events obtained using an $18.3\,\mathrm{GeV}/c$ pion beam incident on a

---

[d]$M = 0$ would be allowed only in unnatural-parity exchange with $\varepsilon = -1$.

Table 1: Key parameters of the data sets and the PWA models used in analyses of diffractively produced 3π events studying a possible spin-exotic $J^{PC} = 1^{-+}$ resonance in the $\rho(770)\pi$ channel. The table also indicates whether the model takes into account different t' dependences of the partial-wave amplitudes either by binning in t' or by modeling. The wave sets are listed in Table 4 in Appendix A.

Experiment	Data set	PWA model
BNL E852 [41, 42]	$18.3\,\mathrm{GeV}/c\ \pi^-$ beam proton target $250 \times 10^3\ \pi^-\pi^-\pi^+$ events	21 waves, rank 1 $0.05 < t' < 1.0\,(\mathrm{GeV}/c)^2$ same t' dependence for all partial-wave amplitudes
VES [37]	$36.6\,\mathrm{GeV}/c\ \pi^-$ beam beryllium target $3.0 \times 10^6\ \pi^-\pi^-\pi^+$ events	44 waves, "maximum" rank $0.03 < t' < 1.0\,(\mathrm{GeV}/c)^2$ $f_a^\varepsilon(t') = (t')^{|M|/2}$ [see Eq. (6)]
BNL E852 [45]	$18.3\,\mathrm{GeV}/c\ \pi^-$ beam proton target $2.6 \times 10^6\ \pi^-\pi^-\pi^+$ events $3.0 \times 10^6\ \pi^-\pi^0\pi^0$ events	36 waves, rank 1 $0.08 < t' < 0.53\,(\mathrm{GeV}/c)^2$ 12 t' bins
COMPASS [43]	$190\,\mathrm{GeV}/c\ \pi^-$ beam lead target $420 \times 10^3\ \pi^-\pi^-\pi^+$ events	42 waves, rank 2 $0.1 < t' < 1.0\,(\mathrm{GeV}/c)^2$ $f_a^\varepsilon(t')$ for each partial wave a [see Eq. (6)]
COMPASS [46, 47]	$190\,\mathrm{GeV}/c\ \pi^-$ beam proton target $46 \times 10^6\ \pi^-\pi^-\pi^+$ events	88 waves, rank 1[e] $0.1 < t' < 1.0\,(\mathrm{GeV}/c)^2$ 11 t' bins

[e]A rank-1 spin-density matrix was used for the 80 waves with positive reflectivity. For the 7 waves with negative reflectivity (see Table 4 in Appendix A), which together contribute only 2.2 % to the total intensity, we used a rank-2 spin-density matrix.
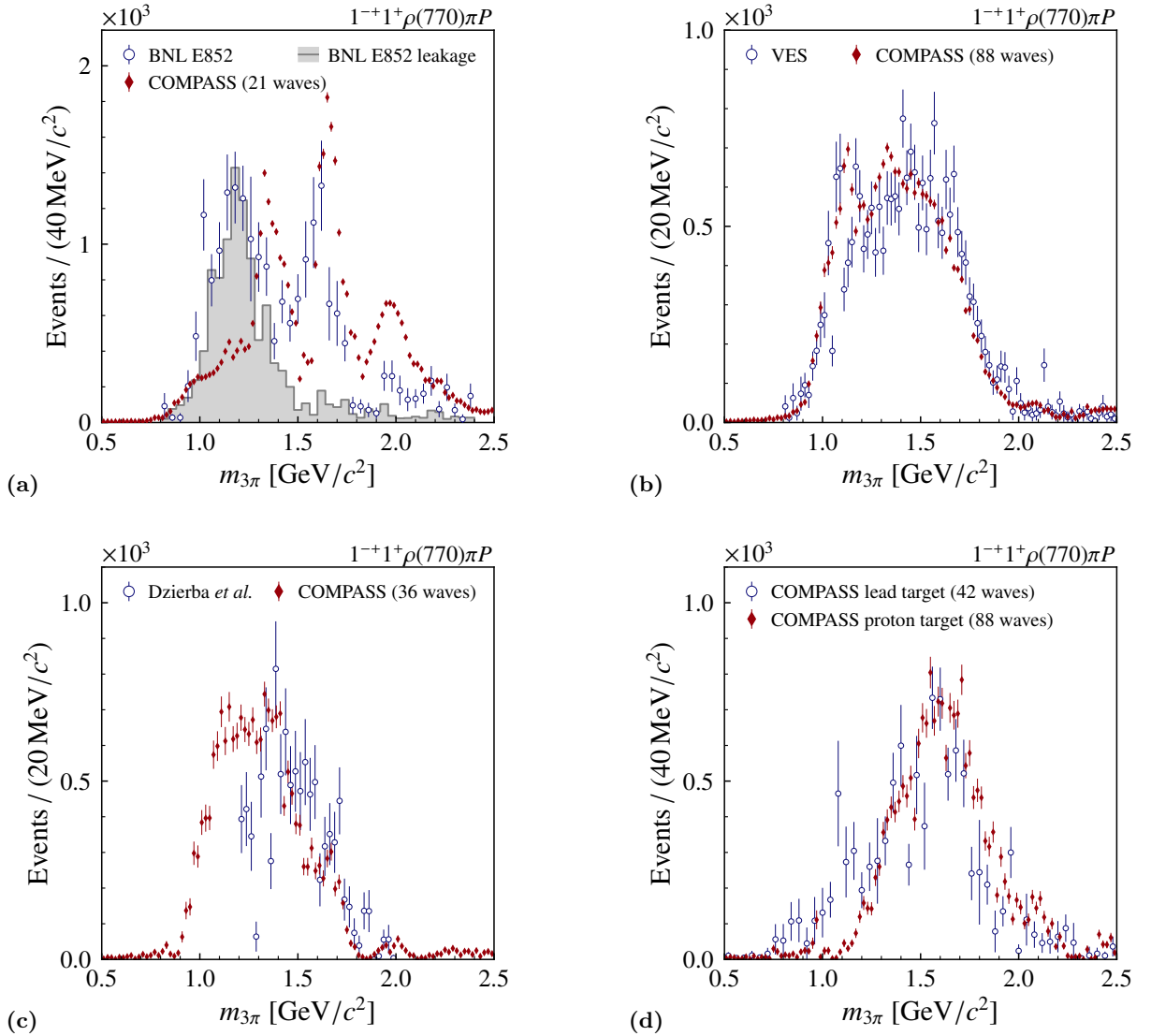
FIG. 3: Comparison of intensity distributions of the spin-exotic $1^{-+}1^+\rho(770)\pi P$ wave as obtained by different experiments measuring diffractive dissociation of a pion beam into 3π. Blue data points: (a) 21-wave fit of BNL E852 data in the range $0.05 < t' < 1.0\,(\mathrm{GeV}/c)^2$, (b) 44-wave fit of VES data in the range $0.03 < t' < 1.0\,(\mathrm{GeV}/c)^2$, (c) 36-wave fit of BNL E852 data in the range $0.18 < t' < 0.23\,(\mathrm{GeV}/c)^2$, and (d) 42-wave fit of COMPASS lead-target data in the range $0.1 < t' < 1.0\,(\mathrm{GeV}/c)^2$. The gray shaded area in panel (a) shows the result of a leakage study performed by the BNL E852 experiment [42]. The red data points show the results of corresponding analyses of the COMPASS proton-target data using 11 t' bins in the range $0.1 < t' < 1.0\,(\mathrm{GeV}/c)^2$: (a) t'-summed intensity distribution from the 21-wave PWA, (b) t'-summed intensity distribution from the 88-wave PWA, (c) intensity distribution from the 36-wave PWA in the range $0.189 < t' < 0.220\,(\mathrm{GeV}/c)^2$, and (d) intensity distribution from the 88-wave PWA in the range $0.449 < t' < 0.724\,(\mathrm{GeV}/c)^2$. The red data points are scaled such that the intensity integrals of the blue and red data points in the region where they overlap are equal. The blue data points are taken from (a) Fig. 18(b) in Ref. [42], (b) Fig. 4(a) in Ref. [37], (c) Fig. 25(a) in Ref. [45], and (d) Fig. 2(d) in Ref. [43]. The red data points in (d) are taken from Fig. 43(j) in Ref. [46].

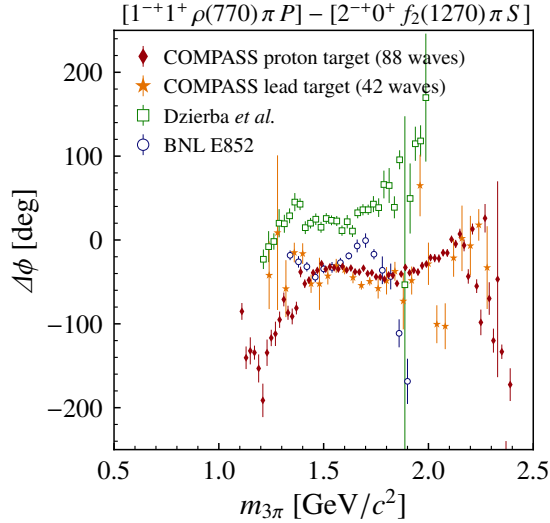**FIG. 4:** Comparison of the phases of the spin-exotic $1^{-+}1^+\rho(770)\pi P$ wave with respect to the $2^{-+}0^+ f_2(1270)\pi S$ wave as obtained by different experiments measuring diffractive dissociation of a pion beam into 3π. Blue data points: 21-wave fit of BNL E852 data in the range $0.05 < t'$ $< 1.0\,(\text{GeV}/c)^2$ (shifted by $-180°^{[\text{f}]}$); Green data points: 36-wave fit of BNL E852 data in the range $0.18 < t' < 0.23\,(\text{GeV}/c)^2$ (shifted by $+180°^{[\text{f}]}$); Orange data points: 42-wave fit of COMPASS lead-target data in the range $0.1 < t' < 1.0\,(\text{GeV}/c)^2$; Red data points: 88-wave fit of COMPASS proton-target data in the range $0.449 < t' < 0.742\,(\text{GeV}/c)^2$ (values for $m_{3\pi} < 1.1\,\text{GeV}/c^2$ not shown). The data points were taken from Fig. 19(i) in Ref. [42] (blue), Fig. 33 in Ref. [45] (green), Fig. 3(b) in Ref. [43] (orange), and Fig. 121 in Ref. [53] (red).

---

[f]Phase shifts of $\pm 180°$ may be caused e.g., by different choices of the analyzers in the definition of the coordinates systems or by different conventions used for the Wigner D-functions.

proton target in the kinematic range $0.05 < t' < 1.0\,(\text{GeV}/c)^2$ [41, 42]. The employed PWA model included 21 waves (see Table 4 in Appendix A) and a rank-1 spin-density matrix. The different t' dependences of the partial-wave amplitudes were not taken into account. The blue data points in Fig. 3(a) show the resulting intensity distribution of the $1^{-+}1^+\rho(770)\pi P$ wave. This distribution has two broad enhancements. The one in the 1.1 to $1.4\,\text{GeV}/c^2$ region was attributed to wrongly assigned intensity leaking from the dominant $1^{++}0^+\rho(770)\pi S$ wave into the $1^{-+}1^+$ $\rho(770)\pi P$ wave. This leakage was caused by the finite instrumental resolution in combination with a nonuniform detector acceptance. An estimate of this leakage obtained using Monte Carlo techniques is shown by the gray-shaded histogram in Fig. 3(a). The second peak at $1.6\,\text{GeV}/c^2$ is accompanied by phase motions with respect to many waves (see e.g., blue data points in Fig. 4 and Fig. 19 in Ref. [42]) and was hence interpreted as the $\pi_1(1600)$. A simultaneous fit of the $1^{-+}1^+\rho(770)\pi P$ and $2^{-+}0^+ f_2(1270)\pi S$ amplitudes and their relative phase (see Fig. 24 in Ref. [42]) yielded Breit-Wigner parameters of $m_{\pi_1(1600)} = 1593 \pm 8\,(\text{stat.})\,{}^{+29}_{-47}\,(\text{sys.})\,\text{MeV}/c^2$ and $\Gamma_{\pi_1(1600)} = 168 \pm 20\,(\text{stat.})\,{}^{+150}_{-12}\,(\text{sys.})\,\text{MeV}/c^2$. It is noteworthy that the $\pi_1(1600)$ peak remained when the PWA was performed in a low-t' region around $0.1\,(\text{GeV}/c)^2$. However, a strong dependence of the shape and magnitude of the $\pi_1(1600)$ signal on the PWA model was observed.

The VES experiment at IHEP used a $36.6\,\text{GeV}/c$ pion beam on a solid-beryllium target and performed a PWA on 3.0×10^6 events in the kinematic range $0.03 < t' < 1.0\,(\text{GeV}/c)^2$ [37]. The PWA model contained 44 waves (see Table 4 in Appendix A) and the spin-density matrix used in the PWA fit had maximum allowed rank. To search for resonances, they extracted from this spin-density matrix a rank-1 spin-density matrix of fully coherent partial-wave amplitudes.

In the PWA model, the partial-wave amplitudes were multiplied by an additional factor of $f_a^\varepsilon(t') = (t')^{|M|/2}$ [59] [see Eq. (6)] to take into account the fact that the partial-wave intensity is proportional to $(t')^{|M|}$. Using this approach, also the VES experiment observed significant intensity in the $1^{-+}1^+\rho(770)\pi P$ wave [see blue data points in Fig. 3(b)]. However, they did not observe a peak at $1.6\,\text{GeV}/c^2$ comparable to the one found in the BNL E852 analysis in Refs. [41, 42]. Instead, they found a very broad intensity distribution with a slow phase motion of about 60° in the $1.6\,\text{GeV}/c^2$ region (see Fig. 4 in Ref. [37]). From this they concluded that the $\rho(770)\pi$ data alone are inconclusive concerning the existence of a $\pi_1(1600)$ signal. However, in a combined fit of the intensity distributions of the 1^{-+} wave in the $b_1(1235)\pi$, $\eta'\pi$, and $\rho(770)\pi$ channels, they found a satisfactory description of the data using a $\pi_1(1600)$ resonance with $m_{\pi_1(1600)} = 1560 \pm 60\,\text{MeV}/c^2$ and $\Gamma_{\pi_1(1600)} = 340 \pm 50\,\text{MeV}/c^2$ (see Fig. 6 in Ref. [37]).

Dzierba *et al.* [45] performed a PWA of a second BNL E852 data sample of 5.6×10^6 3π events, which is a factor 20 larger than the one used in the first analysis in Refs. [41, 42]. The analysis was performed independently in 12 t' bins in the range from 0.08 to $0.53\,(\text{GeV}/c)^2$. The PWA model employed a rank-1 spin-density matrix and a set of 36 partial waves (see Table 4 in Appendix A). This wave set was derived from a larger parent wave set. The resulting intensity distribution of the $1^{-+}1^+\rho(770)\pi P$ wave is broad and structureless and shows no peak at $1.6\,\text{GeV}/c^2$. As an example, the blue data points in Fig. 3(c) show the intensity distribution in the t' bin from 0.18 to $0.23\,(\text{GeV}/c)^2$. The shape of the intensity distribution was found to change strongly with t' (see Fig. 31 in Ref. [45]). With increasing t', intensity moves from the $1.2\,\text{GeV}/c^2$ region to higher masses. Applying the 21-wave set from Refs. [41, 42], yielded a peak at $1.6\,\text{GeV}/c^2$ in the $1^{-+}1^+\rho(770)\pi P$ intensity distribution consistent with the first analysis of BNL E852 data (see Figs. 24 and 25 in Ref. [45]). The authors of Ref. [45] showed that leakage from the $\pi_2(1670)$ causes this peak, if the $2^{-+}0^+\rho(770)\pi P$, the $2^{-+}0^+\rho(770)\pi F$, and the $2^{-+}1^+\rho(770)\pi F$ wave are omitted from the 36-wave model (see Figs. 27 and 28 in Ref. [45]); the latter two waves were missing in the 21-wave model used in Refs. [41, 42]. Using moments of the Wigner D-functions, Dzierba *et al.* demonstrated that the 36-wave model describes the data significantly better than the 21-wave model. Based on these observations, they concluded that the BNL E852 data provide no evidence for the existence of a $\pi_1(1600)$ in the $\rho(770)\,\pi$ channel. For the discussion in Sec. IV A below it is important to note that this conclusion was based only on data in the range $t' < 0.53\,(\text{GeV}/c)^2$ and that it was not corroborated by any kind of resonance-model fit. In the 36-wave PWA, Dzierba *et al.* observed an enhancement around $1.6\,\text{GeV}/c^2$ in the higher t' bins (see Fig. 31 in Ref. [45]) and an approximately constant phase of the $1^{-+}1^+\rho(770)\pi P$ wave with respect to the $2^{-+}0^+f_2(1270)\pi S$ wave around $1.6\,\text{GeV}/c^2$ (see green data points in Fig. 4 shown in this paper and Figs. 25(b) and 33 in Ref. [45]). These effects could be a sign for a 1^{-+} resonance with similar parameters as the $\pi_2(1670)$, but were both ascribed to remaining leakage from the $\pi_2(1670)$ into the 1^{-+} wave.

In contrast, the first analysis of a much smaller data sample of 420×10^3 events obtained by the COMPASS experiment using a $190\,\text{GeV}/c$ pion beam on a solid-lead target showed clear evidence for a $\pi_1(1600)$ signal in the $1^{-+}1^+\rho(770)\pi P$ wave [43]. We performed the PWA employing a rank-2 spin-density matrix and a set of 42 waves (see Table 4 in Appendix A) in the range $0.1 < t' < 1.0\,(\text{GeV}/c)^2$ using a parametrization for the t' dependence of the partial-wave amplitudes like in Eq. (6) with different parameters for each wave. The 42-wave set is similar to the 36-wave set used by Dzierba *et al.* in Ref. [45] having 29 waves in common. In particular, it contains those three 2^{-+} waves that were found to make the peak at $1.6\,\text{GeV}/c^2$ disappear (see discussion above). The resulting intensity distribution of the $1^{-+}1^+\rho(770)\pi P$ wave is shown as blue data points in Fig. 3(d). By performing a resonance-model fit of 6 partial-wave amplitudes simultaneously, we obtained Breit-Wigner parameters of $m_{\pi_1(1600)} = 1660 \pm 10\,(\text{stat.})\,^{+0}_{-64}\,(\text{sys.})\,\text{MeV}/c^2$ and $\Gamma_{\pi_1(1600)} = 269 \pm 21\,(\text{stat.})\,^{+42}_{-64}\,(\text{sys.})\,\text{MeV}/c^2$. The $\pi_1(1600)$ parameters are similar to the ones

found for the $\pi_2(1670)$, which are $m_{\pi_2(1670)} = 1658 \pm 3\,(\text{stat.})\,^{+24}_{-8}\,(\text{sys.})\,\text{MeV}/c^2$ and $\Gamma_{\pi_2(1670)} = 271 \pm 9\,(\text{stat.})\,^{+22}_{-24}\,(\text{sys.})\,\text{MeV}/c^2$. This explains the approximately constant phase observed between the $1^{-+}1^+\rho(770)\pi P$ and $2^{-+}0^+ f_2(1270)\pi S$ waves (see orange data points in Fig. 4).

A Comparison of previous results with COMPASS proton-target data

The COMPASS collaboration has recently published a detailed PWA of the $\pi^-\pi^-\pi^+$ final state using a PWA model with 88 waves (see Tables 1 and 4). Here, we focus on the $1^{-+}1^+\rho(770)\pi P$ wave. The red data points in Fig. 3(b) show the intensity distribution summed over the 11 t' bins. It is similar to the one found by the VES experiment in a similar t' range [37] (blue data points). We do not observe a peak at $1.6\,\text{GeV}/c^2$ like in the BNL E852 21-wave PWA [41,42] [cf. blue data points in Fig. 3(a)]. Surprisingly, the t'-summed intensity distributions in Fig. 3(b) are different from the one obtained in the analysis of the COMPASS lead-target data [43] [blue points in Fig. 3(d)]. Naïvely, one could expect these intensity distributions to be similar because $t' > 0.1\,(\text{GeV}/c)^2$, i.e., far above the region corresponding to coherent scattering off the lead nucleus, and hence the beam pion scatters off quasi-free nucleons inside the nucleus. In the COMPASS proton-target data, the shape of the intensity distribution of the $1^{-+}1^+\rho(770)\pi P$ wave exhibits a surprisingly strong dependence on t' (see Fig. 13 shown in this paper and Fig. 43 in Ref. [46]), and confirms a similar observation made by Dzierba *et al.* [45]. At low t', the intensity distribution is dominated by a broad structure that extends from about 1.0 to $1.7\,\text{GeV}/c^2$. With increasing t', the structure becomes narrower and its maximum moves to about $1.6\,\text{GeV}/c^2$. Interestingly, for $t' \gtrsim 0.5\,(\text{GeV}/c)^2$ (i.e., above the kinematic range considered by Dzierba *et al.* [45]) the intensity distribution actually resembles the one that we obtained in the analysis of the COMPASS lead-target data in the range $0.1 < t' < 1.0\,(\text{GeV}/c)^2$ [see Fig. 3(d)].

In the COMPASS proton-target data, we observe slow phase motions of the $1^{-+}1^+\rho(770)\pi P$ wave with respect to other waves in the $1.6\,\text{GeV}/c^2$ region (see Fig. 44 in Ref. [46]). As an example, the red data points in Fig. 4 show the phase with respect to the $2^{-+}0^+ f_2(1270)\pi S$ wave. Compared to the rather large differences in the intensity distributions (see Fig. 3), the $m_{3\pi}$ dependence of the phases of the $1^{-+}1^+\rho(770)\pi P$ wave relative to other waves is more robust with respect to changes of the analysis model. The phase motion from the COMPASS proton-target data is less pronounced than the one observed by the BNL E852 collaboration but agrees qualitatively with the phase motions observed by Dzierba *et al.* and in the analysis of the COMPASS lead-target data. We have no explanation for the approximately $+60°$ offset of the phase motion reported by Dzierba *et al.* [45] with respect to the other analyses.[g]

The strong t' dependence of the shape of the intensity distribution hints at large contributions from nonresonant processes related, e.g., to the Deck effect [48]. This was confirmed by our resonance-model fit, which describes the partial-wave intensities and interference terms of 14 selected partial waves simultaneously [46]. The resonance-model fit was performed for the first time simultaneously in all t' bins with the resonance parameters, i.e., masses and widths, forced to be the same across the t' bins. In this t'-resolved approach, we exploit the in general different t' dependences of the resonant and nonresonant amplitudes to better disentangle the two contributions. This eventually yields more realistic estimates for the resonance parameters. The model reproduces the $1^{-+}1^+\rho(770)\pi P$ intensities and phase motions well by a t'-dependent interference between the $\pi_1(1600)$ and a nonresonant component.[h] The latter strongly changes

---

[g]The panels in Fig. 33 in Ref. [45] that correspond to the t' bins number 6 and 7 show the same data points. Thus it is unclear whether the shown phase motion is that of bin 6 or bin 7. However, this probably does not explain the phase offset with respect to the other analyses since the phase in the $m_{3\pi} = 1.6\,\text{GeV}/c^2$ region depends only weakly on t'.

[h]We parametrize the nonresonant amplitude using Eqs. (27) and (28) in Ref. [46]. This is a phenomenological parametrization in the form of a Gaussian in the two-body breakup momentum of the isobar-pion decay that was

shape, strength, and phase with t'. At low t', the intensity is dominated by the large nonresonant component, which interferes constructively with the $\pi_1(1600)$ at low masses. With increasing t', the strength of the nonresonant component decreases more quickly than that of the $\pi_1(1600)$ so that the latter becomes the dominant component. For $t' \gtrsim 0.5\,(\text{GeV}/c)^2$, i.e., in the two highest t' bins, the nonresonant component is small or even vanishing in the $1.6\,\text{GeV}/c^2$ mass region, and the broad peak in the data is nearly entirely described by the $\pi_1(1600)$. The resonance model is not able to reproduce a narrow enhancement at about $1.1\,\text{GeV}/c^2$, which appears at low t'. This structure is not accompanied by any phase motion and the intensity in this mass region is sensitive to details of the PWA model. This makes a resonance interpretation unlikely and we hence suspect this structure to be an artifact induced by imperfections in the analysis method. A similar observation has been made in the VES analysis [37]. A similar structure also appears in a more advanced PWA (see Sec. V and Fig. 8), where we significantly reduce the model bias introduced by the chosen parametrizations for the dynamic isobar amplitudes. Hence its appearance does not seem to be tightly related to how well the isobar amplitudes are described by the PWA model.

From the resonance-model fit, we obtain Breit-Wigner parameters of $m_{\pi_1(1600)} = 1600\,^{+110}_{-60}\,\text{MeV}/c^2$ and $\Gamma_{\pi_1(1600)} = 580\,^{+100}_{-230}\,\text{MeV}/c^2$. The quoted uncertainties are systematic only (see Ref. [46] for details on the performed studies); the statistical uncertainties are more than an order of magnitude smaller and hence negligible. Although the mass value agrees well with the one found in our analysis of the COMPASS lead-target data [43] (see Sec. IV), the width found in the proton-target data is considerably larger. The reason for this discrepancy is not understood. However, it could be related to the fact that relative to the $\pi_1(1600)$ the contribution from the nonresonant components is much larger in the proton-target data than in the lead-target data. Also, our resonance models, which we use to decompose the partial-wave amplitudes into coherent sums of Breit-Wigner resonances and nonresonant amplitudes, might render the resonance parameters process-dependent [61]. In addition, due to the much smaller data sample, the analysis of the lead-target data was performed by integrating over t' and by modeling the t' dependence of the partial-wave amplitudes according to Eq. (6). Therefore, a potential t' dependence of the shape of the $1^{-+}1^+\rho(770)\pi P$ amplitude was not taken into account. A recent coupled-channel analysis of COMPASS data on diffractively produced $\eta\pi^-$ and $\eta'\pi^-$ final states performed by the JPAC collaboration finds a resonance pole with parameters of $m_{\pi_1(1600)} = 1564 \pm 24\,(\text{stat.}) \pm 86\,(\text{sys.})\,\text{MeV}/c^2$ and $\Gamma_{\pi_1(1600)} = 492 \pm 54\,(\text{stat.}) \pm 102\,(\text{sys.})\,\text{MeV}/c^2$ [40] that are more consistent with the Breit-Wigner parameters we find in the COMPASS proton-target data.

Are the different results from previous analyses, in particular the two analyses based on BNL E852 data, caused by inconsistencies of the data or by the different PWA models? In order to answer this question, we investigate the impact of the different analysis models used for the BNL E852 data, by applying the 21-wave set from Refs. [41, 42] and the 36-wave set from Ref. [45] (see Table 4 in Appendix A) to the high-precision COMPASS proton-target data sample keeping the subdivision into 11 t' bins. The red data points in Fig. 3(a) show the t'-summed intensity distribution of the $1^{-+}1^+\rho(770)\pi P$ wave as obtained from the PWA using the 21-wave set. The intensity distribution exhibits a clear peak slightly above $1.6\,\text{GeV}/c^2$, similar to the signal found in the BNL E852 analysis in Refs. [41, 42] (blue data points). In the low-mass region, the intensities from the two analyses shown in Fig. 3(a) are not directly comparable. The COMPASS acceptance is much more uniform than the acceptance of the BNL E852 experiment and hence leakage induced by the experimental acceptance is much suppressed. We also confirm the finding of Dzierba *et al.* that the $1.6\,\text{GeV}/c^2$ peak vanishes by applying the 36-wave set to the COMPASS proton-target data. As an example, we compare in Fig. 3(c) the intensity

inspired by Ref. [60].

distributions around $t' = 0.2\,(\mathrm{GeV}/c)^2$. Consequently, our data support the conclusion from Ref. [45] that the $1.6\,\mathrm{GeV}/c^2$ peak observed in Refs. [41, 42] is an artificial structure caused by using a wave set that misses important waves. This conclusion is further supported by the fact that using the 21-wave set we find contrary to the expected dominance of natural-parity exchange a peak of similar height in the same mass region in the $1^{-+}1^{-}\rho(770)\pi P$ wave, which has negative reflectivity corresponding to unnatural-parity exchange. This has also been pointed out by VES [37].

Our t'-resolved analysis using the 88-wave set also confirms the finding of Dzierba *et al.* that the $\pi_1(1600)$ signal is weak compared to the nonresonant component in the range $t' \lesssim 0.5\,(\mathrm{GeV}/c)^2$. In the range $t' < 0.53\,(\mathrm{GeV}/c)^2$ analyzed in Ref. [45], we find that the $\pi_1(1600)$ signal is masked by the dominant contributions from nonresonant processes. However, our analysis contradicts the conclusion from Ref. [45] that there is no evidence for the $\pi_1(1600)$ in 3π. The COMPASS proton-target data require a $\pi_1(1600)$ resonance in the range $t' \gtrsim 0.5\,(\mathrm{GeV}/c)^2$ and also the COMPASS lead-target data cannot be described without a $\pi_1(1600)$.

It is not yet understood why the $\pi_1(1600)$ signal is enhanced with respect to the nonresonant component in the lead-target data as compared to our proton-target data. However, we do observe a general enhancement of the intensity of waves with spin projection $M = 1$ over those with $M = 0$ in the lead-target data [50].

B   Summary: previous results and comparison with COMPASS data

Using our highly precise COMPASS proton-target data we reproduce the key PWA results of all previous analyses of the $1^{-+}1^{+}\rho(770)\pi P$ wave by applying their analysis models. We conclude that this wave contains a $\pi_1(1600)$ signal and that the discrepancies and mutual inconsistencies observed in previous analyses originate either from model artifacts or from studying too restricted t' ranges. The PWA model with 21 waves used in Refs. [41, 42] contained too few waves leading to an artificial peak being misinterpreted as the $\pi_1(1600)$. The analysis in Ref. [45] excluded the region $t' > 0.53\,(\mathrm{GeV}/c)^2$ and hence missed the region, in which the $\pi_1(1600)$ signal rises above the nonresonant background. Since the VES analysis was not performed in t' bins, their $\pi_1(1600)$ signal was also diluted by large nonresonant contributions.

A remaining puzzle is that in $\gamma + \pi^{\pm} \to \pi^{\pm}\pi^{-}\pi^{+}$ reactions the production of the $\pi_1(1600)$ seems to be much less prominent than expected considering vector-meson dominance and the observation of the $\rho(770)\pi$ decay.[i] The CLAS [62, 63] and the COMPASS Primakoff experiment [64, 65] find nearly vanishing intensities of the 1^{-+} wave in the $1.6\,\mathrm{GeV}/c^2$ mass region. This, however, could in principle be due to destructive interference of a $\pi_1(1600)$ with a nonresonant component—a hypothesis that could be verified by resonance-model fits. In the future, much more precise photoproduction data from Jefferson Laboratory will help to clarify the situation.

V   Study of dynamic isobar amplitudes

The partial-wave analyses of the 3π final state performed so far (see Sec. IV) used the conventional isobar model where isobar resonances are described using fixed parametrizations for their dynamic amplitude $\Delta(m_\xi)$ (see Sec. III) with resonance parameters taken from previous experiments [20]. Even though this approach is quite common, it might introduce a model bias in the analysis because the fixed dynamic amplitudes might deviate from the true ones present in real data. The differences could be due to distortions of the two-particle dynamic amplitudes, caused by the

---

[i]The absolute partial width $\pi_1(1600) \to \rho(770)\pi$ is currently unknown. However, our results suggest that the branching fraction might be in the percent region.

presence of the third pion, or due to contributions from excited isobar resonances or nonresonant processes.

To study this possible bias in our PWA model, we re-analyze our data set using the freed-isobar PWA method presented in detail in Refs. [49, 66]. This analysis technique no longer relies on fixed parametrizations for the dynamic isobar amplitudes, but allows to extract these amplitudes from the data themselves with much reduced model dependence. In this approach, the fixed parametrization for the dynamic amplitude $\Delta_a(m_\xi)$ of an isobar ξ in wave a (see Eq. (5)) is replaced by a set of piecewise constant amplitudes defined over a contiguous set of intervals in the $\pi^-\pi^+$ mass m_ξ that are indexed by k, i.e.,[j]

$$\Delta_a(m_\xi) = \sum_k \mathscr{T}_{a,k} \, \Pi_{k,\xi}(m_\xi) \quad \text{with} \quad \Pi_{k,\xi}(m_\xi) = \begin{cases} 1, & \text{if } m_{k,\xi} \le m_\xi < m_{k+1,\xi}, \\ 0, & \text{otherwise.} \end{cases} \tag{7}$$

This way, the dynamic amplitude for isobar ξ is approximated by the set $\{\mathscr{T}_{a,k}\}$ of complex-valued constants. This method allows us not only to estimate the model bias caused by the fixed dynamic isobar amplitudes in our PWA model, but also to study the dynamic isobar amplitudes themselves.

In our PWA model, we factorize the decay amplitude Ψ_a of partial wave a in Eq. (4) into the dynamic isobar amplitude Δ_a and an angular amplitude $\mathcal{K}_a$. Including the Bose symmetrization with respect to the two indistinguishable π^- in the $\pi_1^-\pi_2^-\pi_3^+$ final state, we write for a given $(m_{3\pi}, t')$ cell (see Eq. (47) in Ref. [47]):[k]

$$\Psi_a(\tau_{13}, \tau_{23}) = \mathcal{K}_a(\tau_{13}) \, \Delta_a(m_{13}) + \mathcal{K}_a(\tau_{23}) \, \Delta_a(m_{23}). \tag{8}$$

It is important that Δ_a depends only on the invariant mass m_{ij} of the $\pi_i^-\pi_j^+$ subsystems forming the isobar and that $\mathcal{K}_a$ depends only on the four angular variables in the set of five phase-space variables of the three-body system represented by τ_{ij} (see Sec. III A in Ref. [47] for details on the definition of the coordinate systems). Inserting Eq. (7) into Eq. (8) and defining separate transition and decay amplitudes for every $\pi^-\pi^+$ mass interval k via

$$\mathcal{T}_{a,k} \equiv \mathcal{T}_a \, \mathscr{T}_{a,k} \tag{9}$$

and

$$\Psi_{a,k}(\tau_{13}, \tau_{23}) \equiv \mathcal{K}_a(\tau_{13}) \, \Pi_{k,\xi}(m_{13}) + \mathcal{K}_a(\tau_{23}) \, \Pi_{k,\xi}(m_{23}), \tag{10}$$

the expression for the intensity distribution in Eq. (4) can be written as[l]

$$\mathcal{I}(\tau_{13}, \tau_{23}) = \left| \sum_a \sum_k \mathcal{T}_{a,k} \, \Psi_{a,k}(\tau_{13}, \tau_{23}) \right|^2 + \mathcal{I}_{\text{flat}}. \tag{11}$$

Note that although Eq. (11) contains an additional sum over the two-pion mass intervals k, the mathematical structure is exactly the same as in Eq. (4). We can thus use the same extended maximum likelihood approach to determine the set $\{\mathcal{T}_{a,k}\}$ of the unknown fit parameters from the data.

---

[j]In the following, we discuss PWA models with rank 1 and waves with positive reflectivity. We hence omit the ε and r indices from here onwards.

[k]The angular amplitude is that part of the decay amplitude, which depends only on the decay angles and not on $m_{3\pi}$ or $m_{\pi^-\pi^+}$. It is given by Eqs. (11) and (7) in Ref. [47] without the dynamic parts $f_{\lambda 0}^J$ and $f_{0\,0}^{J\xi}$.

[l]See footnote [j].

Performing a freed-isobar PWA in $(m_{3\pi}, t')$ cells, yields transition amplitudes $\mathcal{T}_{a,k}(m_{3\pi}, t') = \mathcal{T}_a(m_{3\pi}, m_\xi, t')$ that now depend not only on $m_{3\pi}$ and t' but also on m_ξ via the index k. According to Eq. (9), a freed-isobar transition amplitude contains information on both the 3π system and the $\pi^-\pi^+$ subsystem. For each freed-isobar wave in the PWA model and each $(m_{3\pi}, t')$ cell, the method yields an Argand diagram ranging in m_ξ from $2m_\pi$ to $m_{3\pi} - m_\pi$. It is important to note that in the freed-isobar approach, we do not make any assumptions on the resonance content of the $\pi^-\pi^+$ subsystem. The freed-isobar PWA thus allows us to determine from the data the overall amplitude of all $\pi^-\pi^+$ intermediate states with given J^{PC} quantum numbers in the 3π partial wave defined by a. This amplitude hence includes in principle all contributing $\pi^-\pi^+$ resonances, potential nonresonant contributions, as well as distortions due to final-state interactions. Note that a $\pi^-\pi^+$ system with even relative orbital angular momentum, i.e., even J, has $I^G J^{PC}$ quantum numbers $0^+ J^{++}$, which correspond to f_J states, or $2^+ J^{++}$, which would be flavor-exotic. A $\pi^-\pi^+$ system with odd relative orbital angular momentum, i.e., odd J, has $I^G J^{PC}$ quantum numbers $1^+ J^{--}$, which correspond to ρ_J states.

In the ansatz in Eq. (11), we sum coherently over the index k of the $m_{\pi^-\pi^+}$ intervals. This takes into account the interference of the amplitudes in different $m_{\pi^-\pi^+}$ intervals due to Bose symmetrization of the final-state particles. This is conceptually different from the binning in $m_{3\pi}$ and t', where all kinematic bins are independent.

The obtained dynamic isobar amplitudes can be different for every wave a, even though they might describe $\pi^-\pi^+$ subsystems with the same relative orbital angular momentum. The reduced model dependence of the freed-isobar method and the additional information on the $\pi^-\pi^+$ subsystems come at the price of a considerably larger number of fit parameters compared to the conventional fixed-isobar PWA. Thus even for large data sets, the freed-isobar approach is feasible only when it is applied to a selected subset of partial waves in the PWA model, while for the remaining partial waves the conventional fixed isobar parametrizations are used.

Based on the COMPASS proton-target data, we have performed a freed-isobar PWA already in Ref. [47] to extract the dynamic $\pi^-\pi^+$ S-wave amplitudes in three different 3π partial waves.

A   Freed-isobar analysis model

In the following, we apply the freed-isobar method to the $1^{-+}1^+\rho(770)\pi P$ wave. Since this wave has a low relative intensity of only $0.8\,\%$ it is prone to potential leakage effects. Therefore, it does not suffice to free the dynamic isobar amplitude only in the 1^{-+} wave. Small imperfections in the description of the dynamic isobar amplitudes of waves with much higher relative intensity could create tensions between model and data, which in turn could induce leakage into the freed 1^{-+} wave due to its high flexibility.

Therefore, we free all 12 waves of our 88-wave PWA model (see Table 4 in Appendix A), that obtained a relative intensity of more than $1\,\%$ in the conventional PWA. In addition to these 12 waves, we free the $1^{-+}1^+\rho(770)\pi P$ wave to study its 1^{--} dynamic isobar amplitude. The 88-wave PWA model contains subsets of waves with identical quantum numbers but different $I^G J^{PC} = 0^+ 0^{++}$ isobar resonances. Such waves are absorbed in a single freed-isobar wave with $J^{PC} = 0^{++}$ of the $\pi^-\pi^+$ subsystem (indicated by the brackets in Table 2). As a consequence, 3 additional waves with a relative intensity below $1\,\%$ are also freed. In total, we replace the dynamic isobar amplitudes of 16 of the original 88 fixed-isobar waves by 12 waves with freed-isobar amplitudes (see Tables 2 and 4); 72 waves with fixed dynamic isobar amplitudes remain in the freed-isobar PWA model. In the conventional fixed-isobar PWA, the intensity sum of the 16 freed waves accounts for $83.3\,\%$ of the total intensity.

For the freed-isobar waves, we choose $m_{\pi^-\pi^+}$ intervals with a width of $40\,\mathrm{MeV}/c^2$ except in the

Table 2: Waves in the freed-isobar PWA model with dynamic isobar amplitudes parametrized according to Eq. (7). The notation $[\pi\pi]_{JPC}$ represents a $\pi^-\pi^+$ subsystem with well-defined J^{PC} quantum numbers.[m] The center column lists the corresponding waves in the conventional 88-wave fixed-isobar PWA (see Table 4 in Appendix A) and the right column their relative intensity as obtained in Ref. [47].

Freed wave	Fixed wave(s)	Relative intensity
$0^{-+}0^+[\pi\pi]_{0^{++}}\pi S$	$0^{-+}0^+[\pi\pi]_S\pi S$	8.0 %
	$0^{-+}0^+f_0(980)\pi S$	2.4 %
	$0^{-+}0^+f_0(1500)\pi S$	0.1 %
$0^{-+}0^+[\pi\pi]_{1^{--}}\pi P$	$0^{-+}0^+\rho(770)\pi P$	3.5 %
$1^{++}0^+[\pi\pi]_{0^{++}}\pi P$	$1^{++}0^+[\pi\pi]_S\pi P$	4.1 %
	$1^{++}0^+f_0(980)\pi P$	0.3 %
$1^{++}0^+[\pi\pi]_{1^{--}}\pi S$	$1^{++}0^+\rho(770)\pi S$	32.7 %
$1^{++}1^+[\pi\pi]_{1^{--}}\pi S$	$1^{++}1^+\rho(770)\pi S$	4.1 %
$1^{-+}1^+[\pi\pi]_{1^{--}}\pi P$	$1^{-+}1^+\rho(770)\pi P$	0.8 %
$2^{++}1^+[\pi\pi]_{1^{--}}\pi D$	$2^{++}1^+\rho(770)\pi D$	7.7 %
$2^{-+}0^+[\pi\pi]_{0^{++}}\pi D$	$2^{-+}0^+[\pi\pi]_S\pi D$	3.0 %
	$2^{-+}0^+f_0(980)\pi D$	0.6 %
$2^{-+}0^+[\pi\pi]_{1^{--}}\pi P$	$2^{-+}0^+\rho(770)\pi P$	3.8 %
$2^{-+}1^+[\pi\pi]_{1^{--}}\pi P$	$2^{-+}1^+\rho(770)\pi P$	3.3 %
$2^{-+}0^+[\pi\pi]_{1^{--}}\pi F$	$2^{-+}0^+\rho(770)\pi F$	2.2 %
$2^{-+}0^+[\pi\pi]_{2^{++}}\pi S$	$2^{-+}0^+f_2(1270)\pi S$	6.7 %
	Intensity sum	**83.3 %**

[m]In the fixed-isobar PWA, $[\pi\pi]_S$ represents a parametrization for the broad component of the $\pi^-\pi^+$ S-wave amplitude based on Ref. [67] (see Sec. III A in Ref. [47] for details).

Table 3: Borders of the four nonequidistant t' bins, in which the freed-isobar PWA is performed. The intervals are chosen such that each bin contains approximately 11.5×10^6 events.

Bin	1	2	3	4
t' [(GeV/c)^2]	0.100	0.141	0.194	0.326	1.000

regions of the known $\rho(770)$, $f_0(980)$, and $f_2(1270)$ resonances, where we use a finer binning. For the waves with $J^{PC} = 1^{--}$ isobars, we use an interval width of $20 \, \text{MeV}/c^2$ in the range from 0.64 to $0.92 \, \text{GeV}/c^2$.[n] Our freed-isobar PWA model (see Table 2) has a much larger number of fit parameters than the conventional fixed-isobar PWA.[o] In order to sufficiently constrain the fit parameters by data, we increase the $m_{3\pi}$ bin width from $20 \, \text{MeV}/c^2$ in the fixed-isobar PWA to $40 \, \text{MeV}/c^2$ in the freed-isobar PWA and reduce in addition the number of t' bins from 11 to 4 (see Table 3). We thus decrease the total number of kinematic ($m_{3\pi}, t'$) cells in the analyzed range from 1100 in the fixed-isobar PWA to 200 in the freed-isobar PWA. All other parameters of the PWA remain as described in Ref. [47]. For the $m_{3\pi}$ bins below $0.98 \, \text{GeV}/c^2$, the results from the freed-isobar PWA turn out to be not well-determined by the data. This is probably related to the fact that this $m_{3\pi}$ region corresponds to the range $m_{\pi^-\pi^+} \lesssim 0.8 \, \text{GeV}/c^2$ where most isobar resonances, which otherwise stabilize the fit, are absent. Therefore, we exclude this $m_{3\pi}$ range from the following analysis.

In a freed-isobar PWA mathematical ambiguities, so-called zero modes, may arise at the level of the decay amplitudes leading to ambiguous solutions for the transition amplitudes $\{\mathcal{T}_{a,k}\}$. These ambiguities can be resolved by imposing conditions on the $m_{\pi^-\pi^+}$ dependence of the dynamic isobar amplitudes [49, 66]. We give details on the zero mode in the $1^{-+}1^+[\pi\pi]_{1^{--}}\pi P$ wave and its resolution in Appendix B. The zero modes are confined to sectors with the same $J^{PC} M^\varepsilon$ quantum numbers of the 3π system. Therefore, similar ambiguities present in other waves have no influence on the results extracted for the spin-exotic wave. In the following, we will discuss only zero-mode corrected results.

B Freed-isobar results for the $J^{PC} = 1^{-+}$ wave

In the following, we will present results for the $1^{-+}1^+[\pi\pi]_{1^{--}}\pi P$ wave obtained from the freed-isobar PWA with 12 freed waves as listed in Tables 2 and 4. Figure 5 shows the partial-wave intensities $|\overline{\mathcal{T}}_{a,k}|^2$ for the four t' bins listed in Table 3. Here, the

$$\overline{\mathcal{T}}_{a,k} = \frac{\mathcal{T}_{a,k}}{\sqrt{w_k}} \tag{12}$$

are the transition amplitudes for the $m_{\pi^-\pi^+}$ intervals k [see Eqs. (7) and (9)] normalized by the width w_k of the intervals. We observe a clear correlation of the $m_{3\pi}$ distribution of the 3π system with $I^G J^{PC} M^\varepsilon = 1^- 1^{-+}1^+$ with the $m_{\pi^-\pi^+}$ distribution of the $\pi^-\pi^+$ subsystem with $I^G J^{PC} = 1^- 1^{--}$. The $m_{\pi^-\pi^+}$ spectra are dominated by a peak in the $\rho(770)$ region. The shape of the $m_{3\pi}$ spectrum in the $\rho(770)$ region depends strongly on t'. At low t', it is characterized by a broad structure peaking at low values of $m_{3\pi}$ around $1.1 \, \text{GeV}/c^2$. A similar enhancement is observed in the conventional fixed-isobar PWA (see Sec. IV A). The freed-isobar PWA shows that this enhancement indeed contains mainly $\rho(770)\pi$ (see discussion below). With increasing t',

---

[n]For $J^{PC} = 0^{++}$ isobars, we use an interval width of $10 \, \text{MeV}/c^2$ in the range from 0.92 to $1.08 \, \text{GeV}/c^2$; for $J^{PC} = 2^{++}$, an interval width of $20 \, \text{MeV}/c^2$ from 1.18 to $1.40 \, \text{GeV}/c^2$.

[o]In the highest $m_{3\pi}$ bin at $2.48 \, \text{GeV}/c^2$, the number of free parameters in the freed-isobar PWA is 1520. This number decreases with decreasing $m_{3\pi}$ because fewer $m_{\pi^-\pi^+}$ intervals are kinematically allowed. In the same $m_{3\pi}$ bin, the 88-wave fixed-isobar PWA model (see Table 4 in Appendix A) has 184 free parameters.
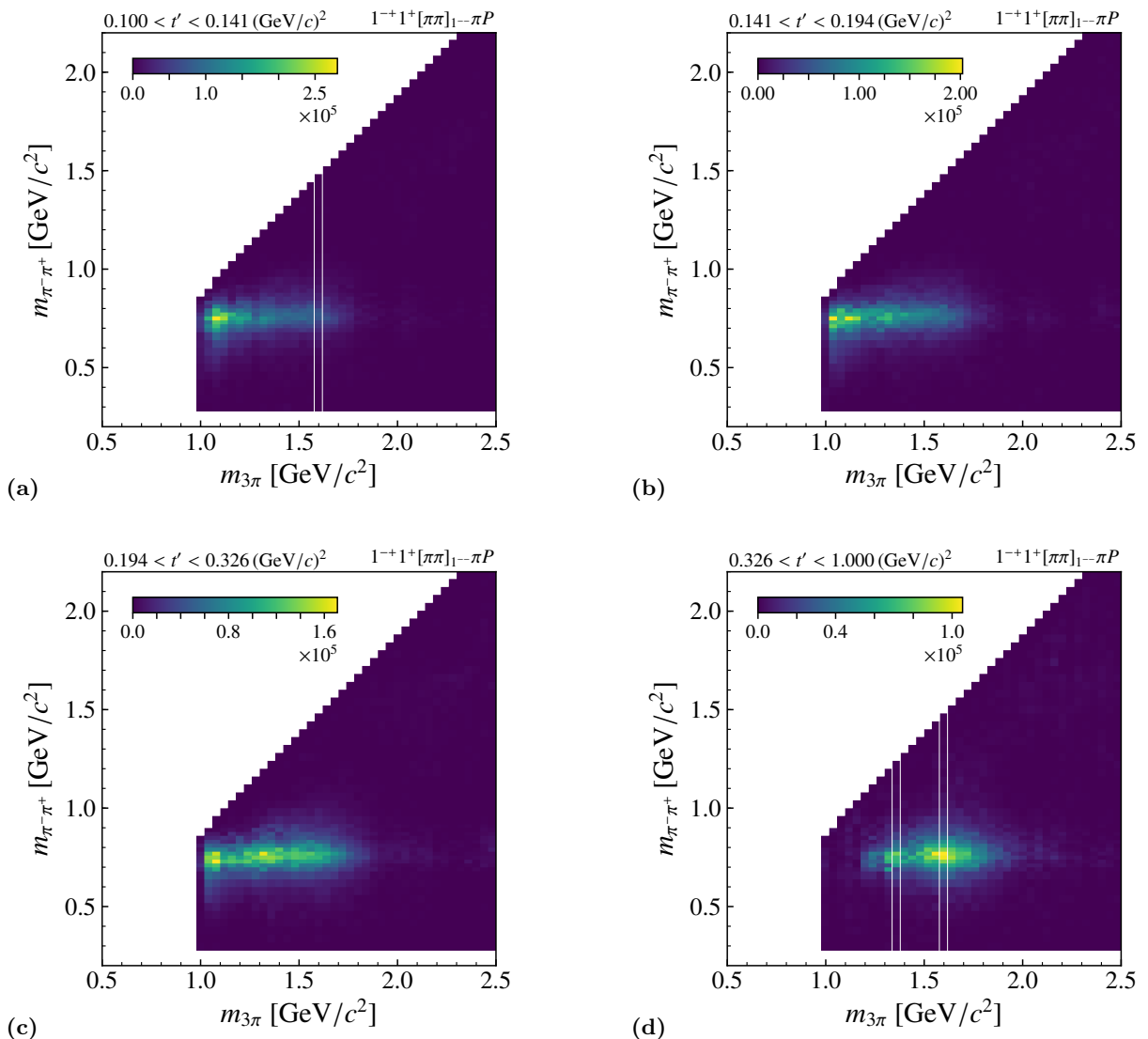
FIG. 5: Two-dimensional intensity distribution of the $1^{-+}1^{+}[\pi\pi]_{1^{--}}\pi P$ wave obtained in the freed-isobar PWA (after correction for the zero mode) as a function of $m_{3\pi}$ and $m_{\pi^{-}\pi^{+}}$ for all four t' bins. The color scale represents the intensity in units of number of events per $40\,\mathrm{MeV}/c^2$ interval in $m_{\pi^{-}\pi^{+}}$ and in $m_{3\pi}$. The white vertical lines indicate the $m_{3\pi}$ bins shown in Fig. 6.

the intensity in the low-mass region decreases quickly and in the highest t' bin, a peak emerges in the $m_{3\pi} = 1.6\,\mathrm{GeV}/c^2$ region [see Fig. 5(d)].

The left column of Fig. 6 shows the intensity distributions as a function of $m_{\pi^{-}\pi^{+}}$ for selected $m_{3\pi}$ bins that are indicated by vertical lines in Fig. 5. The mass bin $1.34 < m_{3\pi} < 1.38\,\mathrm{GeV}/c^2$ is dominated by nonresonant contributions, whereas the bin $1.58 < m_{3\pi} < 1.62\,\mathrm{GeV}/c^2$ lies in the $\pi_1(1600)$ resonance region. For the low-mass region, we show, as an example, only the data in the highest t' bin, while for the $\pi_1(1600)$ resonance region, we present the results for the lowest and the highest of the four t' bins.

Since the freed-isobar PWA extracts the amplitude as a function of $m_{3\pi}$ and $m_{\pi^{-}\pi^{+}}$, we have also information about the phase as a function of $m_{\pi^{-}\pi^{+}}$. This is shown in the right column of Fig. 6 in the form of Argand diagrams for the selected $m_{3\pi}$ bins. The dominant $\rho(770)$ peak in the intensity spectra corresponds to a clear circular structure in the Argand diagrams with a phase
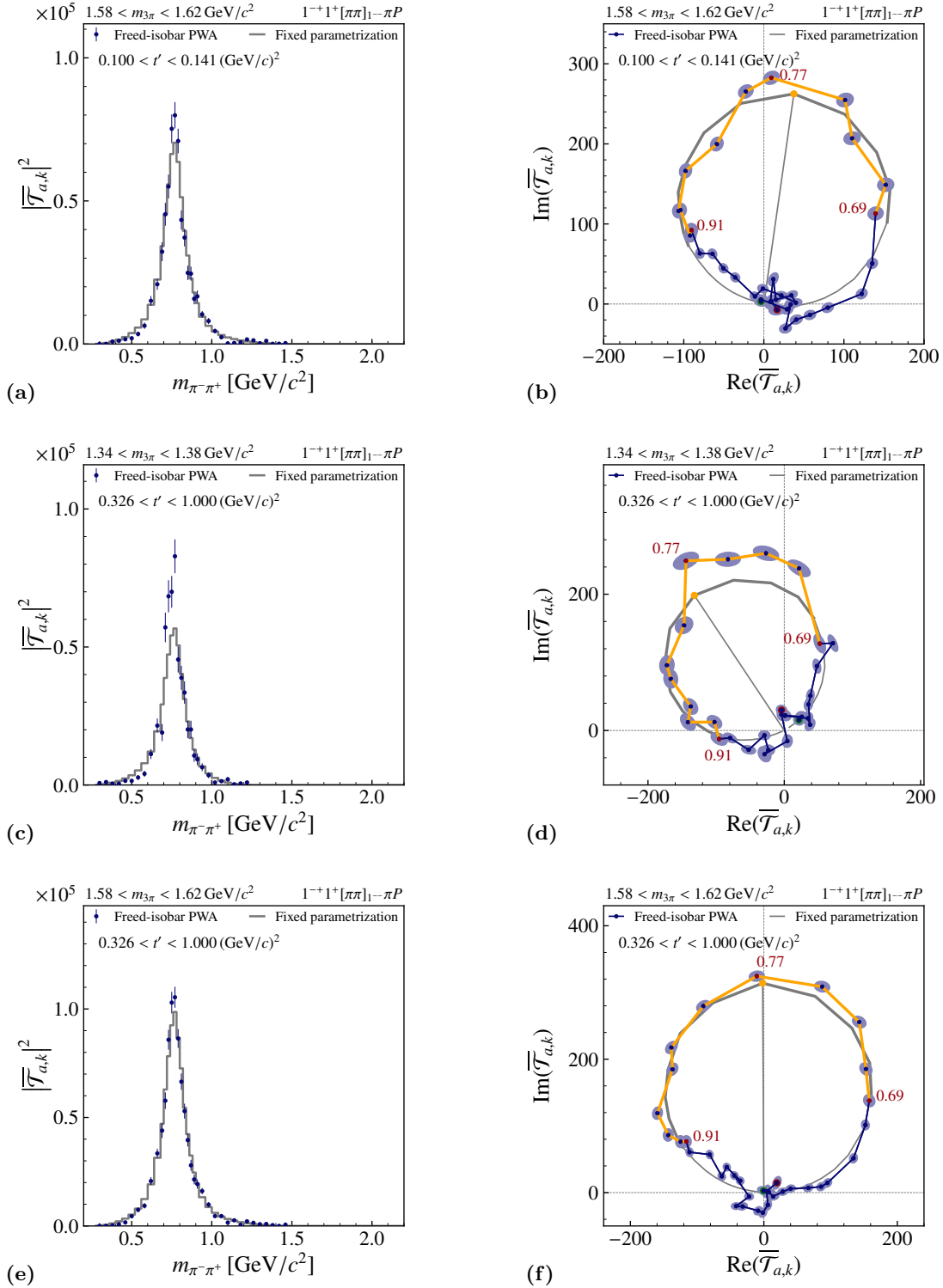
FIG. 6: The $[\pi\pi]_{1^{--}}$ dynamic isobar amplitude in the $1^{-+}1^+[\pi\pi]_{1^{--}}\pi P$ wave as a function of $m_{\pi^-\pi^+}$ for selected $m_{3\pi}$ and t' bins. Left column: intensities; Right column: Argand diagrams. The blue data points with error bars or error ellipses, respectively, are the result of the freed-isobar PWA corrected for the zero mode. In the Argand diagrams, the data points are connected by lines to indicate the order and the red numbers correspond to $m_{\pi^-\pi^+}$ values in GeV/c^2. The line segments highlighted in orange correspond to the $m_{\pi^-\pi^+}$ range from 0.64 to $0.92\,\mathrm{GeV}/c^2$ around the $\rho(770)$. The overall phase of the Argand diagrams is fixed by the $4^{++}1^+\rho(770)\pi G$ wave. For comparison, the fixed parametrization of the dynamic isobar amplitude for the $\rho(770)$ as used in the conventional PWA is shown by the gray lines with the $\rho(770)$ region indicated by thicker lines. In the Argand diagrams, the orange point indicates the nominal $\rho(770)$ mass and the green- and red-circled points indicate the lowest and the highest $m_{\pi^-\pi^+}$ interval, respectively.

motion by about 180°. This confirms, that the presence of the $\rho(770)$ has not been artificially enforced by the fixed parametrizations of the dynamic isobar amplitudes as used in previous analyses. Just as the $m_{\pi^-\pi^+}$ spectra, also the Argand diagrams exhibit no strong dependence on $m_{3\pi}$ or t'. The spin-exotic wave is clearly dominated by the $\rho(770)$ over the full $m_{3\pi}$ region and in all four t' bins.

We study the freed-isobar transition amplitudes that we extracted from the data in terms of isobar resonances and possible distortions. In a first study, we investigate the $\rho(770)$ resonance in the presence of another pion, which together form a 3π system with $J^{PC} = 1^{-+}$. Lacking an elaborate model, we perform this study by fitting the $J^{PC} = 1^{--}$ dynamic isobar amplitudes with a $\rho(770)$ Breit-Wigner model of the form

$$\hat{\mathcal{T}}_a(m_{\pi^-\pi^+}; m_{3\pi}, t') = \mathcal{C}_a(m_{3\pi}, t')\, \frac{\mathcal{N}_a(m_{3\pi}, m_{\pi^-\pi^+})}{m_{\rho(770)}^2 - m_{\pi^-\pi^+}^2 - i\, m_{\rho(770)} \Gamma(m_{\pi^-\pi^+})} \tag{13}$$

in every $(m_{3\pi}, t')$ cell independently. Here, $a = 1^{-+}1^+[\pi\pi]_{1^{--}}\pi P$, $\mathcal{N}_a(m_{3\pi}, m_{\pi^-\pi^+})$ is a normalization factor, which takes into account the variation of the $m_{\pi^-\pi^+}$ bin width, the self-interference of the Breit-Wigner amplitude due to Bose symmetrization, and the angular-momentum barrier factors $F_L(m_{3\pi}; m_{\pi^-\pi^+}, m_\pi)$ and $F_{J_\xi}(m_{\pi^-\pi^+}; m_\pi, m_\pi)$ from Eqs. (10) and (8) of Ref. [47], and $\Gamma(m_{\pi^-\pi^+})$ is the mass-dependent total width of the $\rho(770)$ as given by Eq. (40) in Ref. [47]. In the fits, the resonance parameters $m_{\rho(770)}$ and $\Gamma_{\rho(770)}$ are fixed to the values used in the conventional fixed-isobar PWA (see Tab. III in Ref. [47]). The only free fit parameter is the complex-valued coupling $\mathcal{C}_a(m_{3\pi}, t')$, which determines strength and phase of the $\rho(770)$ signal in the given $(m_{3\pi}, t')$ cell, i.e., radius and rotation of the resonance circle about the origin in the Argand diagram. The model is evaluated at those $m_{\pi^-\pi^+}$ values that correspond to the centers of the $m_{\pi^-\pi^+}$ intervals defined in Eq. (7).

The fits are limited to the region $m_{\pi^-\pi^+} < 1.12\,\mathrm{GeV}/c^2$ to avoid bias from excited ρ resonances at higher masses. The results of these fits are shown as gray curves in Fig. 6.[p] The resulting curves are in good agreement with the extracted dynamic isobar amplitudes in the $m_{3\pi}$ region of the $\pi_1(1600)$, which confirms the validity of the isobar model. For the lower $m_{3\pi}$ bin shown, the agreement is slightly worse, which could hint at a stronger influence of nonresonant contributions in this mass region.

In a second study, we let the $\rho(770)$ resonance parameters float in the fit and determine them independently for every $(m_{3\pi}, t')$ cell. We hence do not assume anymore that we can factorize the $m_{\pi^-\pi^+}$ dependence of the transition amplitudes from their $m_{3\pi}$ and t' dependence. The weighted average of the obtained $\rho(770)$ mass values is about $760\,\mathrm{MeV}/c^2$, only slightly below the PDG averages. The weighted average of the obtained $\rho(770)$ width values is approximately $130\,\mathrm{MeV}/c^2$, which lies 15 to $20\,\mathrm{MeV}/c^2$ below the PDG averages. We have currently no explanation why the $\rho(770)$ in the 1^{-+} wave appears so much narrower.[q] The $\rho(770)$ parameters exhibit variations of about $\pm 10\,\%$ with $m_{3\pi}$ (see Fig. 7), while they show little variation with t' [66]. More advanced models are needed to study the distortion of the $\rho(770)$ line shape due to effects of final-state interaction and interfering contributions from nonresonant processes in the $\pi^-\pi^+$ system.

---

[p]These fits also resolve the mathematical ambiguity discussed in Sec. V A. This is explained in detail in Appendix B.

[q]Allowing the range parameter q_R (see below Eq. (39) in Ref. [47]) of the angular-momentum barrier factor F_{J_ξ} of the $\rho(770)$ decay as an additional free fit parameter, yields slightly larger width values in some $m_{3\pi}$ regions. However, qualitatively the picture remains unchanged.
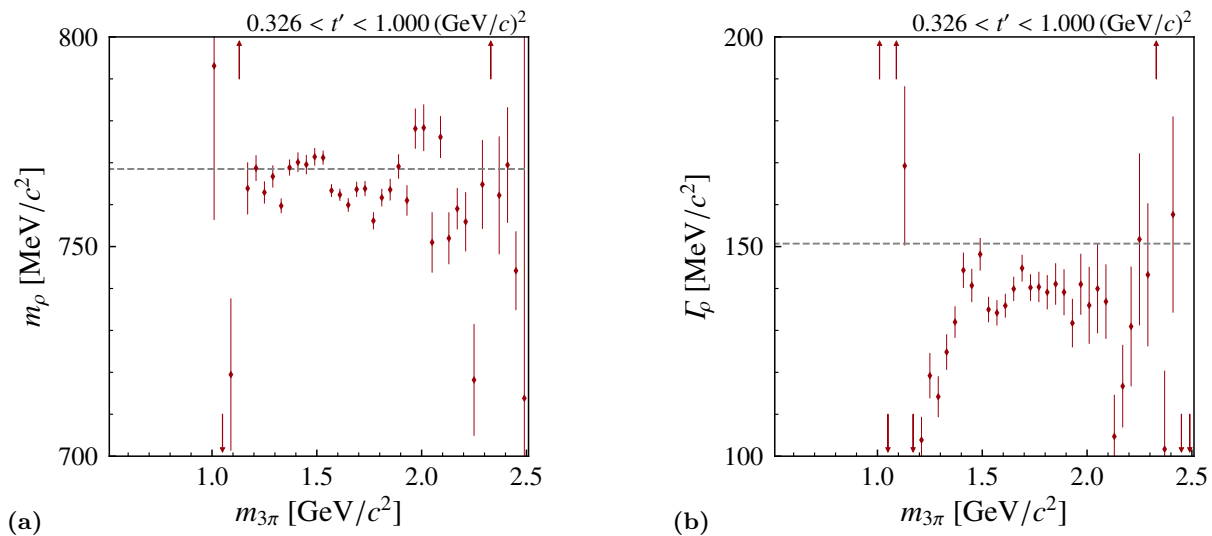
FIG. 7: Parameters of the $\rho(770)$ resonance obtained by fitting the $J^{PC} = 1^{--}$ dynamic isobar amplitudes of the spin-exotic wave from the freed-isobar PWA. The fit is performed independently in every $(m_{3\pi}, t')$ cell; the results shown are for the highest t' bin. (a) shows the $\rho(770)$ mass and (b) the $\rho(770)$ width. The gray lines indicate the corresponding parameter values used in the conventional PWA.

C   Comparison with the conventional partial-wave analysis

In order to directly compare the results from the freed-isobar PWA with the conventional PWA with fixed parametrizations for the dynamic isobar amplitudes, we repeated the latter with the same 88-wave PWA model as in Ref. [47] but applying the coarser binning in $m_{3\pi}$ and t' from the freed-isobar PWA (see Sec. V A and Table 3). From the result of the freed-isobar PWA, we obtain intensity distributions as a function of $m_{3\pi}$ and t' alone by summing the contributions of the freed-isobar transition amplitudes $\{\mathcal{T}_{a,k}\}$ [see Eqs. (7) and (9)] from all $m_{\pi^-\pi^+}$ intervals coherently. Doing so, we take into account the interference of amplitudes in different $m_{\pi^-\pi^+}$ intervals, i.e., the so-called overlaps, that arise due to Bose symmetrization of the final-state particles. The intensity of these coherent sums is by definition not affected by the zero-mode ambiguity mentioned in Sec. V A (see also Appendix B).

In Fig. 8, we overlay the intensity distributions from the freed-isobar PWA obtained as described above (orange data points) with the corresponding distributions from the conventional fixed-isobar PWA (blue data points). Although the 1^{-+} wave contributes only about $1\,\%$ to the total intensity, the distributions are surprisingly similar. The shapes of the intensity distributions are consistent in both approaches, regardless of the t' bin. However, the intensity of the 1^{-+} wave is higher for the freed-isobar PWA. This intensity increase is not caused by freeing the dynamic isobar amplitude of the 1^{-+} wave itself, but rather by the other 11 freed-isobar waves (see Table 2). Keeping these 11 freed waves but fixing the dynamic isobar amplitude in the 1^{-+} wave to the $\rho(770)$, like in the conventional PWA, yields basically the same 1^{-+} intensity distribution as in the PWA with 12 freed waves. Further systematic studies show that no single freed wave causes the increase of the 1^{-+} intensity, but that this is the result of the interplay of all 11 freed waves. This suggests that—unlike for the 1^{-+} wave—the fixed-isobar amplitudes, which in the conventional 88-wave PWA correspond to the these 11 freed-isobar waves, do not match the data completely. Deviations could be caused, for example, by unsuitable parametrizations and/or parameters used for the dynamic isobar amplitudes or by neglecting higher excited isobar resonances that may become relevant at higher values of $m_{3\pi}$.
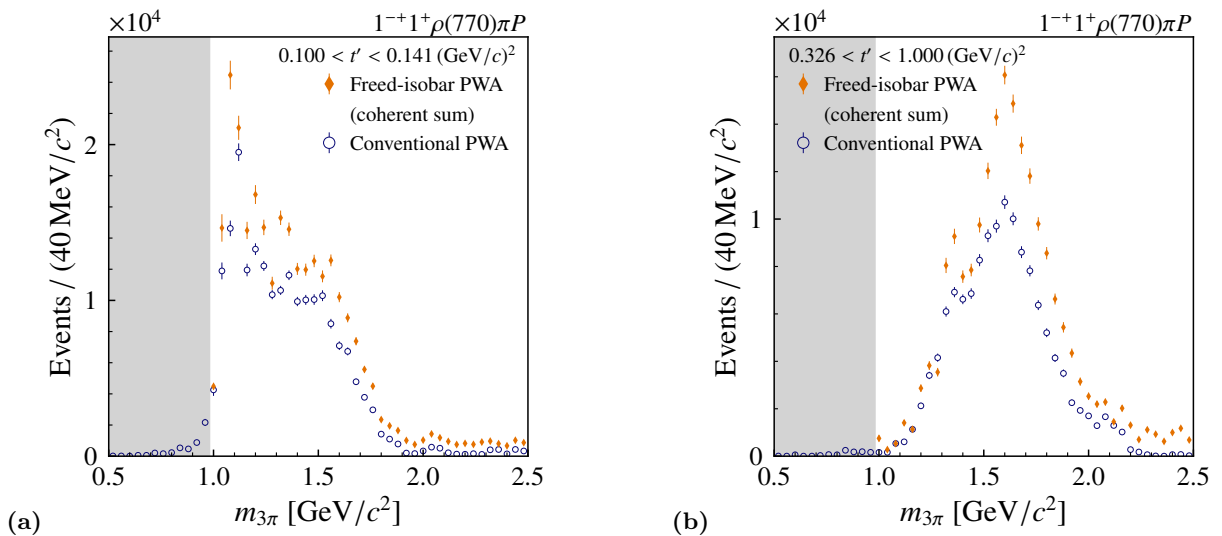
FIG. 8: Comparison of the $m_{3\pi}$ intensity distributions of the $1^{-+}1^+[\pi\pi]_{1^{--}}\pi P$ wave from the freed-isobar PWA (orange data points) and of the $1^{-+}1^+\rho(770)\pi P$ wave from the conventional PWA (blue data points). For the former, the intensities are calculated by coherently summing the contributions from all $m_{\pi^-\pi^+}$ intervals. (a) shows the lowest and (b) the highest t' bin. The shaded $m_{3\pi}$ range is excluded from the freed-isobar PWA.

Another way to compare the two PWA methods is to use the information that we obtain by fitting the $m_{\pi^-\pi^+}$ dependence of the amplitudes extracted by the freed-isobar PWA with Eq. (13) using the same fixed $\rho(770)$ parameters as in Ref. [47] (gray curves in Fig. 6). The interesting information is contained in the complex-valued quantity

$$\mathfrak{T}_a(m_{3\pi},t') \equiv \mathcal{C}_a(m_{3\pi},t')\,\mathcal{N}_a(m_{3\pi}) \tag{14}$$

that we determine for every $(m_{3\pi},t')$ cell and that is directly comparable to the transition amplitude $\mathcal{T}_a(m_{3\pi},t')$ obtained in the fixed-isobar PWA.[r] In Fig. 9(a), we compare the intensity distribution $|\mathfrak{T}_a(m_{3\pi})|^2$ from the freed-isobar PWA (red data points) to the intensity distribution from the fixed-isobar PWA (blue data points) for the 1^{-+} wave in the highest t' bin. The red data points in Fig. 9(a) are very similar to the orange ones in Fig. 8(b). This confirms that the 1^{-+} wave is well described a dynamic isobar amplitude containing only the $\rho(770)$.

As explained in Sec. V, the amplitudes $\{\mathcal{T}_{a,k}\}$ determined by the freed-isobar PWA contain information on both the 3π system and the $\pi^-\pi^+$ subsystem [see Eqs. (7) and (9)]. In order to consistently extract the $m_{3\pi}$ dependence of the phase of a freed wave, we thus need to model the $m_{\pi^-\pi^+}$ dependence of the freed-isobar transition amplitude. This is accomplished by the introduction of the amplitude $\mathfrak{T}_a(m_{3\pi},t')$ via Eqs. (13) and (14), which defines the phase of the 1^{-+} wave that can be compared to the phase obtained in the fixed-isobar PWA. We use the fixed-isobar $4^{++}1^+\rho(770)\pi G$ wave as reference wave since it exhibits a nonzero intensity distribution over a broad $m_{3\pi}$ range and a clear signal of the $a_4(2040)$.[s] From the fits of Eq. (13) with fixed $\rho(770)$ parameters we obtain Fig. 9(b). In this figure, we compare the phase of the 1^{-+} wave with respect to the $4^{++}1^+\rho(770)\pi G$ wave obtained from the freed-isobar PWA in

---

[r]Note that $\mathcal{N}_a$ contains a normalization factor we choose such that $|\mathfrak{T}_a|^2$ gives the number of events per interval in $m_{3\pi}$ and t'.

[s]Usually, the largest waves in the PWA model are used as reference waves. However, in the freed-isobar PWA model these waves use freed dynamic isobar amplitudes (see Tables 2 and 4) and therefore do not offer a consistent reference phase.
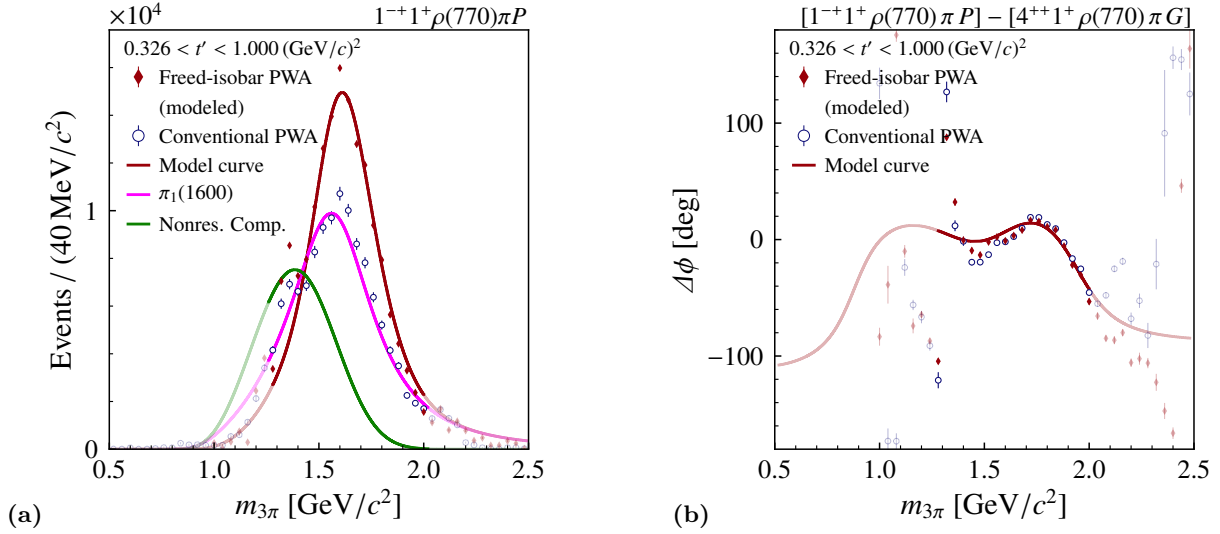
FIG. 9: (a) intensity distribution and (b) phase of the spin-exotic wave with respect to the $4^{++}1^+\rho(770)\pi G$ wave in the highest t' bin. The red data points represent the $1^{-+}1^+[\pi\pi]_{1^{--}}\pi P$ amplitude from the freed-isobar PWA after modelling the $m_{\pi^-\pi^+}$ dependence using the $\rho(770)$ Breit-Wigner amplitude in Eq. (13); the blue data points represent the $1^{-+}1^+\rho(770)\pi P$ amplitude from the conventional fixed-isobar PWA. The red curve represents the result of a fit of a resonance model to the red data points, which is the coherent sum of a resonant amplitude for the $\pi_1(1600)$ (magenta curve) and a nonresonant term (green curve).

the way described above (red data points) with the corresponding phase from the fixed-isobar PWA (blue data points). The two phase motions are in qualitative agreement in the $m_{3\pi}$ range from about 1.4 to $2.0\,\text{GeV}/c^2$. For $m_{3\pi} \lesssim 1.2\,\text{GeV}/c^2$, the phase is not well determined because the intensities of the two waves are small. The rapid phase motion at $1.2\,\text{GeV}/c^2$ is caused by the nearly vanishing intensity of the 4^{++} wave. The rising phase motion in the range from 1.4 to $1.7\,\text{GeV}/c^2$ indicates the presence of the $\pi_1(1600)$ in the 1^{-+} wave, whereas the falling phase motion from 1.7 to $2.0\,\text{GeV}/c^2$ is caused by the $a_4(2040)$ in the 4^{++} wave. Similar rising phase motions are also observed with respect to other waves, e.g., with respect to the $4^{-+}0^+\rho(770)\pi F$ and $6^{-+}0^+\rho(770)\pi H$ waves discussed in Sec. VI.

To further check the consistency between the conventional and the freed-isobar PWA, we fit the $m_{3\pi}$ dependence of the amplitude $\mathfrak{T}_a$ defined in Eqs. (13) and (14) simultaneously for all four t' bins using the same Breit-Wigner model as in Ref. [46]. However, we cannot perform the same 14-wave fit as given in Tab. II of Ref. [46] because most of the selected 14 waves are in the set of 12 freed waves (see Tables 2 and 4) and hence do not provide well-defined phases. Here, we perform a much simpler fit that only includes the 1^{-+} intensity distribution, i.e., $|\mathfrak{T}_a(m_{3\pi})|^2$, and the phase of $\mathfrak{T}_a(m_{3\pi})$ with respect to the amplitude of the fixed-isobar $4^{++}1^+\rho(770)\pi G$ wave. The $4^{++}1^+\rho(770)\pi G$ wave was included in the 14-wave resonance-model fit in Ref. [46], which was another reason to choose it as the reference wave. The $m_{3\pi}$ fit range is restricted to the overlap region from 1.26 to $2.02\,\text{GeV}/c^2$ of the fit ranges of the 1^{-+} and the 4^{++} waves in the resonance-model fit in Ref. [46]. We take the parametrizations for the 1^{-+} and the 4^{++} partial-wave amplitudes from Ref. [46] and use them to model the real and imaginary part of $\mathfrak{T}_a(m_{3\pi})$. In the fit, we let the parameters of the $\pi_1(1600)$ and the nonresonant component in the 1^{-+} wave float. We describe the phase of the 4^{++} wave without any free parameters by using the fit result from Ref. [46]. Since the phase of the 4^{++} wave depends on the t' bin, we have to translate the eleven t' bins used in Ref. [46] to the four bins used here. Thus, for our four

t' bins we construct a linear combination of the phases in the eleven t' bins, using the overlap of the corresponding t' bins weighted with the t' distribution of all events as coefficients. This is possible, since the phase of the 4^{++} wave changes smoothly with t'. In an alternate approach, we replace these linear combinations of the phases in t' bins by a single phase taken from the closest of the eleven t' bins yielding a very similar result. The found $\pi_1(1600)$ resonance parameters are

$$m_{\pi_1(1600)} = 1550 \, \text{MeV}/c^2 \quad \text{and} \quad \Gamma_{\pi_1(1600)} = 500 \, \text{MeV}/c^2. \tag{15}$$

These values are compatible with those found in Ref. [46] and are based on the same data. We do not give any uncertainties in Eq. (15), since we did not perform systematic studies and the statistical uncertainties are negligible compared to the systematic ones. The latter are expected to be in the same order of magnitude as those quoted in Ref. [46]. Increasing the lower $m_{3\pi}$ limit of the fit range to $1.34 \, \text{GeV}/c^2$, for example, yields a $\pi_1(1600)$ that is $30 \, \text{MeV}/c^2$ heavier and $180 \, \text{MeV}/c^2$ narrower.

D   Summary: dynamic isobar amplitude in the $J^{PC} = 1^{-+}$ wave

In conclusion, the results for the spin-exotic $J^{PC} = 1^{-+}$ wave from the freed-isobar PWA confirm the findings from the conventional PWA with fixed parametrizations of the dynamic isobar amplitudes presented in Refs. [46, 47] in several important aspects: (i) The emergence of the $\rho(770)$ resonance in the $\pi^-\pi^+$ subsystem of the 1^{-+} wave, as shown in Figs. 5 and 6, confirms that the assumption of the 1^{-+} wave decaying via a $\rho(770)$ isobar is indeed valid. (ii) The observed agreement of the extracted dynamic isobar amplitude of the $J^{PC} = 1^{--}$ $\pi^-\pi^+$ subsystem with the $\rho(770)$ amplitude used in the conventional PWA validates the chosen $\rho(770)$ parametrization and the parameter values within about $10\,\%$. (iii) We observe good agreement between the results from the freed-isobar PWA with those from the fixed-isobar PWA in terms of the phase motions and the shape of the intensity distributions as function of $m_{3\pi}$, as shown in Figs. 8 and 9. Thus the structures observed in the 1^{-+} amplitude in the conventional PWA are not an artifact due to the employed parametrizations for the dynamic isobar amplitudes. This is supported by the similarity of the $\pi_1(1600)$ resonance parameters from the freed-isobar PWA with those from the 14-wave resonance-model fit from Ref. [46].

VI   The Deck process and its projection into the $J^{PC} = 1^{-+}$ wave

Most partial-wave amplitudes contained in the 88-wave set used to analyze the COMPASS proton-target data (see Secs. III and IV A) contain coherent contributions from resonant and nonresonant processes. Aiming at extracting the resonant components through fits of resonance models to the $m_{3\pi}$ and t' dependence of the spin-density matrix, COMPASS has used a simple empirical description for the amplitude of the nonresonant processes (see Sec. IV A 2 in Ref. [53]). Our resonance-model fits reveal contributions of nonresonant processes that are very different for the various partial waves. The intensity of the nonresonant contributions shows a strong dependence on t' that is often more pronounced than that of the resonances. In the analyzed $m_{3\pi}$ and t' range, the nonresonant components are expected to originate predominantly from double-Regge exchange processes, of which the so-called Deck effect is the most prominent one. In Fig. 10, we show the diagram of the Deck process for the $\pi^-\pi^-\pi^+$ final state. In this process, a quasi on-shell pion is exchanged between the vertices a and b becoming real by scattering off the target proton via Pomeron or Reggeon exchange. The $\pi^-\pi^+$ state produced at vertex a, originally taken to be the $\rho(770)$, is the only appearing resonance. The described process was proposed by R. T. Deck in Ref. [48] as an alternative explanation to $a_1(1260)$ resonance production in the $\rho(770)\,\pi$ S-wave channel [68, 69].
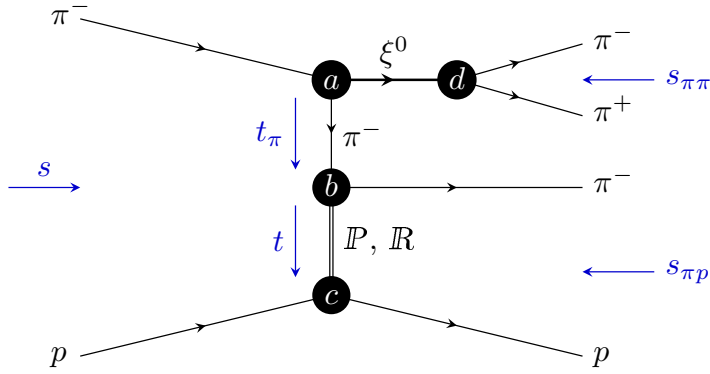
FIG. 10: Schematic diagram of the Deck process with the relevant kinematic variables.

In the COMPASS proton-target data, we found that the shape of the intensity distribution of the spin-exotic $1^{-+}1^+\rho(770)\pi P$ wave changes strongly with t' [46], which is indicative of large nonresonant contributions that seem to contribute particularly at low t' as already discussed in Sec. IV. This is consistent with the result of our resonance-model fit, where we found that the 1^{-+} wave is strongly dominated by nonresonant amplitudes at low t'. In this paper, we investigate the role of the Deck process in this wave by determining the intensity distribution of the Deck model in the $1^{-+}1^+\rho(770)\pi P$ wave and by comparing it to the analytical description of the nonresonant component that we obtained in our resonance-model fit. We also study projections of the Deck amplitude into waves with higher spin for which no confirmed resonances exist [20] and compare with the corresponding intensity distributions obtained from real data. To perform these studies we use pseudo data generated according to a model of the Deck process using Monte Carlo techniques. Since the pseudo data contain only nonresonant contributions, the direct comparison with real data neglects the interference between the resonant and nonresonant wave components. However, similar intensity distributions in real and pseudo data would point to dominant contributions from nonresonant Deck-like processes in the real data.

For our first attempt to model the Deck process, we use the simplified model from Refs. [70–72] to construct the Deck amplitude that we use to generate the pseudo data. In the model, the Deck amplitude is factorized into three terms (cf. Fig. 10): (i) an amplitude $\mathcal{A}_{\pi\pi}$ that describes the $\pi^-\pi^+ \to \pi^-\pi^+$ scattering including the vertices a and d, (ii) a stable-particle propagator that describes the pion exchange, and (iii) an amplitude $\mathcal{A}_{\pi p}$ that describes the $\pi^-p \to \pi^-p$ scattering including the vertices b and c. We hence write the Deck amplitude as:[t]

$$\mathcal{A}_{\text{Deck}}(s_{\pi\pi}, s_{\pi p}, t_\pi, t) = \mathcal{A}_{\pi\pi}(s_{\pi\pi}, t_\pi) \frac{e^{\frac{b}{2} t_\pi}}{m_\pi^2 - t_\pi} \mathcal{A}_{\pi p}(s_{\pi p}, t). \tag{16}$$

It is important to note that we Bose-symmetrize the amplitude in Eq. (16) with respect to the two indistinguishable π^-. The kinematic variables are defined in Fig. 10 with $s_{\pi\pi}$ being the squared center-of-momentum energy of the $\pi^-\pi^+$ system between vertices a and d, t_π the squared four-momentum transferred by the exchange pion, $s_{\pi p}$ the squared center-of-momentum energy of the π^-p system including the vertices b and c, and t the squared four-momentum transferred to the target. Note, that both t and t_π are negative. Like in the original Deck model in Ref. [48], we only take into account pion exchange between vertices a and b in Fig. 10, while possible additional processes like $\rho(770)$ meson exchange are neglected.

The $\pi^-\pi^+ \to \pi^-\pi^+$ amplitude in Eq. (16) is taken from Ref. [73], using the result of a so-called energy-dependent analysis based on data for the reaction $\pi^-p \to \pi^-\pi^+n$ measured at $17.2\,\text{GeV}/c$

---

[t]Since we do not use the Deck amplitude to calculate absolute cross sections, the normalization of Eq. (16) is irrelevant.

pion-beam momentum. This analysis yielded the $\pi\pi$ partial-wave amplitudes $\mathcal{T}_\ell^I$ for orbital angular momenta $\ell = 0, 1, 2, 3$ between the two pions. The model included amplitudes with isospin $I = 0$ of the $\pi\pi$ system for even ℓ and $I = 1$ for odd ℓ. In addition, an $I = 2$ amplitude was included for $\ell = 0$. The P-, D-, and F-wave amplitudes are dominated by $\rho(770)$, $f_2(1270)$, and $\rho_3(1690)$, respectively. The parametrization of the S-, P-, and D-wave amplitudes $\mathcal{T}_0^0$, $\mathcal{T}_1^1$, and $\mathcal{T}_2^0$ is based on K matrices that take into account the $\pi\pi$ and $K\overline{K}$ channels. The F-wave amplitude is parametrized by a dynamic-width Breit-Wigner amplitude for the $\rho_3(1690)$ (see Eq. (12d) in Ref. [73]). The S- and P-wave amplitudes use a K matrix containing two poles and a constant background term (see Eqs. (12a), (12b) and (13a) in Ref. [73]), where the $\rho(770)$ pole in the P-wave includes the angular-momentum barrier factor. The K matrix for the D-wave amplitude contains a single pole, which includes the angular-momentum barrier factor, and a constant background term (see Eqs. (12c) and (13b) in Ref. [73]). For the $I = 2$ S-wave amplitude, a scattering-length formula is used (see Eq. (14) in Ref. [73]). We use the parameters given in Tab. 1 of Ref. [73].

For the propagator of the exchanged pion, we use in Eq. (16) the non-reggeized form containing only the pion pole $1/(m_\pi^2 - t_\pi)$ and a form factor $e^{b\,t_\pi}$ (see Eq. (2.1) in Ref. [71]). We use a slope parameter of $b = 3.4\,(\mathrm{GeV}/c)^{-2}$, which provides a reasonable description of the angular distributions of the COMPASS data in the $m_{3\pi}$ range from 2.3 to 2.5 GeV/c^2 assuming that the Deck process dominates in this mass range.

For the $\pi^- p \to \pi^- p$ amplitude in Eq. (16) we employ the simple parametrization from Eq. (3.1) in Ref. [70]:

$$\mathcal{A}_{\pi p}(s_{\pi p}, t) = i\,s_{\pi p}\,e^{\frac{a}{2}t}, \tag{17}$$

with an exponential slope of $a = 8\,(\mathrm{GeV}/c)^{-2}$.

Figure 11 shows the $m_{3\pi}$ and $m_{\pi^-\pi^+}$ distributions of the 75×10^6 Deck Monte Carlo events The various $\pi^-\pi^+$ resonances that are included in the model are reflected in the spectrum. In order to roughly estimate the Deck-like contributions to the real-data intensity distributions, we perform a PWA of the Deck Monte Carlo data using the same 88-wave PWA model that was applied to the COMPASS proton-target data in Ref. [46] (see Table 4 in Appendix A). We show in Fig. 12 as an example the intensity distributions of the Deck model in the $4^{-+}0^+\rho(770)\pi F$ and 6^{-+} $0^+\rho(770)\pi H$ waves for low and high values of t' superimposed with the real-data distributions. Owing to the absence of confirmed resonances in these waves, we expect the measured intensities to be dominated by nonresonant contributions. This hypothesis is supported by the fact that the shapes of the Deck intensity distributions are in good qualitative agreement with the real data over the full t' range. Note that the Deck Monte Carlo data are normalized using only one common factor for all waves that is determined from the 1^{-+} wave as described further below.

In Fig. 13, we compare the intensity distributions of the $1^{-+}1^+\rho(770)\pi P$ wave for Deck pseudo data and real data, where the latter contains contributions from resonances as well as nonresonant processes. In addition, we show curves that correspond to the nonresonant component found in the resonance-model fit in Ref. [46]. We normalize the Deck intensity in the 1^{-+} wave to the nonresonant curves from the resonance-model fit by matching their $m_{3\pi}$-integrated intensities summed over the lowest 9 of the 11 t' bins. The two highest t' bins are excluded from the calculation of the normalization factor because in this region the $\pi_1(1600)$ resonance dominates the 1^{-+} wave and hence the nonresonant component has a large systematic uncertainty. The same normalization factor is also used for the other waves shown in Fig. 12. For the first 9 t' bins, i.e., for $t' \lesssim 0.5\,(\mathrm{GeV}/c)^2$, the shapes of the Deck intensity distributions are in qualitative agreement with the nonresonant curves from the resonance-model fit [see Figs. 13(a) to 13(c)]. This shows that the empirical parametrization used for the nonresonant component in the resonance-model
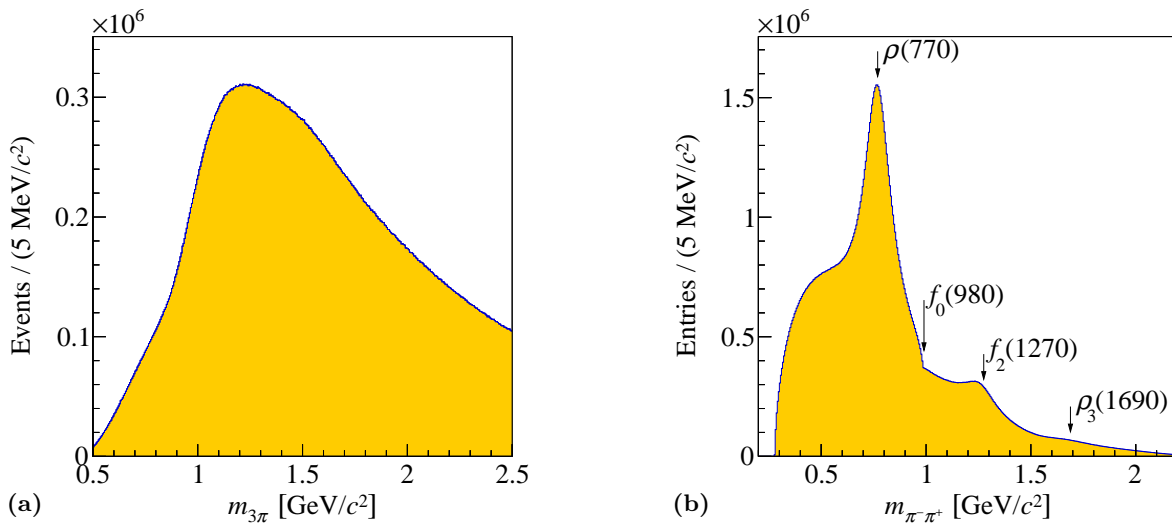
FIG. 11: (a) $\pi^-\pi^-\pi^+$ invariant mass spectrum for the Deck Monte Carlo sample. (b) invariant mass distribution of the $\pi^-\pi^+$ subsystem (2 entries per event). The arrows indicate 2π resonances included in the Deck model.

fit is able to capture the gross features of the Deck amplitudes. We find that the t' dependence of the Deck intensity is shallower than that of the nonresonant curve leading to an undershoot of the Deck intensity at low t' [see Fig. 13(a)] and an overshoot at high t' [see Fig. 13(c)]. For the two highest t' bins, i.e., for $t' \gtrsim 0.5\,(\text{GeV}/c)^2$, the shapes of the Deck intensity distribution and the nonresonant curve start to deviate [see Fig. 13(d)]. The observed behavior of the Deck model is consistent with our finding in Ref. [46] that at low t' the broad structure in the 1^{-+} intensity distribution is mostly due to nonresonant contributions masking the small $\pi_1(1600)$ signal.

A   Summary: the Deck process and the $J^{PC} = 1^{-+}$ wave

We have studied a simple model for the Deck process [see Eq. (16) and Fig. 10] and have compared its intensity distribution in selected waves with the ones obtained from real data. With only one common normalization factor, we find that the Deck intensity is in qualitative agreement with the measured intensity distributions of the $4^{-+}0^+\rho(770)\pi F$ and $6^{-+}0^+\rho(770)\pi H$ waves in the analyzed t' range. This is consistent with the expectation that these waves are dominated by nonresonant components because there are no confirmed π_4 or π_6 resonances [20].

We find that the Deck intensity distribution in the spin-exotic $1^{-+}1^+\rho(770)\pi P$ wave qualitatively reproduces the strong t' dependence of intensity and shape of the nonresonant component that we extracted in our resonance-model fit in Ref. [46] in the range $t' \lesssim 0.5\,(\text{GeV}/c)^2$. In this t' range, the intensity of the nonresonant contribution is similar to or larger than the intensity of the $\pi_1(1600)$ component. However, with regard to the t' dependence it must be recognized that the present simple version of the Deck model does not adequately describe the background yield in the high-t' range where the $\pi_1(1600)$ resonance dominates the $1-+$ wave (see Fig. 13).

Nuclear effects such as absorption seem to play an important role in the scattering process in the t' range between 0.1 and $1.0\,(\text{GeV}/c)^2$, so that the process cannot be described simply as incoherent scattering off quasi-free nucleons. There are currently no models available that describe Deck-like processes on nuclear targets. Such models could help to better understand the enhancement of the $\pi_1(1600)$ signal relative to the nonresonant component that we observe in the lead-target data as compared to the proton-target data (see Sec. IV).
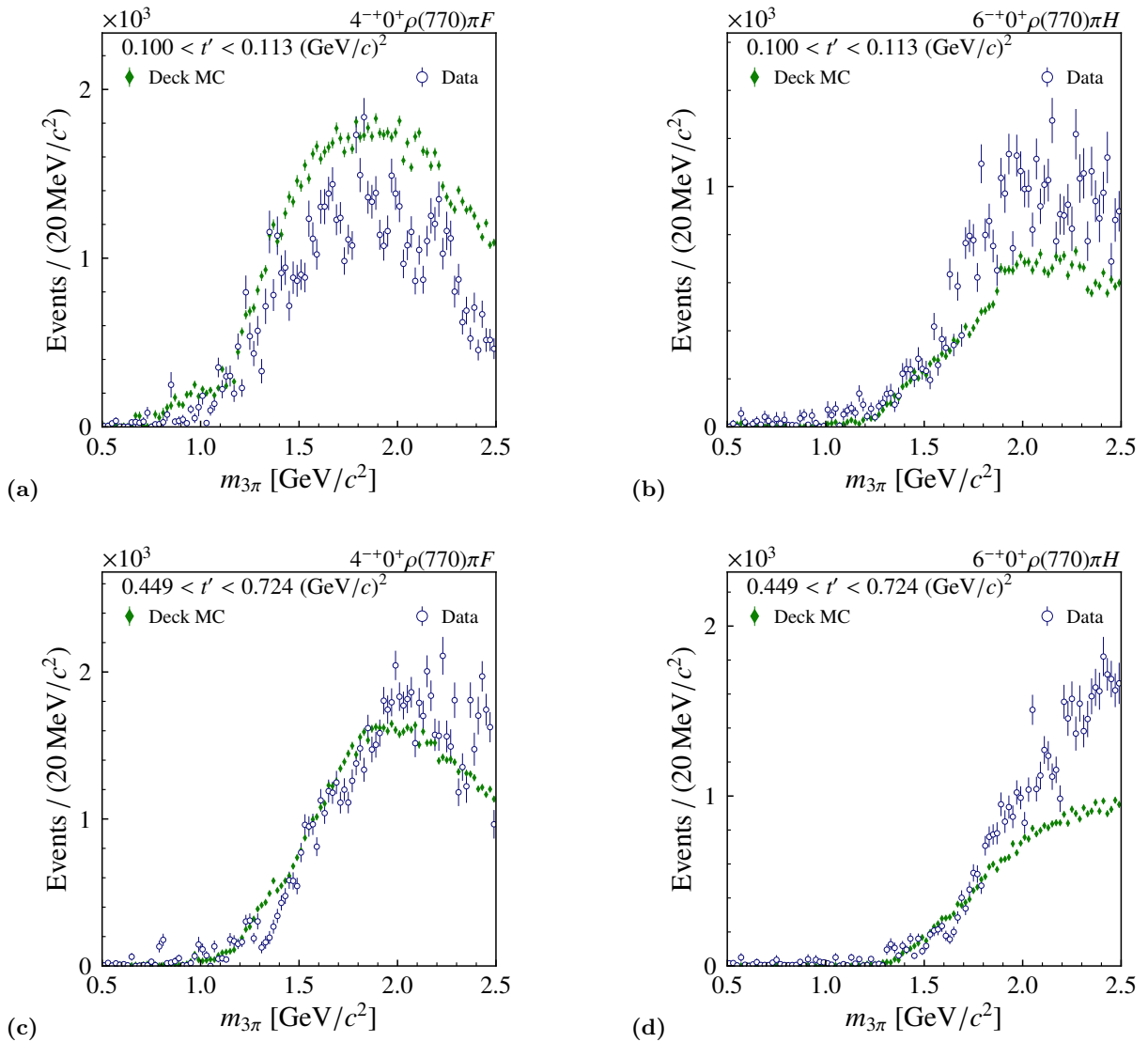
FIG. 12: Intensity distributions of the $4^{-+}0^{+}\rho(770)\pi F$ wave (left column) and the $6^{-+}0^{+}\rho(770)$ πH wave (right column) for two t' bins as obtained from the 88-wave PWA. The real data are represented by the blue data points; the Deck pseudo data by the green data points. The pseudo data are normalized using a common factor for all waves (see text for details).
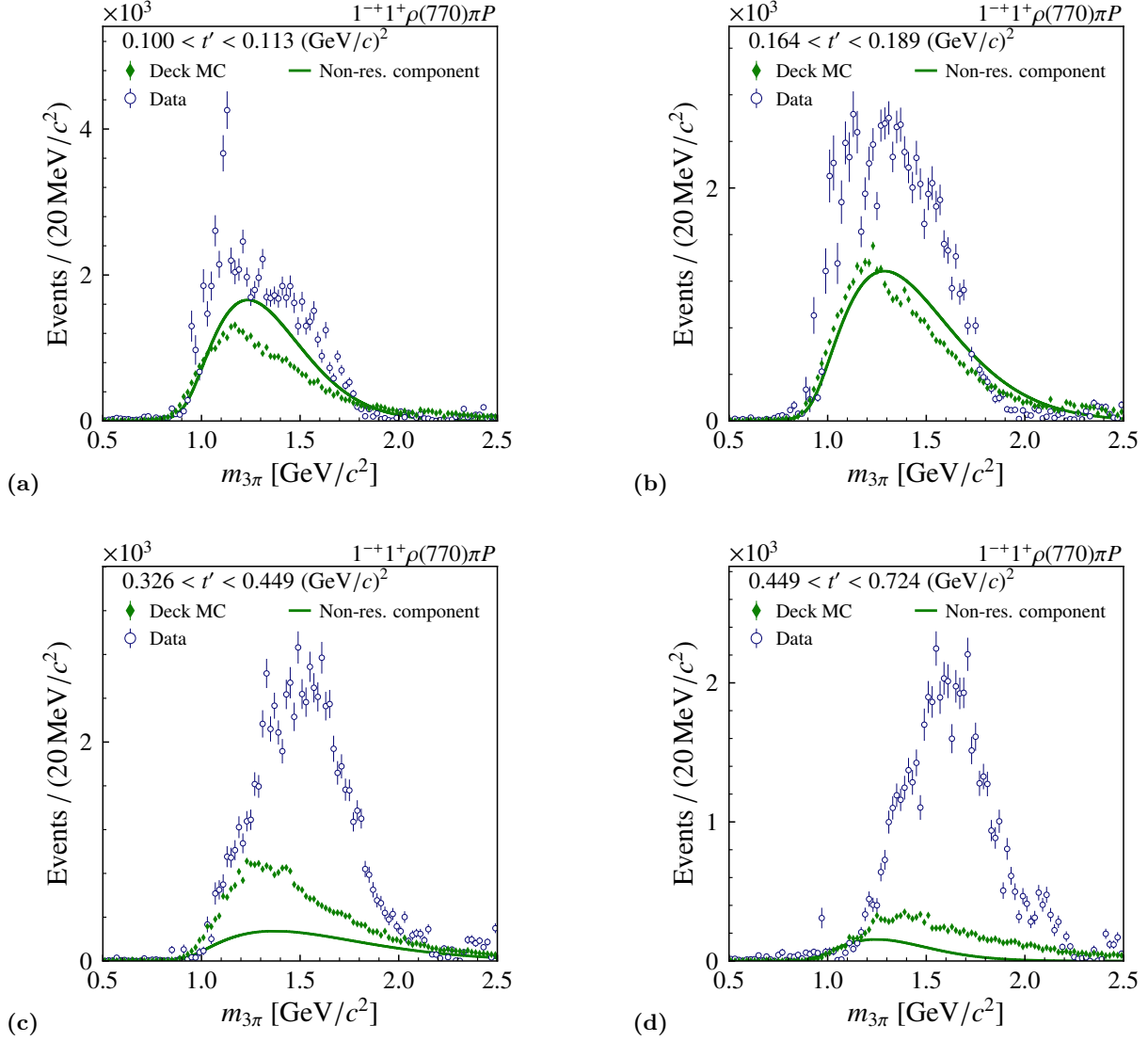
FIG. 13: Intensity distributions of the $1^{-+}1^{+}\rho(770)\pi P$ wave in different t' bins as obtained from the 88-wave PWA. The real data are represented by the blue data points; the Deck pseudo data by the green data points. The green curve represents the nonresonant component determined in the resonance-model fit in Ref. [46]. The pseudo data are normalized using a common factor for all waves (see text for details).

Appendix

A   Compilation of wave sets used in partial-wave analyses of the 3π system

Table 4 lists the wave sets used in the partial-wave analyses that are summarized in Table 1.

Table 4: Comparison of the 88-wave set used for the COMPASS proton-target data with the wave sets of BNL E852, VES, Dzierba *et al.*, and the one used for the COMPASS lead-target data. Entries that are not in the COMPASS 88-wave set are additionally highlighted in red. Entries highlighted in blue indicate waves that are replaced in the freed-isobar PWA by waves with dynamic isobar amplitudes parametrized according to Eq. (7) (see also Table 2).

$J^{PC}\,M^{\varepsilon}$	Isobar	L	COMPASS 88 waves Tab. IX in [47]	BNL E852 21 waves Tab. I in [42]	VES 44 waves [37]	Dzierba *et al.* 36 waves Tab. IV in [45]	COMPASS 42 waves [43]
$0^{-+}0^{+}$	$[\pi\pi]_S$	S	✓	✓	✓	✓	✓
$0^{-+}0^{+}$	$\rho(770)$	P	✓	✓	✓	✓	✓
$0^{-+}0^{+}$	$f_0(980)$	S	✓	✓	✓	✓	✓
$0^{-+}0^{+}$	$f_2(1270)$	D	✓		✓		
$0^{-+}0^{+}$	$f_0(1500)$	S	✓				
$1^{++}0^{+}$	$[\pi\pi]_S$	P	✓		✓	✓	✓
$1^{++}1^{+}$	$[\pi\pi]_S$	P	✓		✓		✓
$1^{++}0^{+}$	$\rho(770)$	S	✓	✓	✓	✓	✓
$1^{++}1^{+}$	$\rho(770)$	S	✓	✓	✓	✓	✓
$1^{++}0^{+}$	$\rho(770)$	D	✓	✓	✓		✓
$1^{++}1^{+}$	$\rho(770)$	D	✓		✓		✓
$1^{++}0^{+}$	$f_0(980)$	P	✓		✓	✓	
$1^{++}1^{+}$	$f_0(980)$	P	✓				
$1^{++}0^{+}$	$f_2(1270)$	P	✓		✓		✓
$1^{++}1^{+}$	$f_2(1270)$	P	✓		✓	✓	✓
$1^{++}0^{+}$	$f_2(1270)$	F	✓				
$1^{++}0^{+}$	$\rho_3(1690)$	D	✓				
$1^{++}0^{+}$	$\rho_3(1690)$	G	✓				
$1^{-+}1^{+}$	$\rho(770)$	P	✓	✓	✓	✓	✓
$2^{++}1^{+}$	$\rho(770)$	D	✓	✓	✓	✓	✓
$2^{++}2^{+}$	$\rho(770)$	D	✓				
$2^{++}1^{+}$	$f_2(1270)$	P	✓		✓		✓
$2^{++}2^{+}$	$f_2(1270)$	P	✓				
$2^{++}1^{+}$	$\rho_3(1690)$	D	✓				
$2^{-+}0^{+}$	$[\pi\pi]_S$	D	✓	✓	✓	✓	✓
$2^{-+}1^{+}$	$[\pi\pi]_S$	D	✓		✓	✓	✓
$2^{-+}0^{+}$	$\rho(770)$	P	✓	✓	✓	✓	✓
$2^{-+}1^{+}$	$\rho(770)$	P	✓		✓	✓	✓
$2^{-+}2^{+}$	$\rho(770)$	P	✓				
$2^{-+}0^{+}$	$\rho(770)$	F	✓		✓	✓	✓
$2^{-+}1^{+}$	$\rho(770)$	F	✓		✓	✓	✓
$2^{-+}0^{+}$	$f_0(980)$	D	✓		✓	✓	
$2^{-+}1^{+}$	$f_0(980)$	D				✓	
$2^{-+}0^{+}$	$f_2(1270)$	S	✓	✓	✓	✓	✓
$2^{-+}1^{+}$	$f_2(1270)$	S	✓	✓	✓	✓	✓
$2^{-+}2^{+}$	$f_2(1270)$	S	✓				
$2^{-+}0^{+}$	$f_2(1270)$	D	✓	✓	✓	✓	✓
$2^{-+}1^{+}$	$f_2(1270)$	D	✓	✓	✓	✓	✓
$2^{-+}2^{+}$	$f_2(1270)$	D	✓				
$2^{-+}0^{+}$	$f_2(1270)$	G	✓				
$2^{-+}0^{+}$	$\rho_3(1690)$	P	✓			✓	
$2^{-+}1^{+}$	$\rho_3(1690)$	P	✓			✓	
$3^{++}0^{+}$	$[\pi\pi]_S$	F	✓				
$3^{++}1^{+}$	$[\pi\pi]_S$	F	✓				
$3^{++}0^{+}$	$\rho(770)$	D	✓		✓	✓	✓
$3^{++}1^{+}$	$\rho(770)$	D	✓				✓
$3^{++}0^{+}$	$\rho(770)$	G	✓				
$3^{++}1^{+}$	$\rho(770)$	G	✓				
$3^{++}0^{+}$	$f_2(1270)$	P	✓		✓	✓	✓

(Table continued)

Table 4: *(Continued)*

$J^{PC} M^\varepsilon$	Isobar	L	COMPASS 88 waves	BNL E852 21 waves	VES 44 waves	Dzierba *et al.* 36 waves	COMPASS 42 waves
$3^{++}1^+$	$f_2(1270)$	P	✓				✓
$3^{++}0^+$	$\rho_3(1690)$	S	✓	✓	✓	✓	✓
$3^{++}1^+$	$\rho_3(1690)$	S	✓		✓		✓
$3^{++}0^+$	$\rho_3(1690)$	I	✓				
$3^{-+}1^+$	$\rho(770)$	F	✓				
$3^{-+}1^+$	$f_2(1270)$	D	✓				
$4^{++}1^+$	$\rho(770)$	G	✓		✓	✓	✓
$4^{++}2^+$	$\rho(770)$	G	✓				
$4^{++}1^+$	$f_2(1270)$	F	✓		✓	✓	✓
$4^{++}2^+$	$f_2(1270)$	F	✓				
$4^{++}1^+$	$\rho_3(1690)$	D	✓			✓	
$4^{-+}0^+$	$[\pi\pi]_S$	G	✓				
$4^{-+}0^+$	$\rho(770)$	F	✓		✓	✓	✓
$4^{-+}1^+$	$\rho(770)$	F	✓				✓
$4^{-+}0^+$	$f_2(1270)$	D	✓		✓		
$4^{-+}1^+$	$f_2(1270)$	D	✓				
$4^{-+}0^+$	$f_2(1270)$	G	✓				
$4^{-+}0^+$	$\rho_3(1690)$	P			✓	✓	
$5^{++}0^+$	$[\pi\pi]_S$	H	✓				
$5^{++}1^+$	$[\pi\pi]_S$	H	✓				
$5^{++}0^+$	$\rho(770)$	G	✓				
$5^{++}0^+$	$f_2(1270)$	F	✓				
$5^{++}1^+$	$f_2(1270)$	F	✓				
$5^{++}0^+$	$f_2(1270)$	H	✓				
$5^{++}0^+$	$\rho_3(1690)$	D	✓				
$6^{++}1^+$	$\rho(770)$	I	✓				
$6^{++}1^+$	$f_2(1270)$	H	✓				
$6^{-+}0^+$	$[\pi\pi]_S$	I	✓				
$6^{-+}1^+$	$[\pi\pi]_S$	I	✓				
$6^{-+}0^+$	$\rho(770)$	H	✓				
$6^{-+}1^+$	$\rho(770)$	H	✓				
$6^{-+}0^+$	$f_2(1270)$	G	✓				
$6^{-+}0^+$	$\rho_3(1690)$	F	✓				
$1^{++}1^-$	$\rho(770)$	S	✓	✓	✓		✓
$1^{-+}0^-$	$\rho(770)$	P	✓	✓	✓	✓	✓
$1^{-+}1^-$	$\rho(770)$	P	✓	✓	✓	✓	✓
$2^{++}0^-$	$\rho(770)$	D	✓	✓	✓	✓	✓
$2^{++}1^-$	$\rho(770)$	D			✓		
$2^{++}0^-$	$f_2(1270)$	P	✓				✓
$2^{++}1^-$	$f_2(1270)$	P	✓				✓
$2^{-+}1^-$	$\rho(770)$	P			✓		
$2^{-+}1^-$	$f_2(1270)$	S	✓	✓	✓		✓
Flat			✓	✓	✓	✓	✓

B Ambiguity in the $J^{PC} = 1^{-+}$ amplitude in the freed-isobar partial-wave analysis

As has been already mentioned in Sec. V, continuous mathematical ambiguities of certain decay amplitudes, called zero modes, may appear in a freed-isobar PWA. Methods to detect and resolve zero modes are discussed in detail in Refs. [49, 66]. Because of zero modes, different values of the transition amplitudes $\{\mathcal{T}_{a,k}\}$ defined in Eqs. (7) and (9) may lead to the same total amplitude $\sum_k \mathcal{T}_{a,k}\, \Psi_{a,k}$ in Eq. (11), where k labels the $m_{\pi^-\pi^+}$ intervals. Zero modes may appear in sets of freed waves that have the same $J^{PC} M^\varepsilon$ quantum numbers but describe decays via different isobars. In special cases, such as the one described below, zero modes may also appear within a single freed wave due to Bose symmetrization of final-state particles.

In the following, we focus on the zero mode present within the $1^{-+}1^+[\pi\pi]_{1^{--}}\pi P$ wave. For the employed wave set (see Tables 2 and 4), it is mathematically well defined and it is the only zero mode affecting this wave. First, we show the origin of this zero-mode ambiguity in the 1^{-+} wave. To this end, we express the angular amplitude $\mathcal{K}_a(\tau)$ with $a = 1^{-+}1^+[\pi\pi]_{1^{--}}\pi P$ in Eq. (10) in the helicity formalism:[u][v]

$$\mathcal{K}_a(\tau) \propto \sum_{\lambda=\pm 1} -\frac{\lambda}{\sqrt{2}} \, {}^{(\varepsilon=+1)}D^{1*}_{1,\lambda}(\phi_{\mathrm{GJ}}, \vartheta_{\mathrm{GJ}}, 0) \, D^{1*}_{\lambda,0}(\phi_{\mathrm{HF}}, \vartheta_{\mathrm{HF}}, 0). \tag{B1}$$

Here, λ is the helicity of the 1^{--} isobar. The factor $-\lambda/\sqrt{2}$ is the Clebsch-Gordan coefficient $(L\,0\;J_\xi\,\lambda\,|\,J\,\lambda)$ that describes the coupling of the relative orbital angular momentum $L = 1$ between the isobar and the bachelor π^- with the spin $J_\xi = 1$ of the isobar to the spin $J = 1$ of X. The angular distributions of the decays $X^- \to \xi^0 + \pi^-$ and $\xi^0 \to \pi^- + \pi^+$ are described by Wigner D-functions, where the one for the X^- decay is defined in the reflectivity basis according to Eq. (19) in Ref. [47]. The subscripts GJ and HF of the angles denote the Gottfried-Jackson and helicity rest frames of X and the isobar, respectively (see Sec. III A in Ref. [47] for the definition of the coordinate systems). Inserting the D-functions

$$^{(\varepsilon=+1)}D^1_{1,\lambda}(\phi_{\mathrm{GJ}}, \vartheta_{\mathrm{GJ}}, 0) = \frac{1}{\sqrt{2}}\left(\cos\phi_{\mathrm{GJ}} - i\lambda\,\sin\phi_{\mathrm{GJ}}\,\cos\vartheta_{\mathrm{GJ}}\right) \tag{B2}$$

and

$$D^1_{\lambda,0}(\phi_{\mathrm{HF}}, \vartheta_{\mathrm{HF}}, 0) = -\frac{\lambda}{\sqrt{2}}\,e^{-i\lambda\,\phi_{\mathrm{HF}}}\,\sin\vartheta_{\mathrm{HF}} \tag{B3}$$

with $\lambda = \pm 1$ into Eq. (B1), we find

$$\mathcal{K}_a(\tau) \propto \left(\cos\phi_{\mathrm{GJ}}\,\cos\phi_{\mathrm{HF}} - \cos\vartheta_{\mathrm{GJ}}\,\sin\phi_{\mathrm{GJ}}\,\sin\phi_{\mathrm{HF}}\right)\sin\vartheta_{\mathrm{HF}}. \tag{B4}$$

The $\pi_1^-\pi_2^-\pi_3^+$ system contains two indistinguishable π^- and hence Eq. (B4) needs to be Bose-symmetrized. We choose the isobar to decay into $\pi_1^-\pi_3^+$ and the vector $\vec{p}_1^{\,\mathrm{HF}}$ to represent the momentum of π_1^- in the helicity rest frame of this isobar. We calculate the magnitude of this vector using the two-body breakup-momentum

$$q^2(m, m_1, m_2) = \frac{\left[m^2 - (m_1 + m_2)^2\right]\left[m^2 - (m_1 - m_2)^2\right]}{4m^2}. \tag{B5}$$

Thus $|\vec{p}_1^{\,\mathrm{HF}}| = q_{13}$, where

$$q_{ij} \equiv q(m_{ij}, m_\pi, m_\pi) \tag{B6}$$

is the breakup momentum between pions i and j with m_{ij} being the invariant mass of the two-pion system. Using the above equations, we express the x and y components of $\vec{p}_1^{\,\mathrm{HF}}$ using the helicity angles as spherical coordinates:

$$q_{13}\cos\phi_{\mathrm{HF}}\sin\vartheta_{\mathrm{HF}} = p_{1,x}^{\mathrm{HF}} = \frac{\cos\hat{\vartheta}_{\mathrm{GJ}}}{\sin\vartheta_{\mathrm{GJ}}}\,Q_{23} - \frac{\cos\vartheta_{\mathrm{GJ}}}{\sin\vartheta_{\mathrm{GJ}}}\,\frac{\vec{p}_{13}\cdot\vec{p}_{23}}{Q_{13}}, \tag{B7}$$

$$q_{13}\sin\phi_{\mathrm{HF}}\sin\vartheta_{\mathrm{HF}} = p_{1,y}^{\mathrm{HF}} = Q_{23}\sin\hat{\vartheta}_{\mathrm{GJ}}\sin(\phi_{\mathrm{GJ}} - \hat{\phi}_{\mathrm{GJ}}). \tag{B8}$$

---

[u]Also cf. with Eqs. (11) and (7) in Ref. [47].

[v]To ease the notation, we omit the wave index a in this section.

Here, angles with a hat ("ˆ") indicate the Bose-symmetrized system, where the isobar decays into $\pi_2^- \pi_3^+$. The $\vec{p}_{ij}$ represent the sums of the momenta of particles i and j in the 3π center-of-momentum system and the Q_{ij} are the two-body breakup momenta of the 3π system given by

$$Q_{ij} \equiv q(m_{3\pi}, m_{ij}, m_\pi). \tag{B9}$$

The right-hand sides of Eqs. (B7) and (B8) are obtained from transforming the four-momentum vector of π_1^+ from the Gottfried-Jackson frame into the helicity frame of the isobar. This calculation can be found in the supplemental material in Appendix E.

The angular amplitude $\mathcal{K}_a(\tau)$ in Eq. (B4) depends on the helicity angles with the coordinate system in the helicity rest frame depending on the particles forming the isobar. Equations (B7) and (B8) allow us to replace the dependencies of $\mathcal{K}_a(\tau)$ on the helicity angles by expressions depending only on Gottfried-Jackson angles for the two combinations of the final-state particles that correspond to Bose symmetrization. The coordinate system in the Gottfried-Jackson rest frame does not depend on the particles forming the isobar.[w] Expressing in addition the scalar product $\vec{p}_{13} \cdot \vec{p}_{23}$ in Eq. (B7) in terms of the Gottfried-Jackson angles, we obtain

$$\mathcal{K}_a(\tau_{13}) \propto \frac{Q_{23}}{q_{13}} \left(\cos\phi_{\mathrm{GJ}} \sin\vartheta_{\mathrm{GJ}} \cos\hat{\vartheta}_{\mathrm{GJ}} - \cos\hat{\phi}_{\mathrm{GJ}} \sin\hat{\vartheta}_{\mathrm{GJ}} \cos\vartheta_{\mathrm{GJ}} \right), \tag{B10}$$

where τ_{13} is the set of phase-space variables for the isobar decaying into $\pi_1^- \pi_3^+$. Performing the Bose symmetrization and including the dynamic isobar amplitude $\Delta(m_{ij})$, we find for the decay amplitude

$$\Psi_a(\tau_{13}, \tau_{23}) = \mathcal{K}_a(\tau_{13}) \, \Delta(m_{13}) + \mathcal{K}_a(\tau_{23}) \, \Delta(m_{23}). \tag{B11}$$

This amplitude exactly vanishes at every point in phase space if the dynamic amplitude $\Delta(m_{ij})$ has the form

$$\tilde{\Delta}(m_{ij}) = Q_{ij} \, q_{ij}. \tag{B12}$$

This is because the two terms in the bracket in Eq. (B10) are Bose-symmetrized versions of each other and thus

$$\mathcal{K}_a(\tau_{13}) = -\frac{Q_{23}}{q_{13}} \frac{q_{23}}{Q_{13}} \mathcal{K}_a(\tau_{23}). \tag{B13}$$

Consequently, changing the dynamic isobar amplitude according to

$$\Delta(m_{ij}) \to \Delta(m_{ij}) + \mathfrak{C} \, \tilde{\Delta}(m_{ij}) \tag{B14}$$

with an arbitrary complex-valued coefficient $\mathfrak{C}$ does not alter the decay amplitude and hence also leaves the intensity as well as the likelihood function unchanged. Therefore, the coefficient $\mathfrak{C}$ represents a mathematical ambiguity, or zero mode, in the PWA model that is defined by the real-valued zero-mode shape $\tilde{\Delta}(m_{ij})$. In the conventional PWA, this ambiguity does not appear owing to the fixed parametrization of the dynamic isobar amplitudes. However, in a freed-isobar PWA a shift in the direction of the zero mode is possible due to the freedom in the dynamic isobar amplitudes.

Let $\{\mathcal{T}_k^{\mathrm{fit}}\}$ be the set of binned transition amplitudes as defined in Eqs. (7) and (9) that are extracted in a freed-isobar PWA, with k being the index of the $m_{\pi^-\pi^+}$ interval. The $\{\mathcal{T}_k^{\mathrm{fit}}\}$ might

---

[w]Therefore, $(\vartheta_{\mathrm{GJ}}, \phi_{\mathrm{GJ}})$ and $(\hat{\vartheta}_{\mathrm{GJ}}, \hat{\phi}_{\mathrm{GJ}})$ in Eq. (B10) are two different sets of angles defined in the same coordinate system.

be shifted away from their physical values $\{\mathcal{T}_k^{\text{phys}}\}$ in the direction of the zero mode $\tilde{\Delta}(m_{ij})$ according to Eq. (B14). Thus for each $m_{\pi^-\pi^+}$ interval, the center of which is represented by m_k, we have[x]

$$\mathcal{T}_k^{\text{fit}} = \mathcal{T}_k^{\text{phys}} + \mathfrak{C}\,\tilde{\Delta}_k \quad \text{with} \quad \tilde{\Delta}_k \equiv \tilde{\Delta}(m_k). \tag{B15}$$

Since the ambiguity represented by $\mathfrak{C}$ in Eq. (B15) leaves the intensity and therefore the likelihood function unchanged, it can only be resolved by imposing prior knowledge about the dynamic isobar amplitudes.[y] For the 1^{-+} wave, we can safely assume the $\{\mathcal{T}_k^{\text{phys}}\}$ to contain the $\rho(770)$ resonance. We resolve the zero-mode ambiguity by determining that value of $\mathfrak{C}$ that minimizes the deviation of $\{\mathcal{T}_k^{\text{fit}}\}$ from the $\rho(770)$ Breit-Wigner amplitude. The deviation is measured by the residuals

$$\delta_k(\mathfrak{C}) \equiv \mathcal{T}_k^{\text{fit}} - \mathfrak{C}\,\tilde{\Delta}_k - \hat{\mathcal{T}}_a(m_k; m_{3\pi}, t'), \tag{B16}$$

where $\hat{\mathcal{T}}_a(m_k; m_{3\pi}, t')$ is the Breit-Wigner amplitude for the $\rho(770)$ resonance as given by Eq. (13). To determine $\mathfrak{C}$ and thereby resolve the zero-mode ambiguity, we minimize the Mahalanobis distance[z]

$$\chi^2(\mathfrak{C}) = \sum_{k,l} \delta_k(\mathfrak{C})\,\mathbf{V}_{kl}^{-1}\,\delta_l(\mathfrak{C}), \tag{B17}$$

where $\mathbf{V}$ is the covariance matrix of the $\{\mathcal{T}_k^{\text{fit}}\}$ (see Appendix C). Since we cannot exclude contributions from excited ρ states at higher $m_{\pi^-\pi^+}$, we limit the sum in Eq. (B17) to those $m_{\pi^-\pi^+}$ intervals k and l where $m_{\pi^-\pi^+} < 1.12\,\text{GeV}/c^2$.[aa]

Imposing the $\rho(770)$ Breit-Wigner amplitude in Eq. (B16) by minimizing the χ^2 function in Eq. (B17), we determine only one complex-valued degree of freedom, i.e., $\mathfrak{C}$, from the data. The real-valued zero-mode shape $\tilde{\Delta}(m_{ij})$ that enters Eq. (B17) is fixed and given by Eq. (B12). It is important to note that this procedure does not lead to a circular argument, i.e., we do not get out what we put in. This is because our procedure that resolves the zero-mode ambiguity cannot artificially generate a fake $\rho(770)$ resonance signal in the $\pi^-\pi^+$ isobar amplitude, i.e., a circular structure in the Argand diagram, if the $\rho(770)$ is not contained in the data. This has been verified through Monte-Carlo studies [49, 66]. In other words, we do not demand that the dynamic isobar amplitude is described entirely by the $\rho(770)$ as in conventional PWA method. Instead, we only impose the $\rho(770)$ to be a part of the amplitude. We hence fix a single complex value, i.e., $\mathfrak{C}$, using minimal assumptions on the shape of the dynamic isobar amplitude. This still leaves $2(n-1)$ complex-valued degrees of freedom, where n is the number of $m_{\pi^-\pi^+}$ intervals, that are determined from the data. The freed-isobar PWA thus yields much more information on the dynamic isobar amplitude in the $1^{-+}1^+[\pi\pi]_{1^{--}}\pi P$ wave than the conventional PWA method, which only returns a single complex-valued parameter, i.e., the transition amplitude, for this wave.

In Fig. 14, we show the result of the freed-isobar PWA (green data points) and the corresponding zero-mode corrected amplitude (blue data points) for an exemplary $(m_{3\pi}, t')$ cell. The green points are shifted away from their physical value by the zero mode with an accidental value for the coefficient $\mathfrak{C}$, which is different in every $(m_{3\pi}, t')$ cell. The gray histogram represents

---

[x]Since the shape of the zero mode is multiplied with an arbitrary coefficient, we normalize it to $\sum_k \tilde{\Delta}_k^2 = 1$.

[y]This is conceptually similar to gauge fixing in gauge symmetries.

[z]Since the δ_k are complex-valued, while the covariance matrix describes real-valued quantities, the sum over the $m_{\pi^-\pi^+}$ interval indices k and l runs implicitly also over the real and imaginary parts of the corresponding amplitudes (see also Sec. IV B in Ref. [46]).

[aa]The covariance matrix is first cut to this $m_{\pi^-\pi^+}$ range and then inverted.
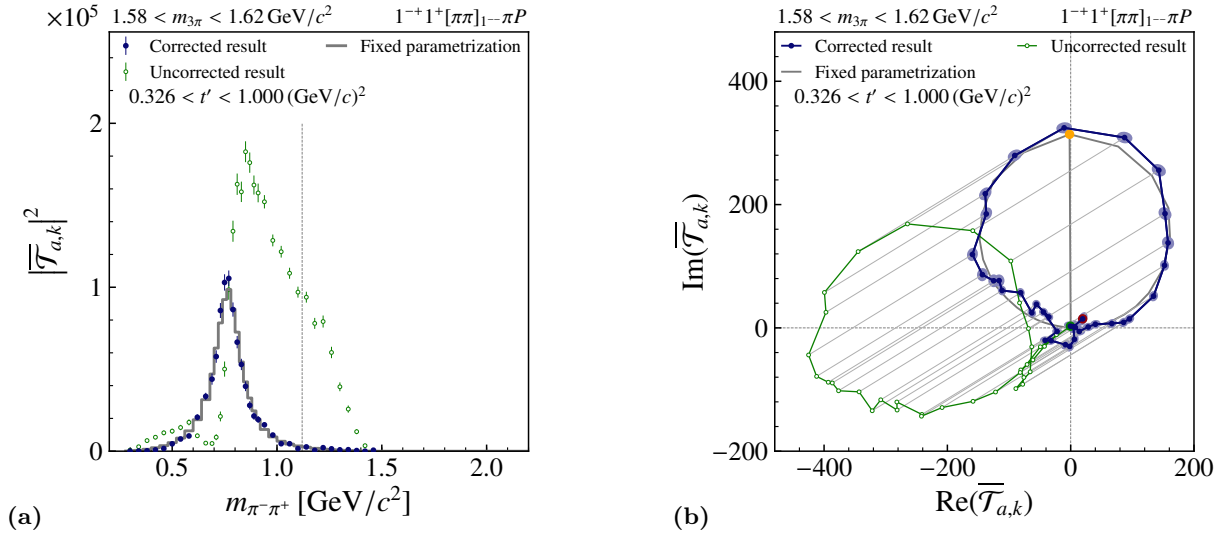
FIG. 14: Similar to Fig. 6 but showing the effect of resolving the zero-mode ambiguity in the $1^{-+}1^{+}[\pi\pi]_{1^{--}}\pi P$ wave using, as an example, the highest t' bin and an $m_{3\pi}$ bin in the $\pi_1(1600)$ resonance region. (a) shows the intensity distribution and (b) the corresponding Argand diagram as a function of $m_{\pi^-\pi^+}$. The green data points correspond to the set $\{\mathcal{T}_k^{\text{fit}}\}$ of binned transition amplitudes [defined in Eqs. (7) and (9)] as extracted in the freed-isobar PWA. The blue data points represent the transition amplitudes $\{\mathcal{T}_k^{\text{fit}} - \mathfrak{C}\,\tilde{\Delta}_k\}$ after resolving the zero-mode ambiguity by minimizing Eq. (B17). The upper limit $m_{\pi^-\pi^+} = 1.12\,\text{GeV}/c^2$ of the range used in this minimization is indicated by the vertical line in (a). The gray histogram represents the $\rho(770)$ Breit-Wigner amplitude used to resolve the zero-mode ambiguity. In the Argand diagram, corresponding green and blue data points are connected by gray lines representing the $\{\mathfrak{C}\,\tilde{\Delta}_k\}$ values.

the $\rho(770)$ Breit-Wigner amplitude $\hat{\mathcal{T}}_a(m_k; m_{3\pi}, t')$ used in Eqs. (B16) and (B17) to resolve the zero-mode ambiguity. Since the zero-mode shape given in Eq. (B12) is real valued, all green points in the Argand diagram are shifted in parallel directions to the blue points. It should be noted that only data for $m_{\pi^-\pi^+} < 1.12\,\text{GeV}/c^2$ were used to resolve the ambiguity. The resulting zero-mode corrected amplitude agrees well with the $\rho(770)$ Breit-Wigner also in the mass region $m_{\pi^-\pi^+} > 1.12\,\text{GeV}/c^2$. This method to resolve the ambiguity is used to produce Figs. 5 and 6. Note that the zero mode does not influence the $m_{3\pi}$ intensity distributions obtained by summing the contributions of the freed-isobar transition amplitudes $\{\mathcal{T}_{a,k}\}$ from all $m_{\pi^-\pi^+}$ intervals coherently (see Fig. 8).

We have studied several constraints to resolve the zero-mode ambiguity. In a first study, we extend the fit range to the full kinematically allowed $m_{\pi^-\pi^+}$ range. In a second study, we allow the $\rho(770)$ resonance parameters to float in the fit that resolves the ambiguity. In this approach, we either use a single set of $\rho(770)$ resonance parameters while simultaneously fitting all $(m_{3\pi}, t')$ cells or we allow for different $\rho(770)$ resonance parameters in each $(m_{3\pi}, t')$ cell. The resulting $\rho(770)$ resonance parameters obtained using the above approaches are discussed in Sec. V B. All these approaches yield similar results for the zero-mode corrected amplitudes (see also discussion in Sec. V).

In a third study, we try to resolve the zero mode by minimizing the variation of the zero-mode corrected amplitudes between neighboring $m_{3\pi}$ bins. This means we do not make any assumption on the $m_{\pi^-\pi^+}$ dependence of the amplitudes and just require a smooth behavior as a function of $m_{3\pi}$. The resulting zero-mode corrected amplitudes still exhibit a clear $\rho(770)$ resonance

signal but the method induces a considerable bias towards small intensities of the dynamic isobar amplitudes across all $m_{3\pi}$ and $m_{\pi^-\pi^+}$ bins. Because of this observed bias, we do do not use this approach.

C Preparation of the covariance matrix

In the freed-isobar PWA, the zero-mode coefficient $\mathfrak{C}$ in Eq. (B15) is a nuisance parameter that contains no physical information and is not constrained by the data (see Appendix B). But since $\mathfrak{C}$ mixes with all other fit parameters, it influences the uncertainties of these parameters. We thus want to remove the corresponding uncertainties from the covariance matrix $\mathbf{V}$ of the extracted transition amplitudes $\{\mathcal{T}_k^{\mathrm{fit}}\}$ that we obtain from the minimizing algorithm. Since the zero-mode $\tilde{\Delta}(m_{ij})$ in Eq. (B12) is real-valued, the ambiguity does not mix real and imaginary parts of the transition amplitudes. We therefore remove the uncertainty that corresponds to the zero-mode individually from the covariance matrices $\mathbf{V}_{\mathrm{Re}}$ and $\mathbf{V}_{\mathrm{Im}}$ of real and imaginary parts of the transition amplitudes. Those entries of the covariance that mix real and imaginary parts of the $\{\mathcal{T}_k^{\mathrm{fit}}\}$ are unaffected by the zero mode. To this end, we define a projection operator $\mathbf{P}$ that acts on the covariance matrix according to

$$\mathbf{V}_{\mathrm{Re,\,Im}} \to \mathbf{P} \cdot \mathbf{V}_{\mathrm{Re,\,Im}} \cdot \mathbf{P}. \tag{C1}$$

This projection operator is an $n \times n$ real-valued matrix, where n is the number of $m_{\pi^-\pi^+}$ intervals. It is defined as

$$\mathbf{P}_{kl} \equiv \delta_{kl} - \tilde{\Delta}_k\,\tilde{\Delta}_l, \tag{C2}$$

so that

$$\mathbf{P} \cdot \vec{\tilde{\Delta}} = \vec{0}, \quad \mathbf{P} \cdot \vec{\tilde{\Delta}}_\perp = \vec{\tilde{\Delta}}_\perp, \quad \text{and} \quad \mathbf{P} \cdot \mathbf{P} = \mathbf{P}. \tag{C3}$$

Here, $\vec{\tilde{\Delta}}_\perp$ is an arbitrary direction in the space of the $\{\mathcal{T}_k^{\mathrm{fit}}\}$ that is orthogonal to the zero mode $\vec{\tilde{\Delta}}$.[ab]

By construction, the covariance matrices $\mathbf{V}_{\mathrm{Re,\,Im}}$ in Eq. (C1), from which we removed the uncertainties corresponding to the zero mode, have eigenvectors in the direction of the zero mode with an eigenvalue of zero. However, using these matrices in Eq. (B17) would render the χ^2 function completely independent of the zero-mode coefficient $\mathfrak{C}$ so that we would not be able to determine $\mathfrak{C}$ by minimizing this function. We hence reinsert the zero mode as an eigenvector weighted with an arbitrary positive coefficient $\mathfrak{L}$, i.e., we perform the transformation

$$\mathbf{V}_{\mathrm{Re,\,Im}} \to \mathbf{P} \cdot \mathbf{V}_{\mathrm{Re,\,Im}} \cdot \mathbf{P} + \mathfrak{L}\,\vec{\tilde{\Delta}} \otimes \vec{\tilde{\Delta}}. \tag{C4}$$

Doing so, we ensure that the zero mode $\vec{\tilde{\Delta}}$ is an eigenvector of the covariance matrix $\mathbf{V}$ and therefore the determination of $\mathfrak{C}$ is independent from the determination of all other fit parameters in Eq. (B17). For this reason, the solutions for the zero-mode coefficient $\mathfrak{C}$ and the other fit parameters in Eq. (B16) are also independent of the particular choice for the value of $\mathfrak{L}$. We verified numerically that this holds over seventeen orders of magnitude for the value of $\mathfrak{L}$.

D Acknowledgements

[ab] $\vec{\tilde{\Delta}}$ is the vector that has the $\{\tilde{\Delta}_k\}$ as components.

References

[1] M. Tanimoto, "Decay patterns of $q\bar{q}g$ hybrid mesons," *Phys. Lett. B* **116** (1982) 198.

[2] N. Isgur, R. Kokoski, and J. E. Paton, "Gluonic excitations of mesons: Why they are missing and where to find them," *Phys. Rev. Lett.* **54** (1985) 869.

[3] F. Iddir, A. Le Yaouanc, L. Oliver, O. Pene, and J. C. Raynal, "Selection Rule for 1^{-+} Hybrid Decay Into $\eta\pi$ From QCD," *Phys. Lett. B* **207** (1988) 325.

[4] F. E. Close and P. R. Page, "The production and decay of hybrid mesons by flux-tube breaking," *Nucl. Phys.* **B443** (1995) 233–254, arXiv:hep-ph/9411301 [hep-ph].

[5] P. R. Page, E. S. Swanson, and A. P. Szczepaniak, "Hybrid meson decay phenomenology," *Phys. Rev. D* **59** (1999) 034016, arXiv:hep-ph/9808346 [hep-ph].

[6] J. J. Dudek, R. G. Edwards, M. J. Peardon, D. G. Richards, and C. E. Thomas, [Hadron Spectrum Collaboration], "Highly Excited and Exotic Meson Spectrum from Dynamical Lattice QCD," *Phys. Rev. Lett.* **103** (2009) 262001, arXiv:0909.0200 [hep-ph].

[7] J. J. Dudek, R. G. Edwards, M. J. Peardon, D. G. Richards, and C. E. Thomas, [Hadron Spectrum Collaboration], "Toward the excited meson spectrum of dynamical QCD," *Phys. Rev. D* **82** (2010) 034508, arXiv:1004.4930 [hep-ph].

[8] J. J. Dudek, "The lightest hybrid meson supermultiplet in QCD," *Phys. Rev. D* **84** (2011) 074023, arXiv:1106.5515 [hep-ph].

[9] J. J. Dudek, R. G. Edwards, P. Guo, and C. E. Thomas, [Hadron Spectrum Collaboration], "Toward the excited isoscalar meson spectrum from lattice QCD," *Phys. Rev. D* **88** (2013) 094505, arXiv:1309.2608 [hep-lat].

[10] A. J. Woss, J. J. Dudek, R. G. Edwards, C. E. Thomas, and D. J. Wilson, [Hadron Spectrum Collaboration], "Decays of an exotic 1^{-+} hybrid meson resonance in QCD," *Phys. Rev. D* **103** no. 5, (2021) 054502, arXiv:2009.10034 [hep-lat].

[11] R. A. Briceño, J. J. Dudek, and R. D. Young, "Scattering processes and resonances from lattice QCD," *Rev. Mod. Phys.* **90** (2018) 025001, arXiv:1706.06223 [hep-lat].

[12] M. T. Hansen and S. R. Sharpe, "Lattice QCD and Three-Particle Decays of Resonances," *Ann. Rev. Nucl. Part. Sci.* **69** (2019) 65–107, arXiv:1901.00483 [hep-lat].

[13] M. Ablikim *et al.*, [BESIII Collaboration], "Observation of a Charged Charmoniumlike Structure in $e^+e^- \to \pi^+\pi^- J/\psi$ at $\sqrt{s} = 4.26$ GeV," *Phys. Rev. Lett.* **110** (2013) 252001, arXiv:1303.5949 [hep-ex].

[14] Z. Q. Liu *et al.*, [Belle Collaboration], "Study of $e^+e^- \to \pi^+\pi^- J/\psi$ and Observation of a Charged Charmoniumlike State at Belle," *Phys. Rev. Lett.* **110** (2013) 252002, arXiv:1304.0121 [hep-ex].

[15] A. Bondar *et al.*, [Belle Collaboration], "Observation of Two Charged Bottomoniumlike Resonances in $\Upsilon(5S)$ Decays," *Phys. Rev. Lett.* **108** (2012) 122001, arXiv:1110.2251 [hep-ex].

[16] R. Aaij *et al.*, [LHCb Collaboration], "Observation of $J/\psi p$ Resonances Consistent with Pentaquark States in $\Lambda_b^0 \to J/\psi K^- p$ Decays," *Phys. Rev. Lett.* **115** (2015) 072001, arXiv:1507.03414 [hep-ex].

[17] R. Aaij *et al.*, [LHCb Collaboration], "Observation of a Narrow Pentaquark State, $P_c(4312)^+$, and of the Two-Peak Structure of the $P_c(4450)^+$," *Phys. Rev. Lett.* **122** (2019) 222001, `arXiv:1904.03947 [hep-ex]`.

[18] R. F. Lebed, R. E. Mitchell, and E. S. Swanson, "Heavy-Quark QCD Exotica," *Prog. Part. Nucl. Phys.* **93** (2017) 143–194, `arXiv:1610.04528 [hep-ph]`.

[19] S. L. Olsen, T. Skwarnicki, and D. Zieminska, "Nonstandard heavy mesons and baryons: Experimental evidence," *Rev. Mod. Phys.* **90** (2018) 015003, `arXiv:1708.04012 [hep-ph]`.

[20] M. Tanabashi *et al.*, [Particle Data Group], "Review of Particle Physics," *Phys. Rev. D* **98** (2018) 030001.

[21] D. Alde *et al.*, "Evidence for a 1^{-+} Exotic Meson," *Phys. Lett. B* **205** (1988) 397.

[22] H. Aoyagi *et al.*, "Study of the $\eta\pi^-$ system in the $\pi^- p$ reaction at 6.3 GeV/c," *Phys. Lett. B* **314** (1993) 246–254.

[23] D. R. Thompson *et al.*, [E852 Collaboration], "Evidence for Exotic Meson Production in the Reaction $\pi^- p \to \eta\pi^- p$ at 18 GeV/c," *Phys. Rev. Lett.* **79** (1997) 1630–1633, `arXiv:hep-ex/9705011 [hep-ex]`.

[24] S. U. Chung *et al.*, [E852 Collaboration], "Evidence for exotic $J^{PC} = 1^{-+}$ meson production in the reaction $\pi^- p \to \eta\pi^- p$ at 18 GeV/c," *Phys. Rev. D* **60** (1999) 092001, `arXiv:hep-ex/9902003 [hep-ex]`.

[25] V. Dorofeev *et al.*, [VES Collaboration], "The $J^{PC} = 1^{-+}$ hunting season at VES," *AIP Conf. Proc.* **619** (2002) 143–154, `arXiv:hep-ex/0110075 [hep-ex]`.

[26] G. S. Adams *et al.*, [E862 Collaboration], "Confirmation of the 1^{-+} meson exotics in the $\eta\pi^0$ system," *Phys. Lett. B* **657** (2007) 27–31, `arXiv:hep-ex/0612062 [hep-ex]`.

[27] A. Abele *et al.*, [Crystal Barrel Collaboration], "Exotic $\eta\pi$ state in $\bar{p}d$ annihilation at rest into $\pi^-\pi^0\eta p_{\text{spectator}}$," *Phys. Lett. B* **423** (1998) 175–184.

[28] A. Abele *et al.*, [Crystal Barrel Collaboration], "Evidence for a $\pi\eta$-P-wave in $\bar{p}p$-annihilations at rest into $\pi^0\pi^0\eta$," *Phys. Lett. B* **446** (1999) 349–355.

[29] M. Albrecht *et al.*, [Crystal Barrel Collaboration], "Coupled channel analysis of $\bar{p}p \to \pi^0\pi^0\eta$, $\pi^0\eta\eta$ and $K^+K^-\pi^0$ at 900 MeV/c and of $\pi\pi$-scattering data," *Eur. Phys. J. C* **80** (2020) 453, `arXiv:1909.07091 [hep-ex]`.

[30] P. Salvini *et al.*, [OBELIX Collaboration], "$\bar{p}p$ annihilation into four charged pions at rest and in flight," *Eur. Phys. J. C* **35** (2004) 21–33.

[31] J. Kuhn *et al.*, [E852 Collaboration], "Exotic meson production in the $f_1(1285)\pi^-$ system observed in the reaction $\pi^- p \to \eta\pi^+\pi^-\pi^- p$ at 18 GeV/c," *Phys. Lett. B* **595** (2004) 109–117, `arXiv:hep-ex/0401004 [hep-ex]`.

[32] M. Lu *et al.*, [E852 Collaboration], "Exotic Meson Decay to $\omega\pi^0\pi^-$," *Phys. Rev. Lett.* **94** (2005) 032002, `arXiv:hep-ex/0405044 [hep-ex]`.

[33] Y. A. Khokhlov, [VES Collaboration], "Study of $X(1600)$ 1^{-+} hybrid," *Nucl. Phys.* **A663** (2000) 596–599.

[34] E. I. Ivanov *et al.*, [E852 Collaboration], "Observation of exotic meson production in the reaction $\pi^- p \to \eta' \pi^- p$ at 18 GeV/c," *Phys. Rev. Lett.* **86** (2001) 3977–3980, `arXiv:hep-ex/0101058 [hep-ex]`.

[35] D. V. Amelin, Y. G. Gavrilov, Y. P. Gouz, V. A. Dorofeev, R. I. Dzhelyadin, *et al.*, [VES Collaboration], "Investigation of hybrid states in the VES experiment at the Institute for High Energy Physics (Protvino)," *Phys. Atom. Nucl.* **68** (2005) 359–371.

[36] G. S. Adams *et al.*, [CLEO Collaboration], "Amplitude analyses of the decays $\chi_{c1} \to \eta \pi^+ \pi^-$ and $\chi_{c1} \to \eta' \pi^+ \pi^-$," *Phys. Rev. D* **84** (2011) 112009, `arXiv:1109.5843 [hep-ex]`.

[37] A. Zaitsev, [VES Collaboration], "Study of exotic resonances in diffractive reactions," *Nucl. Phys.* **A675** (2000) 155–160.

[38] C. A. Baker, C. J. Batty, K. Braune, D. V. Bugg, N. Dzhaoshvili, *et al.*, "Confirmation of $a_0(1450)$ and $\pi_1(1600)$ in $\bar{p}p \to \omega \pi^+ \pi^- \pi^0$ at rest," *Phys. Lett. B* **563** (2003) 140–149.

[39] C. Adolph *et al.*, [COMPASS Collaboration], "Odd and even partial waves of $\eta \pi^-$ and $\eta' \pi^-$ in $\pi^- p \to \eta^{(\prime)} \pi^- p$ at 191 GeV/c," *Phys. Lett. B* **740** (2015) 303–311, `arXiv:1408.4286 [hep-ex]`.

[40] A. Rodas *et al.*, [JPAC Collaboration], "Determination of the Pole Position of the Lightest Hybrid Meson Candidate," *Phys. Rev. Lett.* **122** (2019) 042002, `arXiv:1810.04171 [hep-ph]`.

[41] G. S. Adams *et al.*, [E852 Collaboration], "Observation of a New $J^{PC} = 1^{-+}$ Exotic State in the Reaction $\pi^- p \to \pi^+ \pi^- \pi^- p$ at 18 GeV/c," *Phys. Rev. Lett.* **81** (1998) 5760–5763.

[42] S. U. Chung *et al.*, [E852 Collaboration], "Exotic and $q\bar{q}$ resonances in the $\pi^+ \pi^- \pi^-$ system produced in $\pi^- p$ collisions at 18 GeV/c," *Phys. Rev. D* **65** (2002) 072001.

[43] M. Alekseev *et al.*, [COMPASS Collaboration], "Observation of a $J^{PC} = 1^{-+}$ Exotic Resonance in Diffractive Dissociation of 190 GeV/c π^- into $\pi^- \pi^- \pi^+$," *Phys. Rev. Lett.* **104** (2010) 241803, `arXiv:0910.5842 [hep-ex]`.

[44] C. A. Meyer and E. S. Swanson, "Hybrid Mesons," *Prog. Part. Nucl. Phys.* **82** (2015) 21–58, `arXiv:1502.07276 [hep-ph]`.

[45] A. R. Dzierba, R. Mitchell, E. Scott, M. R. Shepherd, P. Smith, M. Swat, *et al.*, "Partial wave analysis of the $\pi^- \pi^- \pi^+$ and $\pi^- \pi^0 \pi^0$ systems and the search for a $J^{PC} = 1^{-+}$ meson," *Phys. Rev. D* **73** (2006) 072001, `arXiv:hep-ex/0510068 [hep-ex]`.

[46] M. Aghasyan *et al.*, [COMPASS Collaboration], "Light isovector resonances in $\pi^- p \to \pi^- \pi^- \pi^+ p$ at 190 GeV/c," *Phys. Rev. D* **98** (2018) 092003, `arXiv:1802.05913 [hep-ex]`.

[47] C. Adolph *et al.*, [COMPASS Collaboration], "Resonance production and $\pi\pi$ S-wave in $\pi^- + p \to \pi^- \pi^- \pi^+ + p_{\text{recoil}}$ at 190 GeV/c," *Phys. Rev. D* **95** (2017) 032004, `arXiv:1509.00992 [hep-ex]`.

[48] R. T. Deck, "Kinematical Interpretation of the First π-ρ Resonance," *Phys. Rev. Lett.* **13** (1964) 169–173.

[49] F. Krinner, D. Greenwald, D. Ryabchikov, B. Grube, and S. Paul, "Ambiguities in model-independent partial-wave analysis," *Phys. Rev. D* **97** (2018) 114008, `arXiv:1710.09849 [hep-ph]`.

[50] F. Haas, "Two-Dimensional Partial-Wave Analysis of Exclusive 190 GeV $\pi^- p$ Scattering into the $\pi^- \pi^- \pi^+$ Final State at COMPASS (CERN)," PhD thesis, Technische Universität München, 2014. `http://cds.cern.ch/record/1662589/`. CERN-THESIS-2013-277.

[51] P. Abbon *et al.*, [COMPASS Collaboration], "The COMPASS experiment at CERN," *Nucl. Instrum. Methods Phys. Res., Sect. A* **577** (2007) 455–518, `arXiv:hep-ex/0703049` `[hep-ex]`.

[52] P. Abbon *et al.*, [COMPASS Collaboration], "The COMPASS setup for physics with hadron beams," *Nucl. Instrum. Methods Phys. Res., Sect. A* **779** (2015) 69–115, `arXiv:1410.1797` `[physics.ins-det]`.

[53] M. Aghasyan *et al.*, [COMPASS Collaboration], "Light isovector resonances in $\pi^- p \to \pi^- \pi^- \pi^+ p$ at 190 GeV/c—Supplemental Material," *Phys. Rev. D* **98** (2018) 092003, `arXiv:1802.05913 [hep-ex]`. `https://journals.aps.org/prd/supplemental/10.1103/PhysRevD.98.092003`.

[54] S. U. Chung and T. L. Trueman, "Positivity conditions on the spin density matrix: A simple parametrization," *Phys. Rev. D* **11** (1975) 633.

[55] K. Gottfried and J. D. Jackson, "On the connection between production mechanism and decay of resonances at high energies," *Nuovo Cim.* **33** (1964) 309–330.

[56] G. Cohen-Tannoudji, P. Salin, and A. Morel, "A simple formulation of high-energy exchange models in terms of direct-channel amplitudes," *Nuovo Cim. A* **55** (1968) 412–422.

[57] V. Mathieu, M. Albaladejo, C. Fernández-Ramírez, A. W. Jackura, M. Mikhasenko, A. Pilloni, and A. P. Szczepaniak, [JPAC Collaboration], "Moments of angular distribution and beam asymmetries in $\eta\pi^0$ photoproduction at GlueX," *Phys. Rev. D* **100** (2019) 054017, `arXiv:1906.04841 [hep-ph]`.

[58] M. L. Perl, *High Energy Hadron Physics*. Wiley-Interscience Publication. Wiley, 1974.

[59] I. A. Kachaev. Institute for High Energy Physics, Protvino, private communication, 2020.

[60] N. A. Törnqvist, "Understanding the scalar meson $q\bar{q}$ nonet," *Z. Phys. C* **68** (1995) 647–660, `arXiv:hep-ph/9504372 [hep-ph]`.

[61] "Resonances" in M. Tanabashi *et al.*, [Particle Data Group], "Review of Particle Physics," *Phys. Rev. D* **98** (2018) 571–575. `http://pdg.lbl.gov/2018/reviews/rpp2018-rev-resonances.pdf`.

[62] M. Nozar *et al.*, [CLAS Collaboration], "Search for the Photoexcitation of Exotic Mesons in the $\pi^+ \pi^+ \pi^-$ System," *Phys. Rev. Lett.* **102** (2009) 102002, `arXiv:0805.4438 [hep-ex]`.

[63] P. Eugenio and C. Bookwalter, [CLAS Collaboration], "Search for exotic mesons in photoproduction at JLab CLAS," *AIP Conf. Proc.* **1560** (2013) 421–423.

[64] B. Ketzer, "Hybrid Mesons," *PoS* **QNP2012** (2012) 025, `arXiv:1208.5125 [hep-ex]`.

[65] S. Grabmüller, "Cryogenic Silicon Detectors and Analysis of Primakoff Contributions to the Reaction $\pi^- \mathrm{Pb} \to \pi^- \pi^- \pi^+ \mathrm{Pb}$ at COMPASS," PhD thesis, Technische Universität München, 2012. `https://cds.cern.ch/record/1492155/`. CERN-THESIS-2012-170.

[66] F. Krinner, "Freed-Isobar Partial-Wave Analysis," PhD thesis, Technische Universität München, 2018. `https://wwwcompass.cern.ch/compass/publications/theses/2018_phd_krinner.pdf`.

[67] K. L. Au, D. Morgan, and M. R. Pennington, "Meson dynamics beyond the quark model: Study of final-state interactions," *Phys. Rev. D* **35** (1987) 1633.

[68] G. Goldhaber, J. L. Brown, J. A. Kadyk, and B. C. Shen, "Evidence for a $\pi\rho$ Interaction Produced in the $\pi^+ p$ Reaction at 3.65 BeV," *Phys. Rev. Lett.* **12** (1964) 336.

[69] S. U. Chung, O. I. Dahl, L. M. Hardy, R. I. Hess, G. R. Kalbfleisch, *et al.*, "Analysis of the 1.0-1.4 BeV πp Enhancement," *Phys. Rev. Lett.* **12** (1964) 621.

[70] G. Ascoli, L. M. Jones, B. Weinstein, and H. W. Wyld, "Partial-Wave Analysis of the Deck Amplitude for $\pi N \to \pi\pi\pi N$," *Phys. Rev. D* **8** (1973) 3894–3919.

[71] G. Ascoli, R. Cutler, L. M. Jones, U. Kruse, T. Roberts, B. Weinstein, and H. W. Wyld, "Deck-model calculation of $\pi^- p \to \pi^-\pi^+\pi^- p$," *Phys. Rev. D* **9** (1974) 1963–1979.

[72] C. Daum *et al.*, [ACCMOR Collaboration], "Diffractive production of 3π states at 63 and 94 GeV," *Nucl. Phys.* **B182** (1981) 269.

[73] B. Hyams, C. Jones, P. Weilhammer, W. Blum, H. Dietl, *et al.*, "$\pi\pi$ Phase Shift Analysis from 600 to 1900 MeV," *Nucl. Phys.* **B64** (1973) 134–162.

Supplemental Material

In this supplemental material, we provide additional information.

In Appendix E, we give details on the calculation of the zero mode in the spin-exotic $1^{-+}1^+$ $[\pi\pi]_{1--}\pi P$ wave that is discussed in Appendix B. In Appendix F, we show the comparison between freed-isobar and conventional PWA similar to Figs. 8 and 9 for the t' bins that are not shown in the paper. Finally, in Appendix G, we show the $[\pi\pi]_{1--}$ dynamic isobar amplitude in the $1^{-+}1^+[\pi\pi]_{1--}\pi P$ wave as a function of $m_{\pi^-\pi^+}$ similar to Fig. 6 for all $(m_{3\pi}, t')$ cells the freed-isobar PWA was performed in.

E Ambiguity in the $J^{PC} = 1^{-+}$ amplitude in the freed-isobar partial-wave analysis

In order to derive Eqs. (B7) and (B8), we consider the decay of a particle X into three particles 1, 2, and 3. We want to express momentum vectors defined in the helicity rest frame (HF) of the (13) two-particle subsystem using variables defined in the Gottfried-Jackson rest frame (GJ) of the (123) system X.

In the Gottfried-Jackson frame,

$$\vec{p}_1 + \vec{p}_2 + \vec{p}_3 = \vec{0}, \tag{E1}$$

where $\vec{p}_i$ is the three-momentum of particle i. Since we want to transform from the Gottfried-Jackson into the (13) helicity frame, we consider the three-momentum vector

$$\vec{p}_{13} = \vec{p}_1 + \vec{p}_3 \tag{E2}$$

of the (13) subsystem in the Gottfried-Jackson frame. The z axis of the (13) helicity frame is given by the direction of $\vec{p}_{13}$, i.e.,

$$\hat{e}_z^{\mathrm{HF}} = \frac{\vec{p}_{13}}{p_{13}}, \tag{E3}$$

where $p_{13} \equiv |\vec{p}_{13}|$. The y axis is given by

$$\hat{e}_y^{\mathrm{HF}} = \frac{\hat{e}_z^{\mathrm{GJ}} \times \hat{e}_z^{\mathrm{HF}}}{\left|\hat{e}_z^{\mathrm{GJ}} \times \hat{e}_z^{\mathrm{HF}}\right|} \tag{E4}$$

and the x axis completes the right-handed orthonormal basis, i.e.,

$$\hat{e}_x^{\mathrm{HF}} = \hat{e}_y^{\mathrm{HF}} \times \hat{e}_z^{\mathrm{HF}}. \tag{E5}$$

While the normalization of the x and z unit vectors of the helicity frame is trivial, we find the normalization of the y unit vector to be

$$\left|\hat{e}_z^{\mathrm{GJ}} \times \hat{e}_z^{\mathrm{HF}}\right| = \sin\vartheta_{\mathrm{GJ}}. \tag{E6}$$

Here, ϑ_{GJ} is the polar angle of $\vec{p}_{13}$ in the Gottfried-Jackson frame; the corresponding azimuthal angle is ϕ_{GJ}.

Using Eqs. (E4) and (E6), we can rewrite Eq. (E5):

$$\hat{e}_x^{\mathrm{HF}} = \frac{1}{\sin\vartheta_{\mathrm{GJ}}} \left(\hat{e}_z^{\mathrm{GJ}} \times \hat{e}_z^{\mathrm{HF}}\right) \times \hat{e}_z^{\mathrm{HF}}$$
$$= \frac{1}{\sin\vartheta_{\mathrm{GJ}}} \left[\left(\hat{e}_z^{\mathrm{GJ}} \cdot \hat{e}_z^{\mathrm{HF}}\right) \hat{e}_z^{\mathrm{HF}} - \left(\hat{e}_z^{\mathrm{HF}} \cdot \hat{e}_z^{\mathrm{HF}}\right) \hat{e}_z^{\mathrm{GJ}}\right]$$

$$= \frac{\cos \vartheta_{\text{GJ}}}{\sin \vartheta_{\text{GJ}}} \, \hat{e}_z^{\text{HF}} - \frac{1}{\sin \vartheta_{\text{GJ}}} \, \hat{e}_z^{\text{GJ}}. \tag{E7}$$

Based on the expressions for the basis vectors of the helicity frame in the Gottfried-Jackson frame in Eqs. (E3), (E4), (E6), and (E7), we can write down the corresponding rotation matrix $\mathbf{R}$. The rows of this matrix are given by the helicity-frame basis vectors, i.e.,

$$\begin{aligned} \mathbf{R} &= \left(\hat{e}_x^{\text{HF}}, \hat{e}_y^{\text{HF}}, \hat{e}_z^{\text{HF}} \right)^{\mathsf{T}} \\ &= \left(\frac{\cos \vartheta_{\text{GJ}}}{\sin \vartheta_{\text{GJ}}} \frac{\vec{p}_{13}}{|\vec{p}_{13}|} - \frac{1}{\sin \vartheta_{\text{GJ}}} \hat{e}_z^{\text{GJ}}, \frac{\hat{e}_z^{\text{GJ}} \times \vec{p}_{13}}{\sin \vartheta_{\text{GJ}} |\vec{p}_{13}|}, \frac{\vec{p}_{13}}{|\vec{p}_{13}|} \right)^{\mathsf{T}}. \end{aligned} \tag{E8}$$

Applying this matrix to a momentum vector $\vec{p}$ defined in the Gottfried-Jackson frame yields a vector

$$\vec{p}^{\,\prime} = \mathbf{R} \cdot \vec{p} \tag{E9}$$

that is defined in a rotated reference frame that differs from the (13) helicity frame merely by a Lorentz boost along $\vec{p}_{13}$ direction into the rest frame of the (13) subsystem. Since the $\vec{p}_{13}$ direction corresponds to the z direction in the rotated frame, the boost does not affect the x and y components of $\vec{p}^{\,\prime}$ and hence the corresponding components of the vector $\vec{p}^{\,\text{HF}}$ defined in the helicity frame are given by

$$p_x^{\text{HF}} = p_x^{\prime} \quad \text{and} \quad p_y^{\text{HF}} = p_y^{\prime}. \tag{E10}$$

However, the boost mixes the z component $p_z^{\prime}$ and the energy E that corresponds to $\vec{p}$ and $\vec{p}^{\,\prime}$. Therefore,

$$p_z^{\text{HF}} = \left(\frac{E_{13}}{m_{13}} p_z^{\prime} - \frac{p_{13}}{m_{13}} E \right), \tag{E11}$$

where $\gamma = E_{13}/m_{13}$ and $\beta\gamma = p_{13}/m_{13}$ are the usual relativistic factors of the Lorentz boost. Here, E_{13} and p_{13} are energy and momentum of the (13) subsystem in the Gottfried-Jackson frame and m_{13} is the corresponding invariant mass. Using Eqs. (E8) to (E11), we can write all components of $\vec{p}^{\,\text{HF}}$:

$$p_x^{\text{HF}} = \frac{\cos \vartheta_{\text{GJ}}}{\sin \vartheta_{\text{GJ}}} \frac{\vec{p}_{13} \cdot \vec{p}}{p_{13}} - \frac{1}{\sin \vartheta_{\text{GJ}}} p_z \tag{E12}$$

$$p_y^{\text{HF}} = \frac{\left(\hat{e}_z^{\text{GJ}} \times \vec{p}_{13} \right) \cdot \vec{p}}{\sin \vartheta_{\text{GJ}} \, p_{13}} \tag{E13}$$

$$p_z^{\text{HF}} = \frac{E_{13}}{m_{13}} \frac{\vec{p}_{13} \cdot \vec{p}}{p_{13}} - \frac{p_{13}}{m_{13}} E. \tag{E14}$$

In order to derive Eqs. (B7) and (B8), we specifically need the expressions for $p_{1,x}^{\text{HF}}$ and $p_{1,y}^{\text{HF}}$. Due to Eq. (E1)

$$\vec{p}_1 = -\vec{p}_2 - \vec{p}_3 = -\vec{p}_{23} \tag{E15}$$

and in particular

$$p_{1,z} = -p_{23,z} = -p_{23} \cos \hat{\vartheta}_{\text{GJ}}, \tag{E16}$$

where p_{23} and $\hat{\vartheta}_{\mathrm{GJ}}$ are the magnitude and the polar angle of $\vec{p}_{23}$ in the Gottfried-Jackson frame; the corresponding azimuthal angle is $\hat{\phi}_{\mathrm{GJ}}$. Using the above relations and Eq. (E12), we find

$$p_{1,x}^{\mathrm{HF}} = \frac{\cos \hat{\vartheta}_{\mathrm{GJ}}}{\sin \vartheta_{\mathrm{GJ}}} p_{23} - \frac{\cos \vartheta_{\mathrm{GJ}}}{\sin \vartheta_{\mathrm{GJ}}} \frac{\vec{p}_{13} \cdot \vec{p}_{23}}{p_{13}}. \tag{E17}$$

We make use of the properties of the combination of dot and the cross products when calculating $p_{1,y}^{\mathrm{HF}}$ via Eq. (E13):

$$\left(\hat{e}_z^{\mathrm{GJ}} \times \vec{p}_{13} \right) \cdot \vec{p}_1 = - \left(\hat{e}_z^{\mathrm{GJ}} \times \vec{p}_{13} \right) \cdot \vec{p}_{23} \tag{E18}$$

$$= - \left(\vec{p}_{13} \times \vec{p}_{23} \right) \cdot \hat{e}_z^{\mathrm{GJ}} \tag{E19}$$

$$= \left(\vec{p}_{23} \times \vec{p}_{13} \right) \cdot \hat{e}_z^{\mathrm{GJ}}. \tag{E20}$$

We thus need the z component of $\vec{p}_{23} \times \vec{p}_{13}$, which is given by

$$(\vec{p}_{23} \times \vec{p}_{13})_z = p_{13} \, p_{23} \, \sin \vartheta_{\mathrm{GJ}} \, \sin \hat{\vartheta}_{\mathrm{GJ}} \left(\cos \phi_{\mathrm{GJ}} \sin \hat{\phi}_{\mathrm{GJ}} - \sin \phi_{\mathrm{GJ}} \cos \hat{\phi}_{\mathrm{GJ}} \right). \tag{E21}$$

This simplifies to

$$(\vec{p}_{23} \times \vec{p}_{13})_z = p_{13} \, p_{23} \, \sin \vartheta_{\mathrm{GJ}} \, \sin \hat{\vartheta}_{\mathrm{GJ}} \, \sin \left(\phi_{\mathrm{GJ}} - \hat{\phi}_{\mathrm{GJ}} \right), \tag{E22}$$

leading to

$$p_{1,y}^{\mathrm{HF}} = p_{23} \, \sin \hat{\vartheta}_{\mathrm{GJ}} \, \sin \left(\phi_{\mathrm{GJ}} - \hat{\phi}_{\mathrm{GJ}} \right). \tag{E23}$$

Since the momenta p_{13} and p_{23} are the breakup momenta Q_{13} and Q_{23} as defined in Eq. (B9), Eqs. (E17) and (E23) are identical to Eqs. (B7) and (B8).

F Comparison of the freed-isobar with the conventional partial-wave analysis

In Fig. 15, we show the comparison between the coherently summed result of the freed-isobar PWA for the second and third t' bin (similar to Fig. 8).
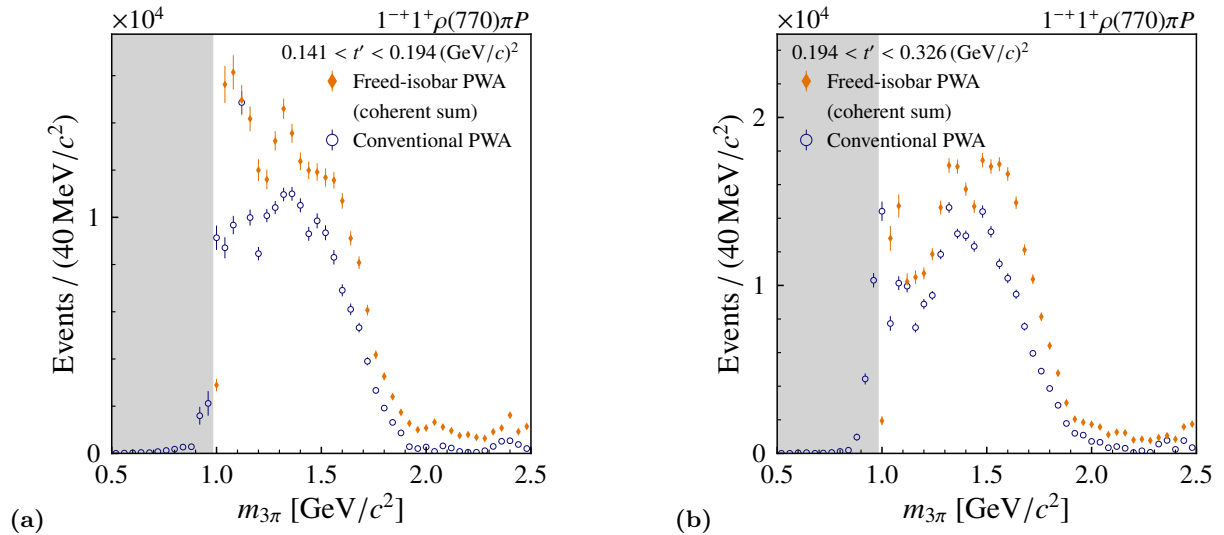
FIG. 15: Comparison of the $m_{3\pi}$ intensity distributions of the $1^{-+}1^+[\pi\pi]_{1^{--}}\pi P$ wave from the freed-isobar PWA (orange data points) and of the $1^{-+}1^+\rho(770)\pi P$ wave from the conventional PWA (blue data points), similar to Fig. 8.

In Fig. 16, we show the results of the Breit-Wigner resonance-model fit to the results of the freed-isobar PWA for the spin-exotic wave similar to Fig. 9 for the three lowest t' bins.
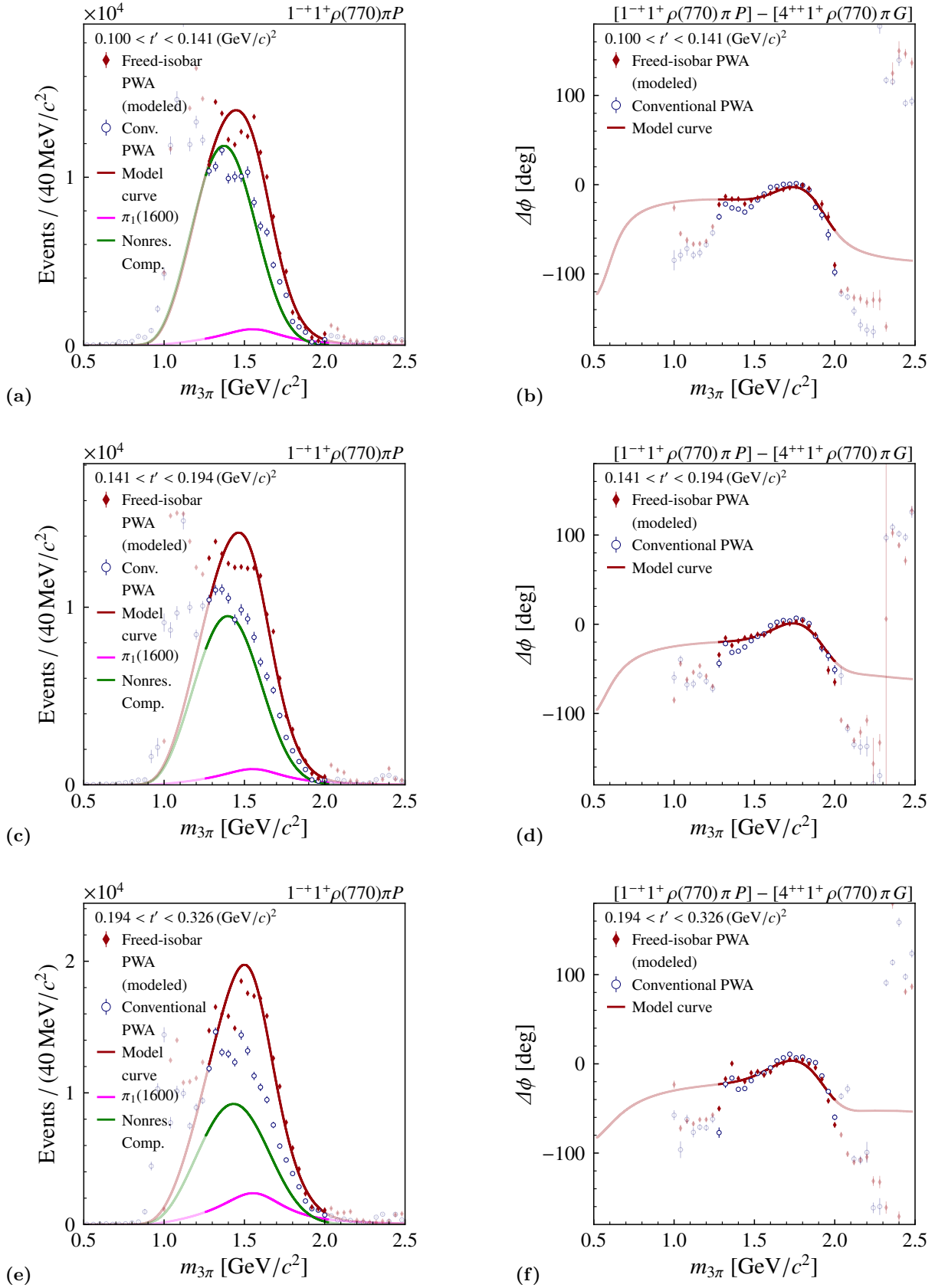
FIG. 16: Intensity distribution and phase of the spin-exotic wave with respect to the $4^{++}1^+$ $\rho(770)\pi G$ wave in the three lowest t' bins, similar to Fig. 9.

G   Dynamic isobar amplitudes from freed-isobar partial-wave analysis

In addition to the three $(m_{3\pi}, t')$ cells shown in Fig. 6, we show in Figures 17 to 68 the $[\pi\pi]_{1^{--}}$ dynamic isobar amplitude in the $1^{-+}1^{+}[\pi\pi]_{1^{--}}\pi P$ wave as a function of $m_{\pi^-\pi^+}$ for all 152 $(m_{3\pi}, t')$ cells with $m_{3\pi} > 0.98\,\text{GeV}/c^2$.

1 $[\pi\pi]_{1^{--}}$ dynamic isobar amplitude for $0.100 < t' < 0.141\,(\text{GeV}/c)^2$
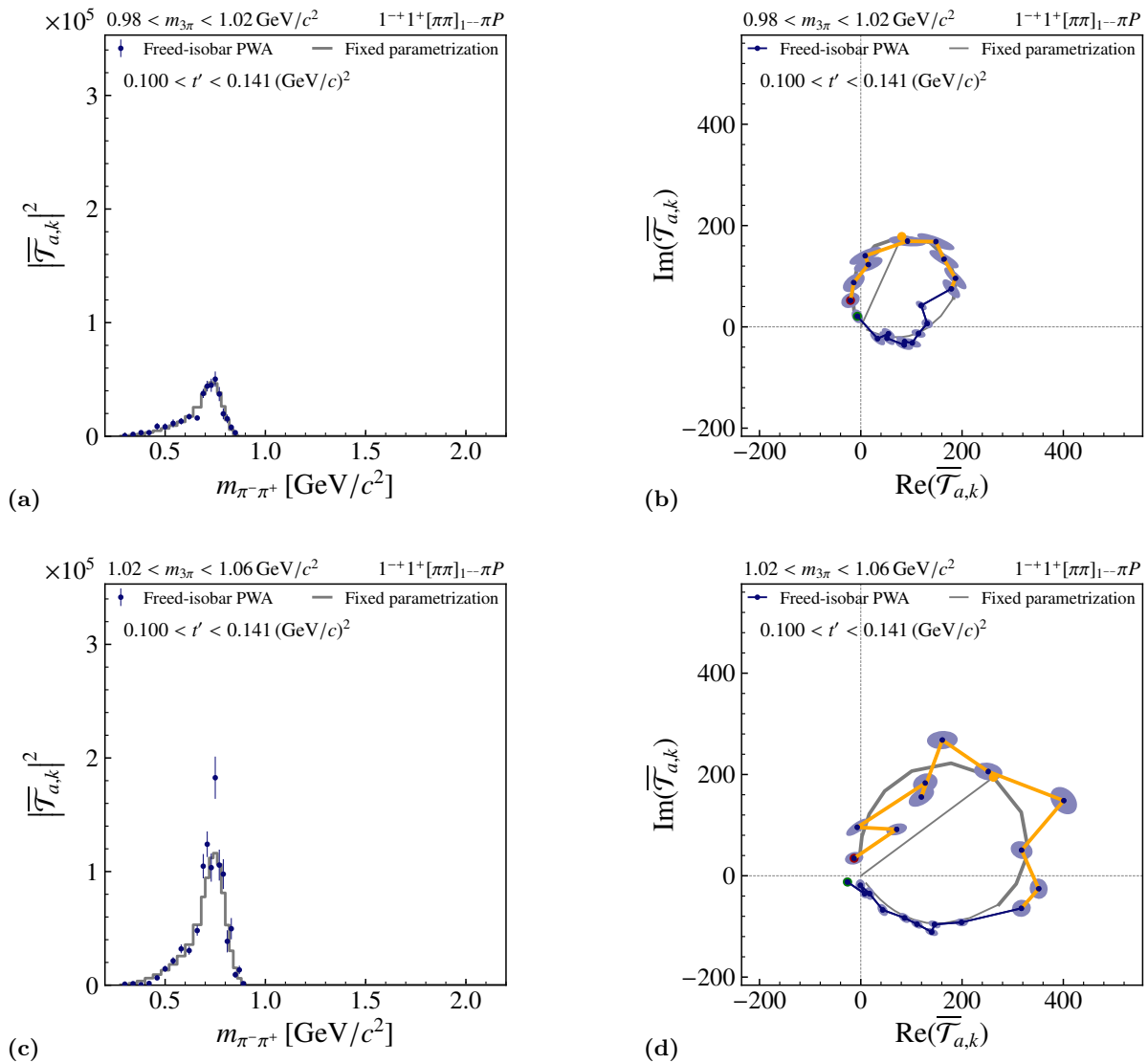
FIG. 17: Intensity distributions and Argand diagrams similar to Fig. 6 for $0.98 < m_{3\pi} < 1.06\,\text{GeV}/c^2$ and $0.100 < t' < 0.141\,(\text{GeV}/c)^2$.
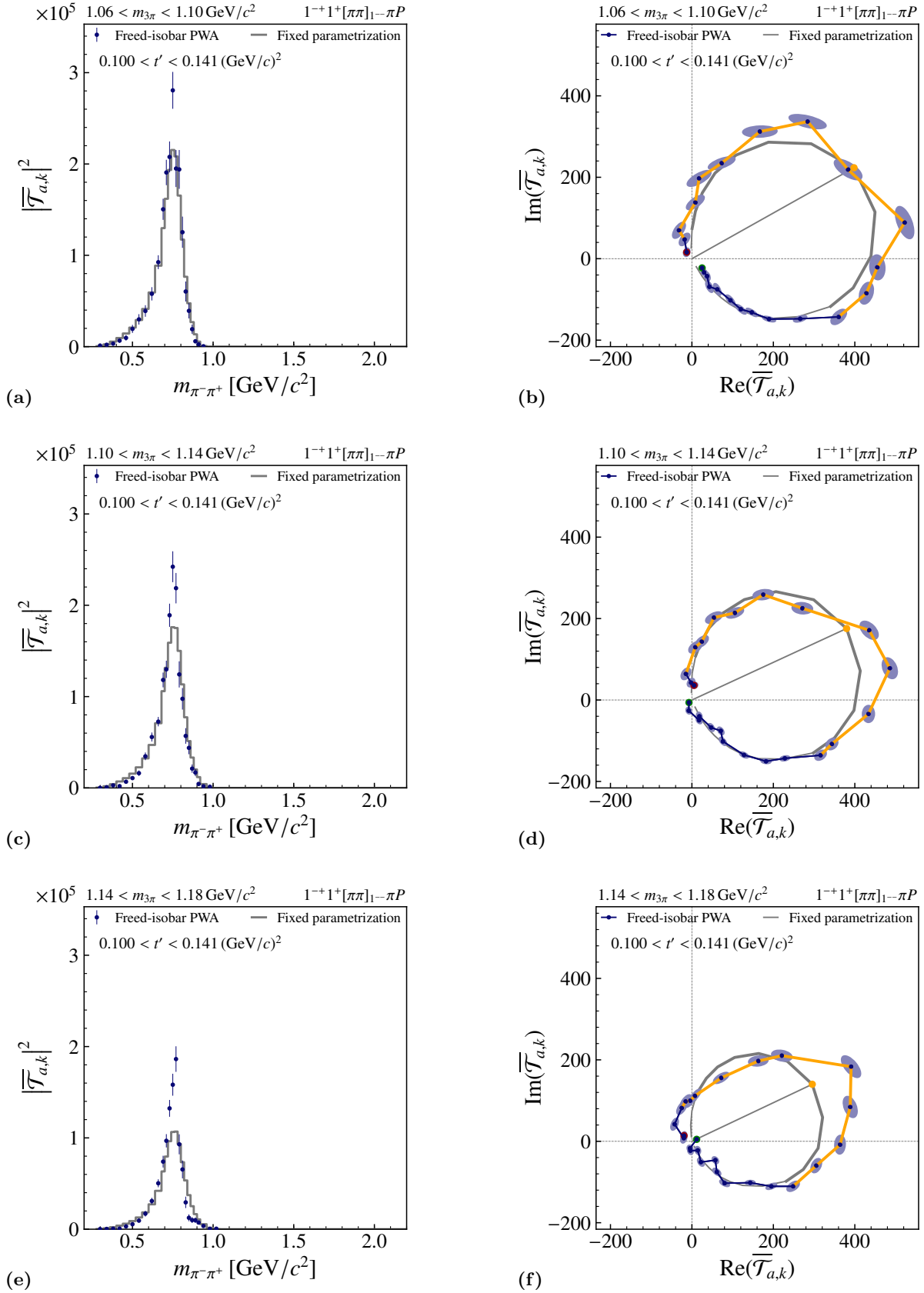
FIG. 18: Intensity distribution and Argand diagrams similar to Fig. 6 for $1.06 < m_{3\pi} < 1.18\,\text{GeV}/c^2$ and $0.100 < t' < 0.141\,(\text{GeV}/c)^2$.
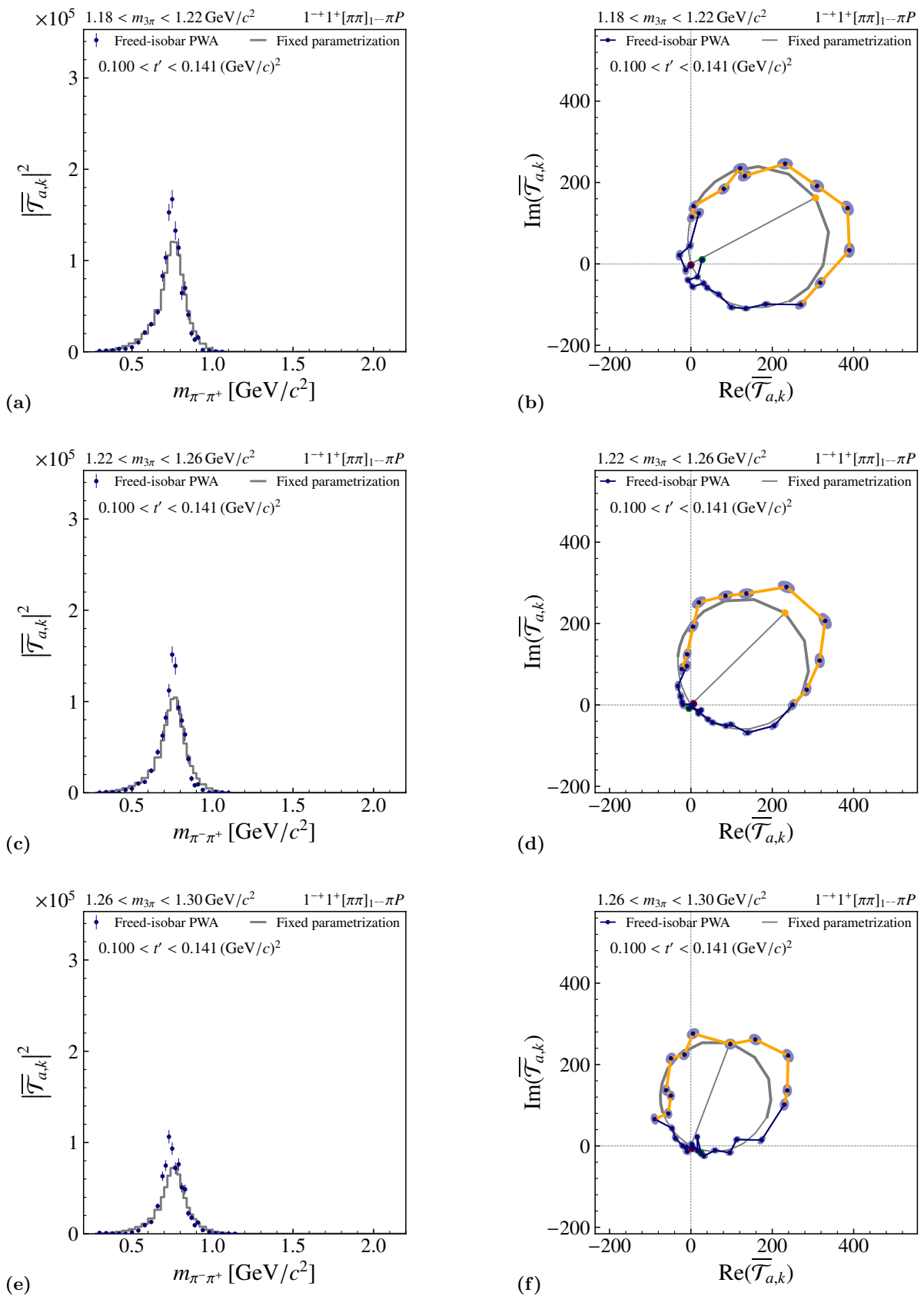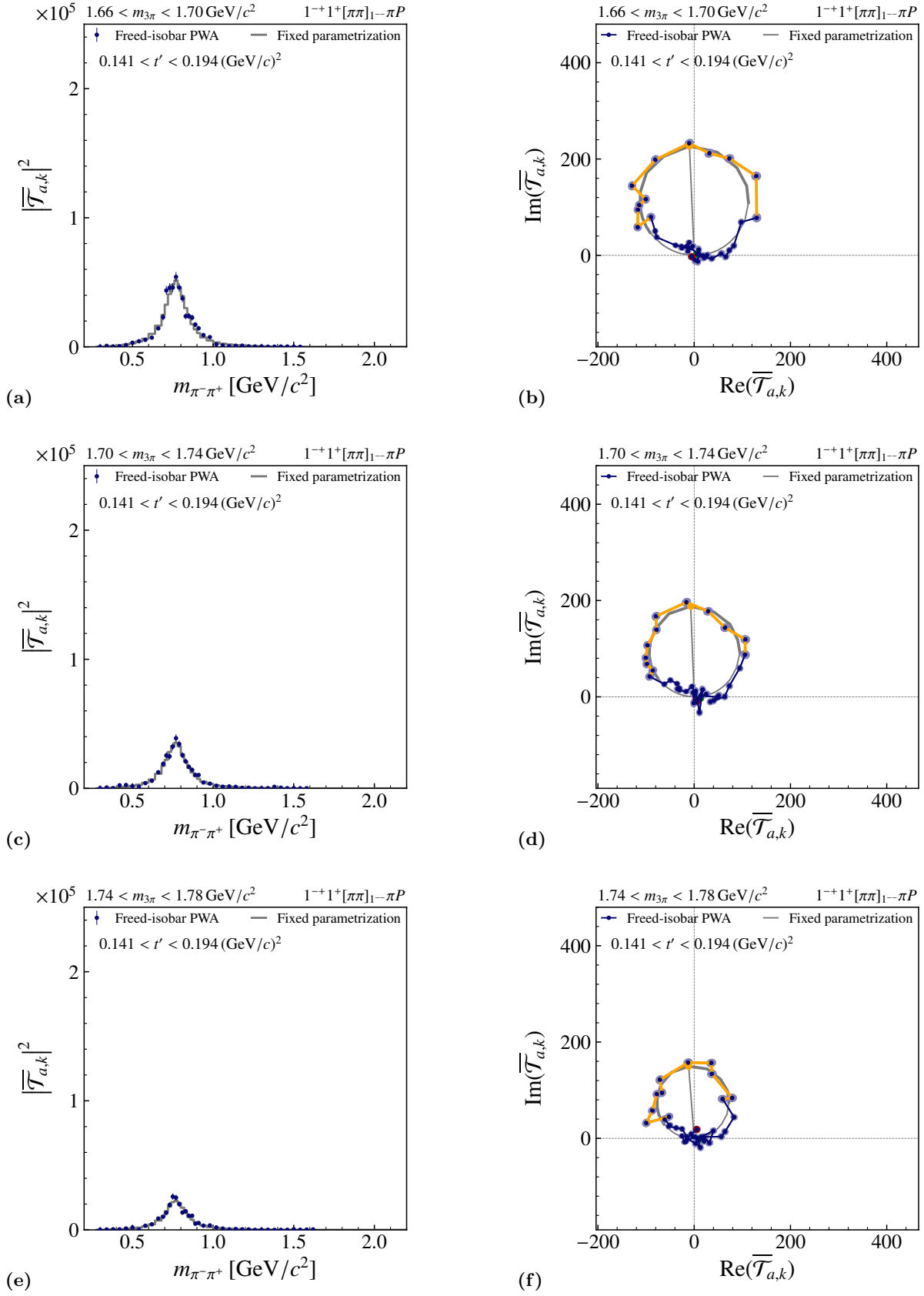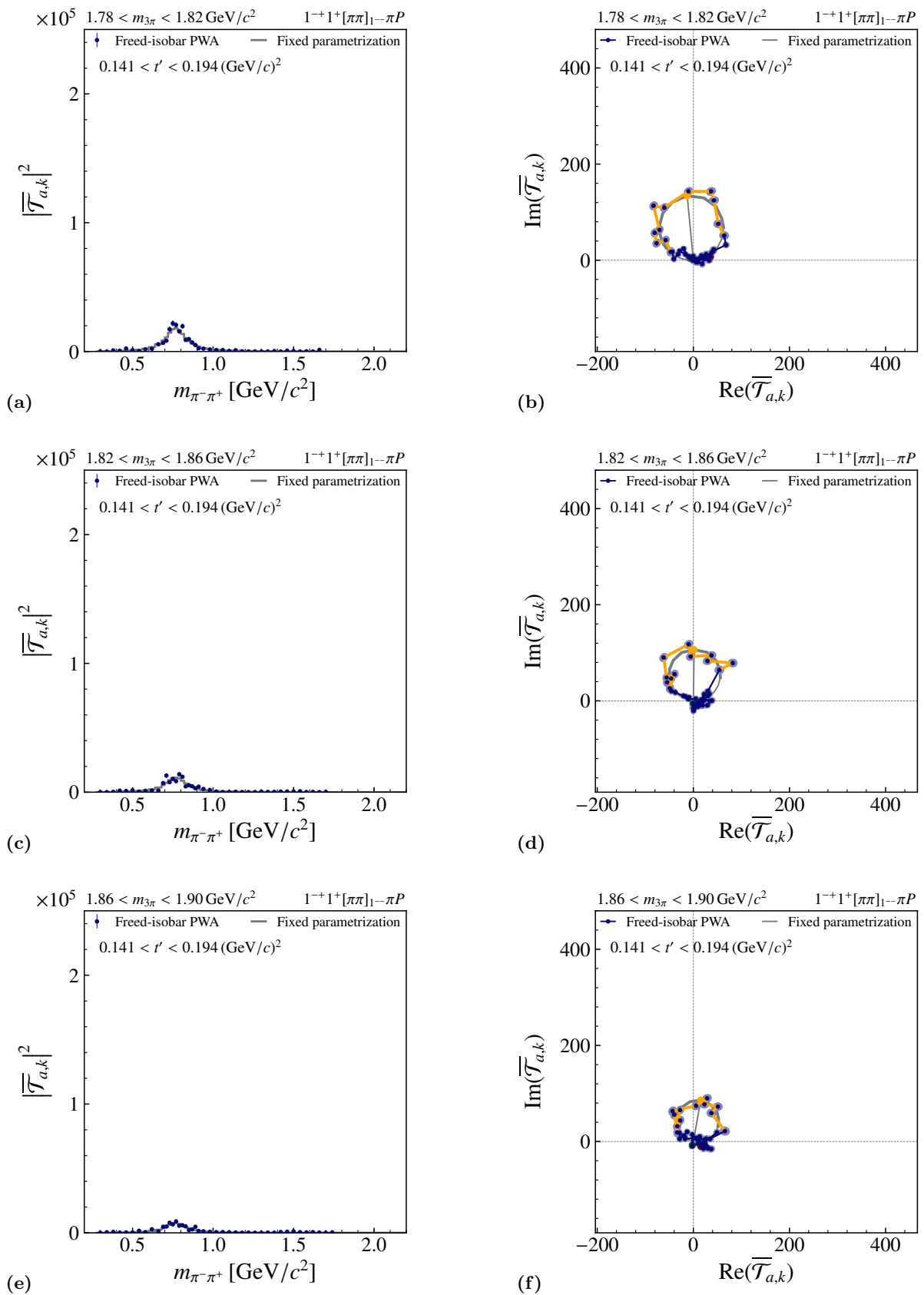
FIG. 19: Intensity distribution and Argand diagrams similar to Fig. 6 for $1.18 < m_{3\pi} < 1.30 \, \text{GeV}/c^2$ and $0.100 < t' < 0.141 \, (\text{GeV}/c)^2$.
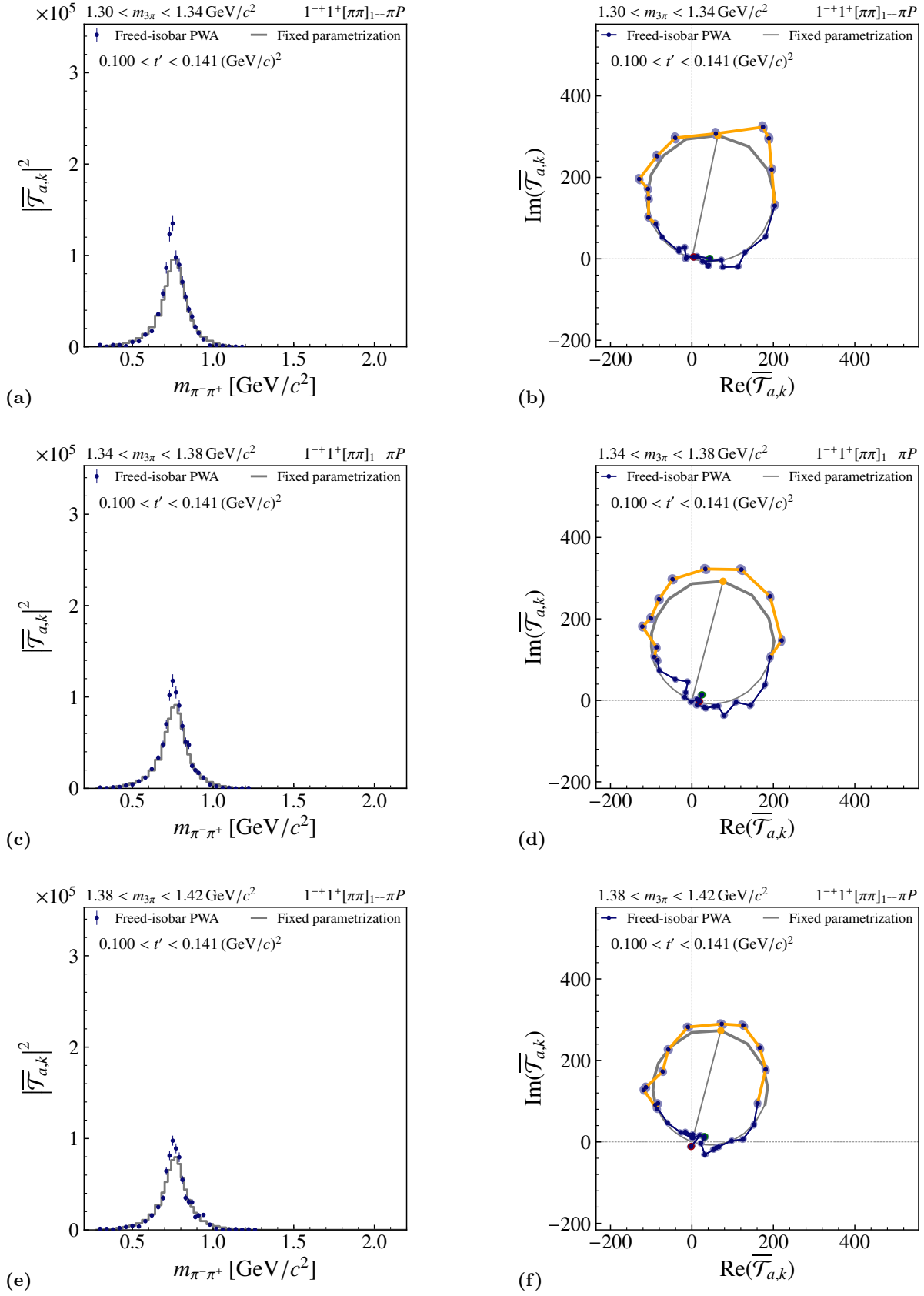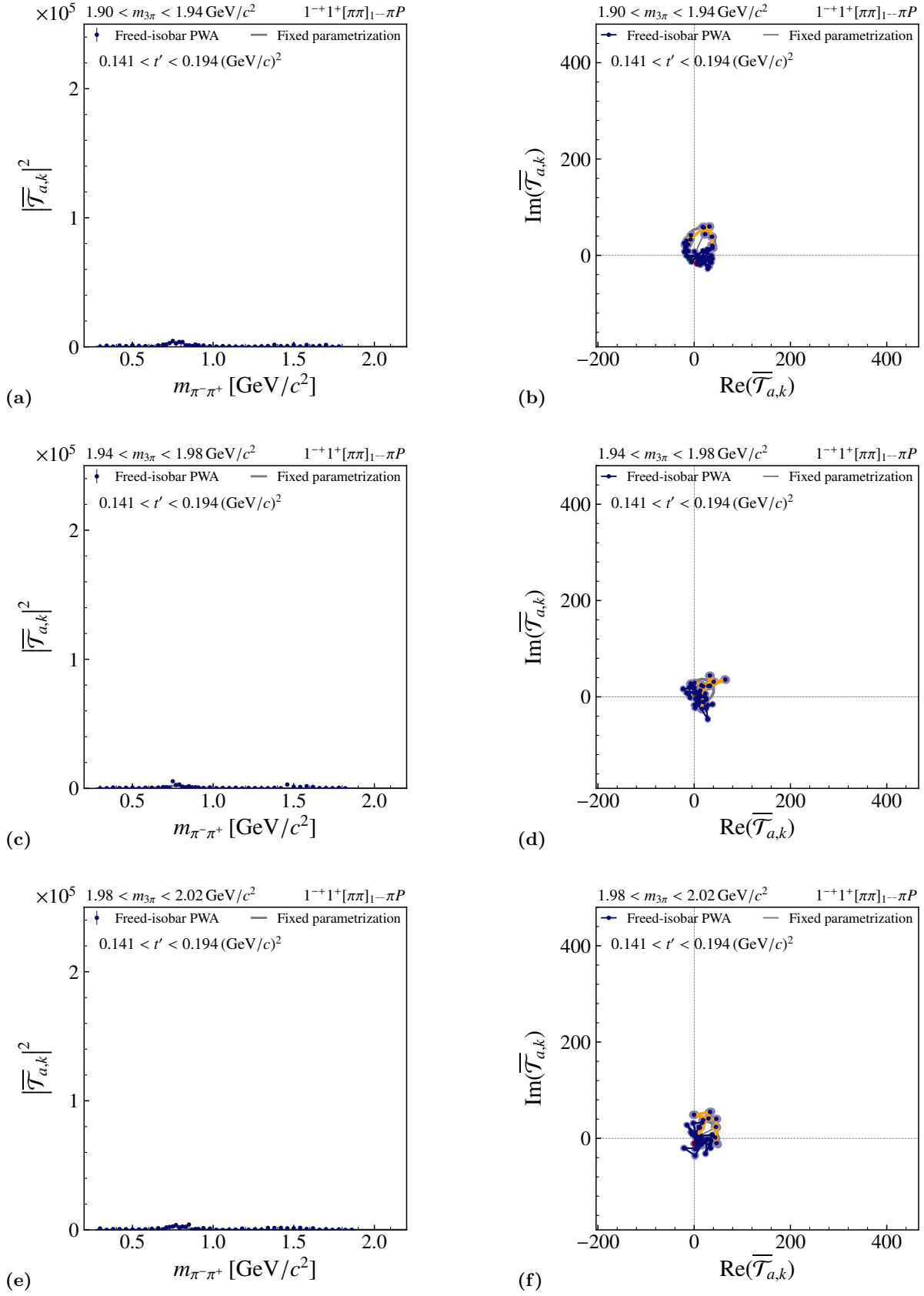
FIG. 20: Intensity distribution and Argand diagrams similar to Fig. 6 for $1.30 < m_{3\pi} < 1.42\,\text{GeV}/c^2$ and $0.100 < t' < 0.141\,(\text{GeV}/c)^2$.
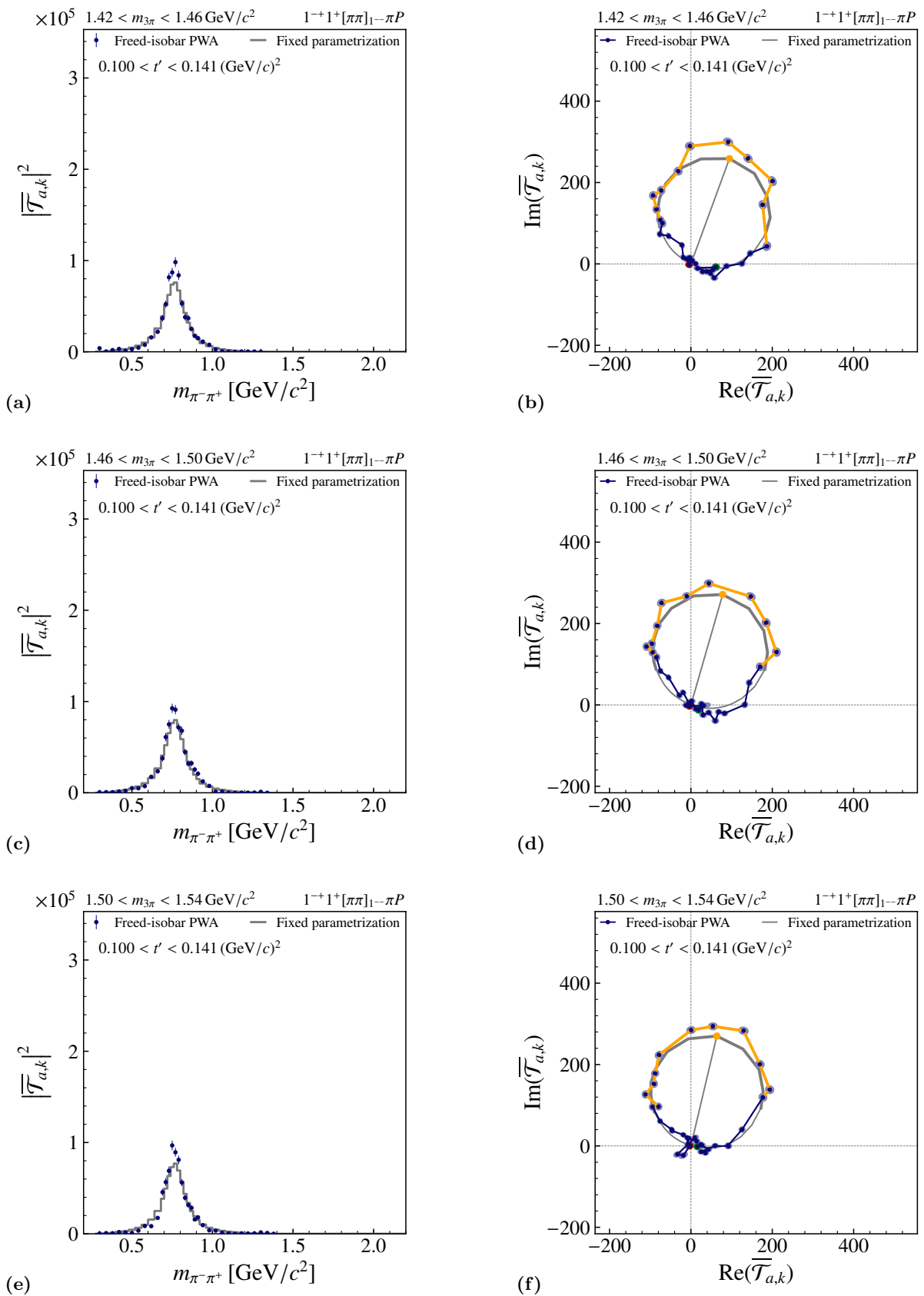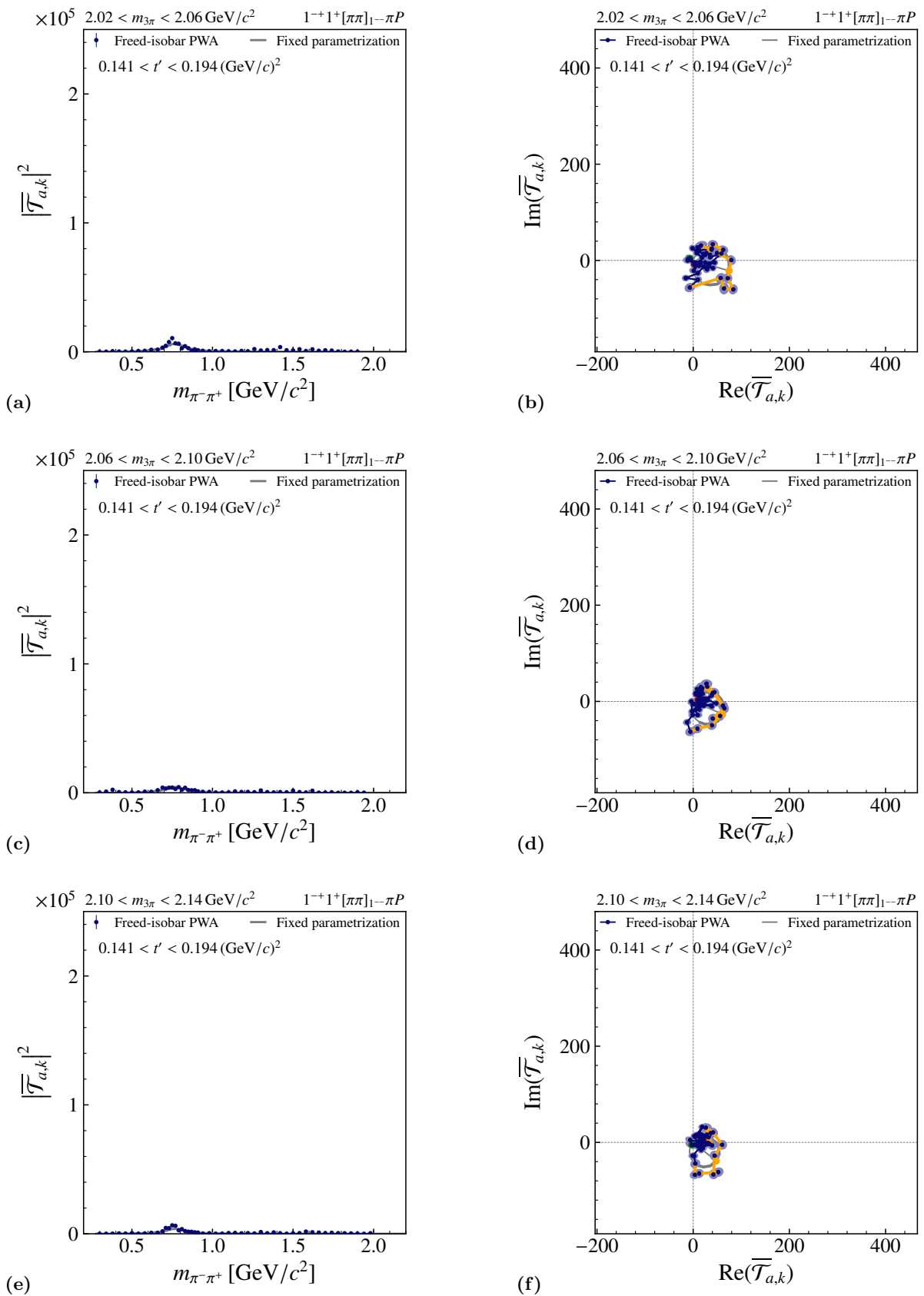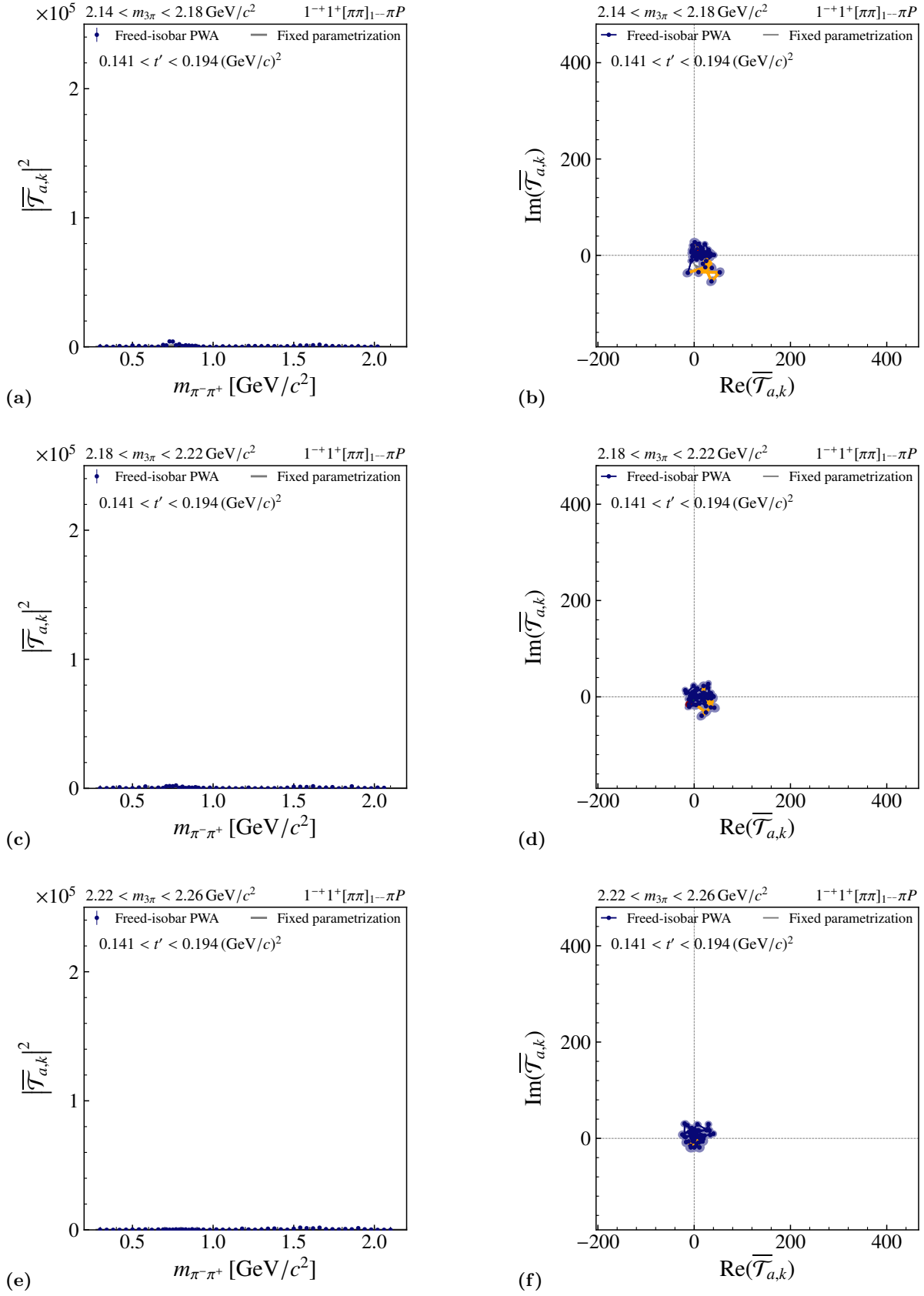
FIG. 21: Intensity distribution and Argand diagrams similar to Fig. 6 for $1.42 < m_{3\pi} < 1.54 \, \mathrm{GeV}/c^2$ and $0.100 < t' < 0.141 \, (\mathrm{GeV}/c)^2$.
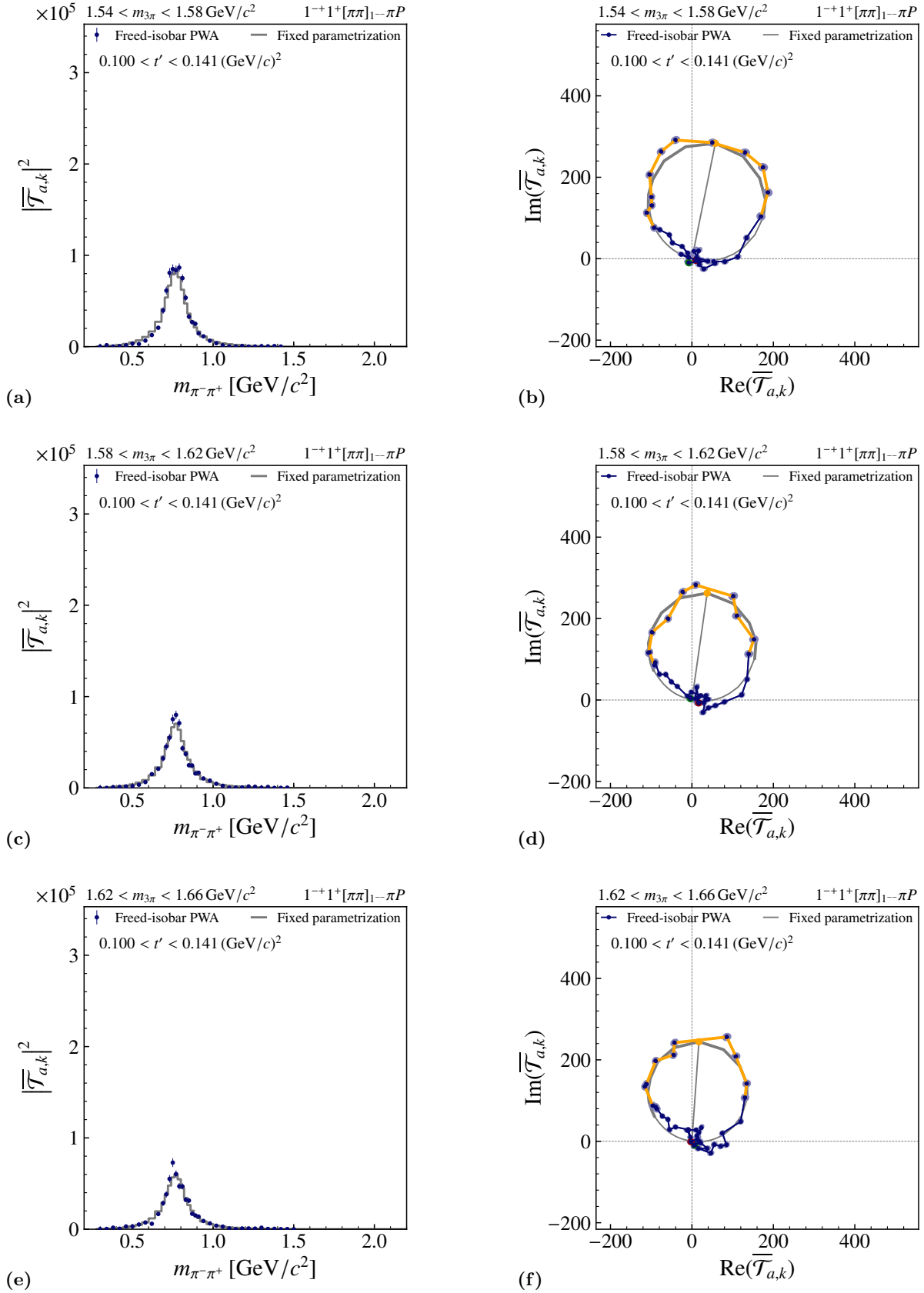
FIG. 22: Intensity distribution and Argand diagrams similar to Fig. 6 for $1.54 < m_{3\pi} < 1.66\,\mathrm{GeV}/c^2$ and $0.100 < t' < 0.141\,(\mathrm{GeV}/c)^2$.
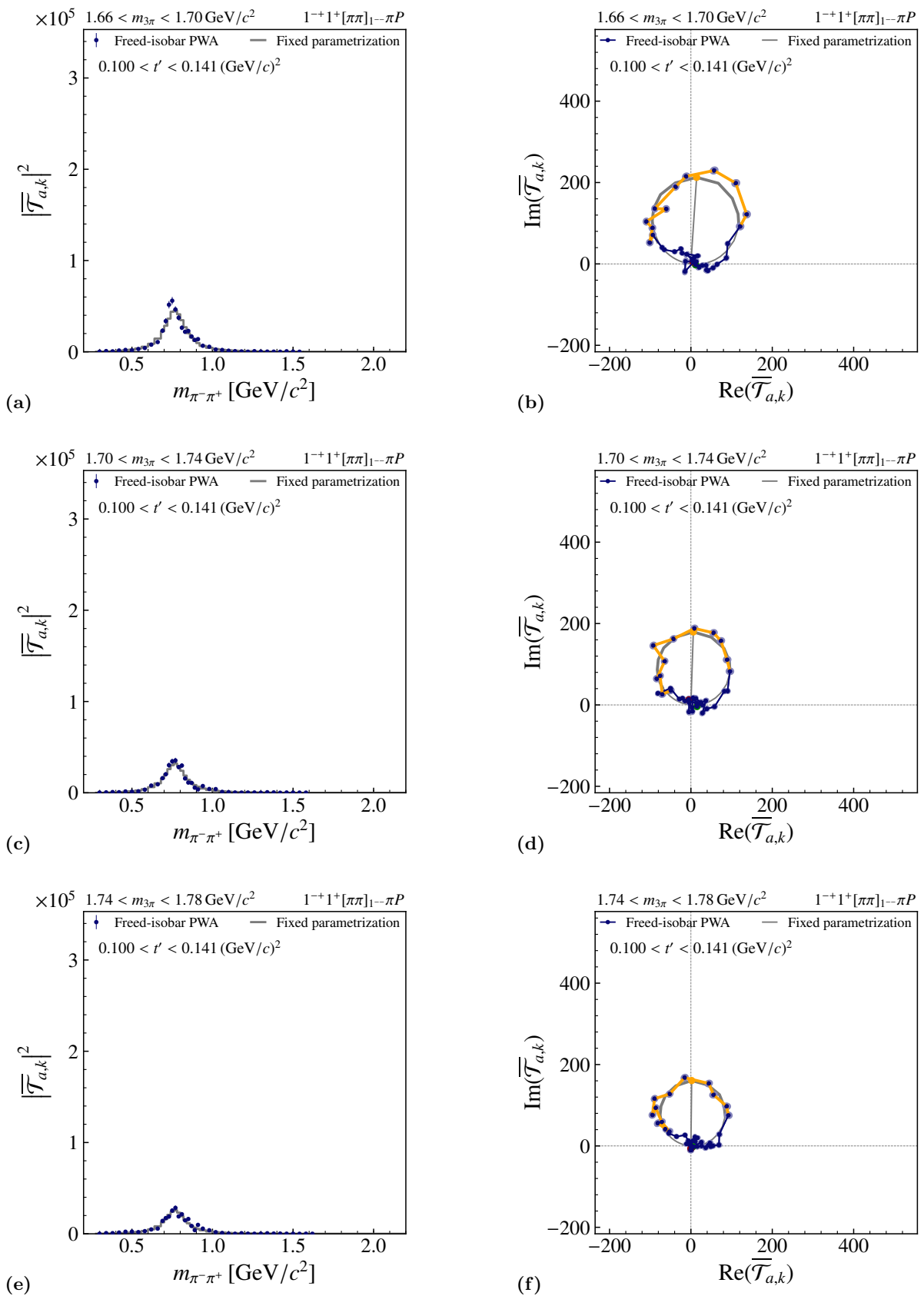
FIG. 23: Intensity distribution and Argand diagrams similar to Fig. 6 for $1.66 < m_{3\pi} < 1.78\,\mathrm{GeV}/c^2$ and $0.100 < t' < 0.141\,(\mathrm{GeV}/c)^2$.
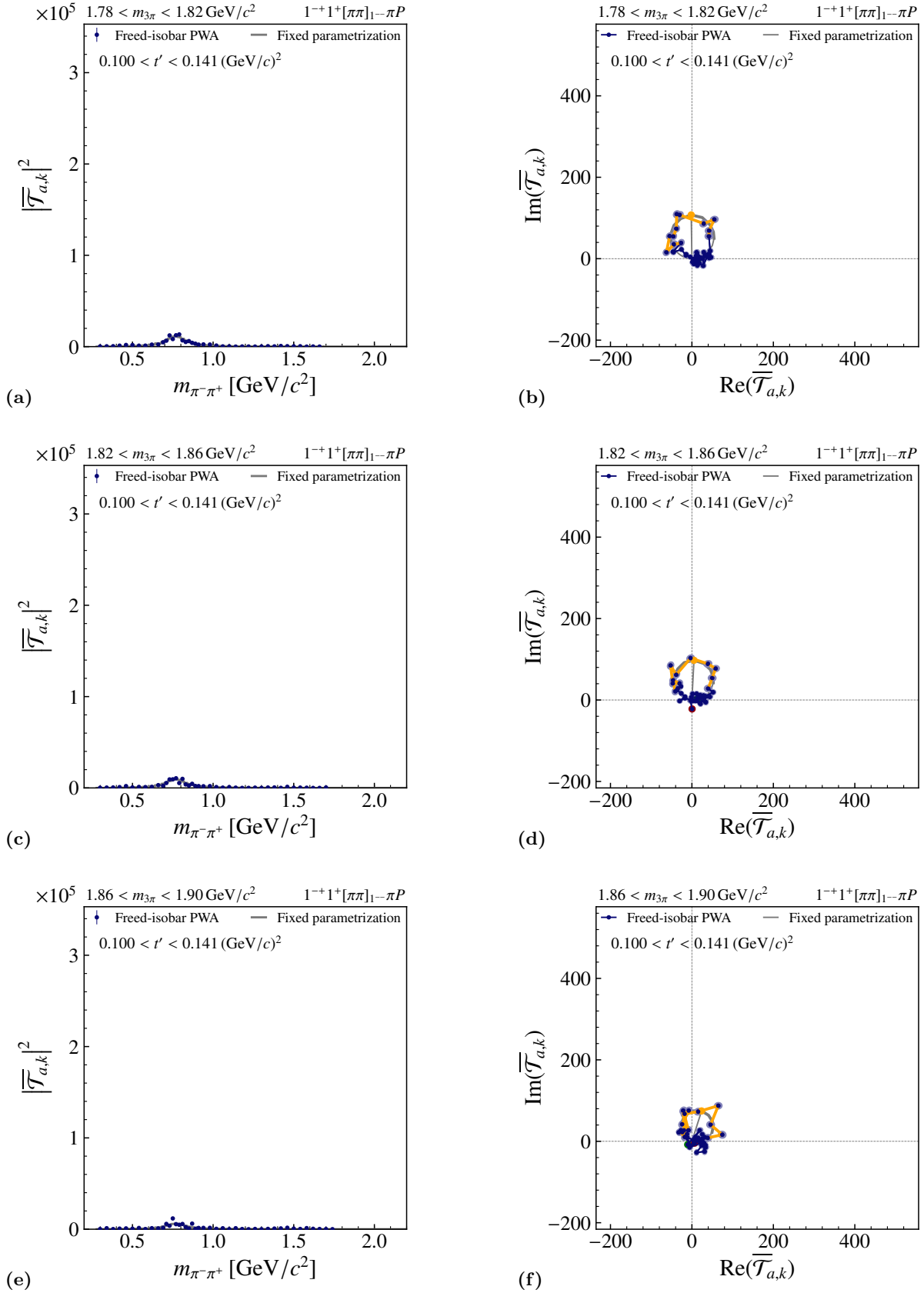
FIG. 24: Intensity distribution and Argand diagrams similar to Fig. 6 for $1.78 < m_{3\pi} < 1.90\,\text{GeV}/c^2$ and $0.100 < t' < 0.141\,(\text{GeV}/c)^2$.
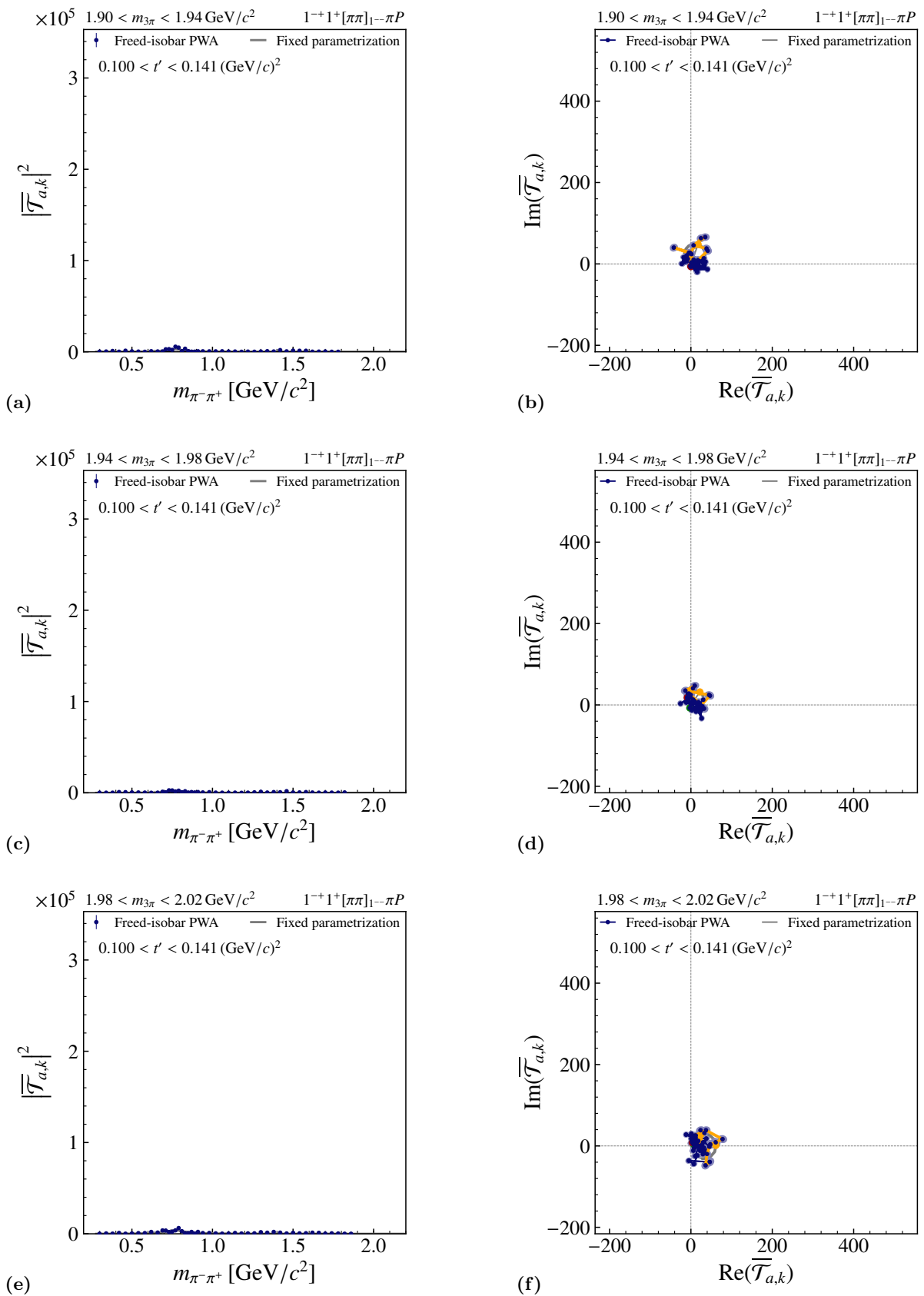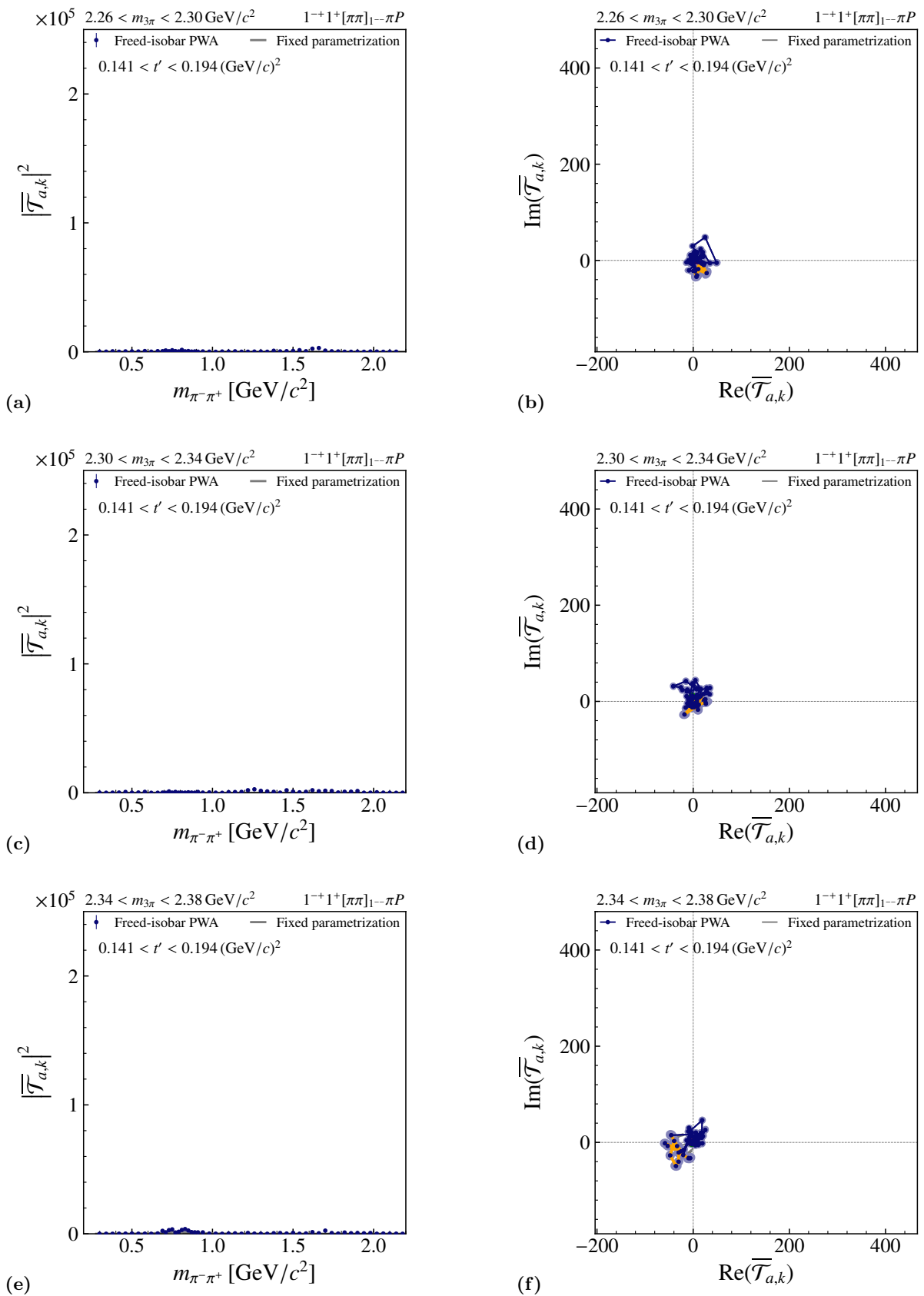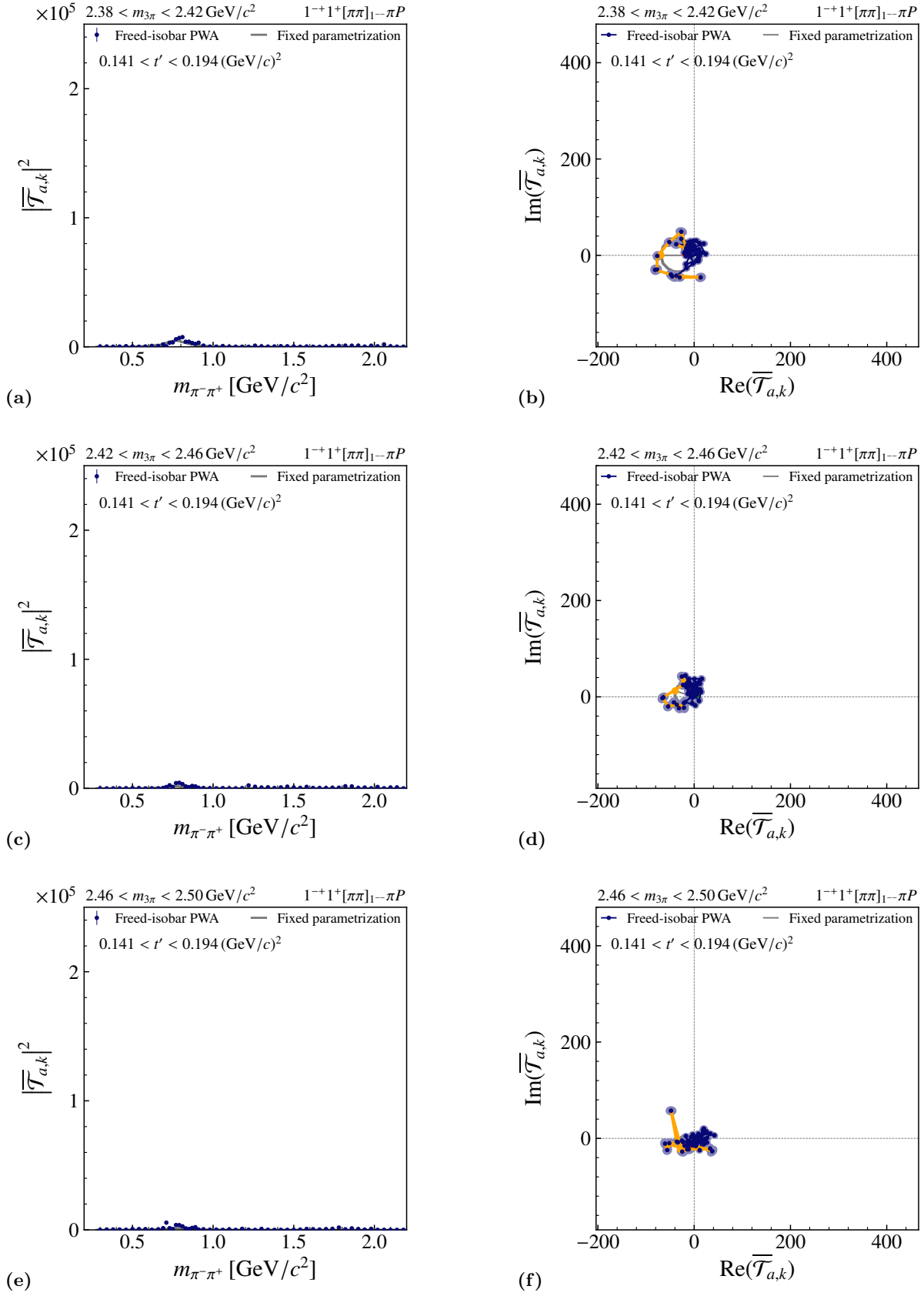
FIG. 25: Intensity distribution and Argand diagrams similar to Fig. 6 for $1.90 < m_{3\pi} < 2.02\,\mathrm{GeV}/c^2$ and $0.100 < t' < 0.141\,(\mathrm{GeV}/c)^2$.
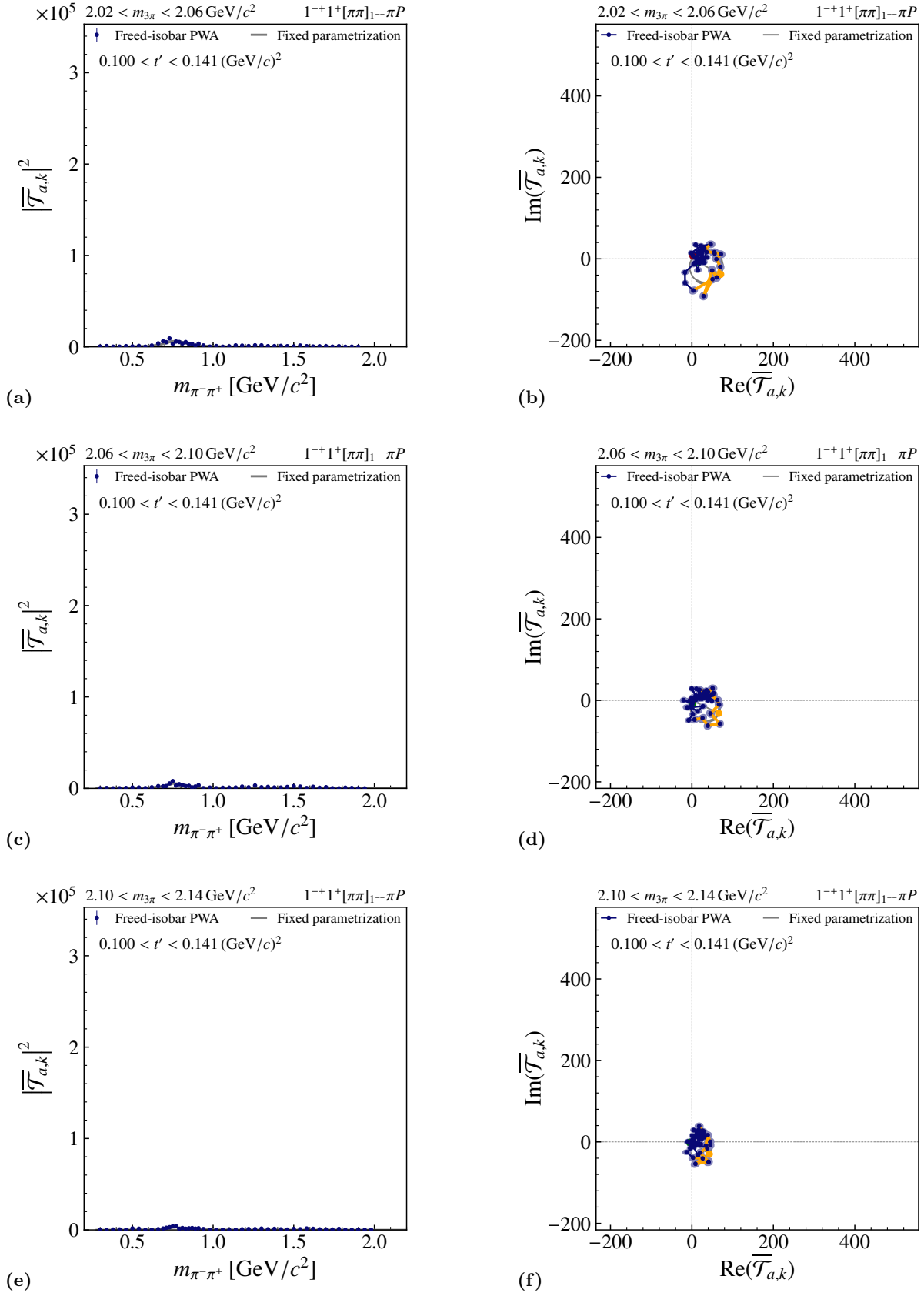
FIG. 26: Intensity distribution and Argand diagrams similar to Fig. 6 for $2.02 < m_{3\pi} < 2.14\,\mathrm{GeV}/c^2$ and $0.100 < t' < 0.141\,(\mathrm{GeV}/c)^2$.
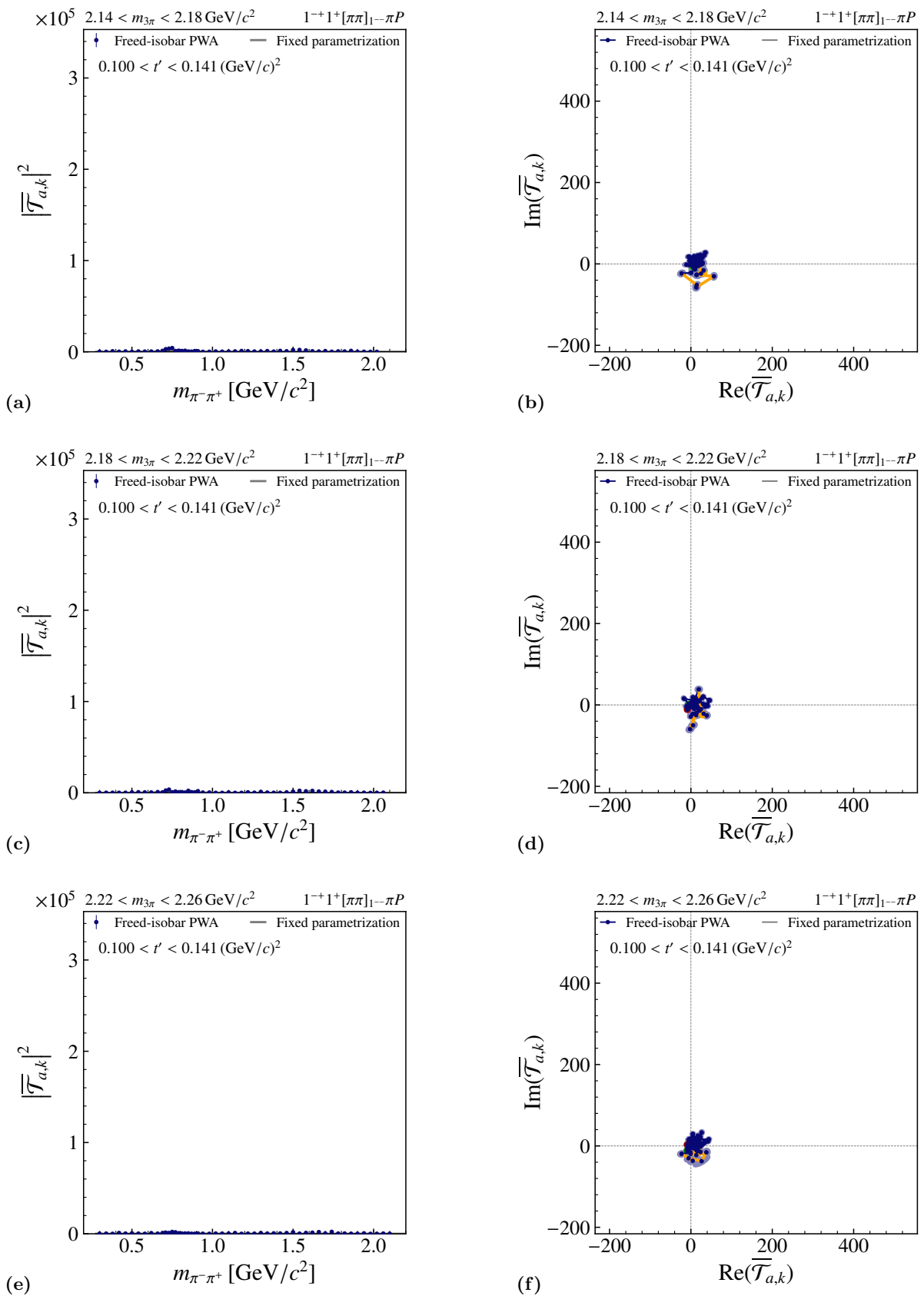
FIG. 27: Intensity distribution and Argand diagrams similar to Fig. 6 for $2.14 < m_{3\pi} < 2.26\,\mathrm{GeV}/c^2$ and $0.100 < t' < 0.141\,(\mathrm{GeV}/c)^2$.
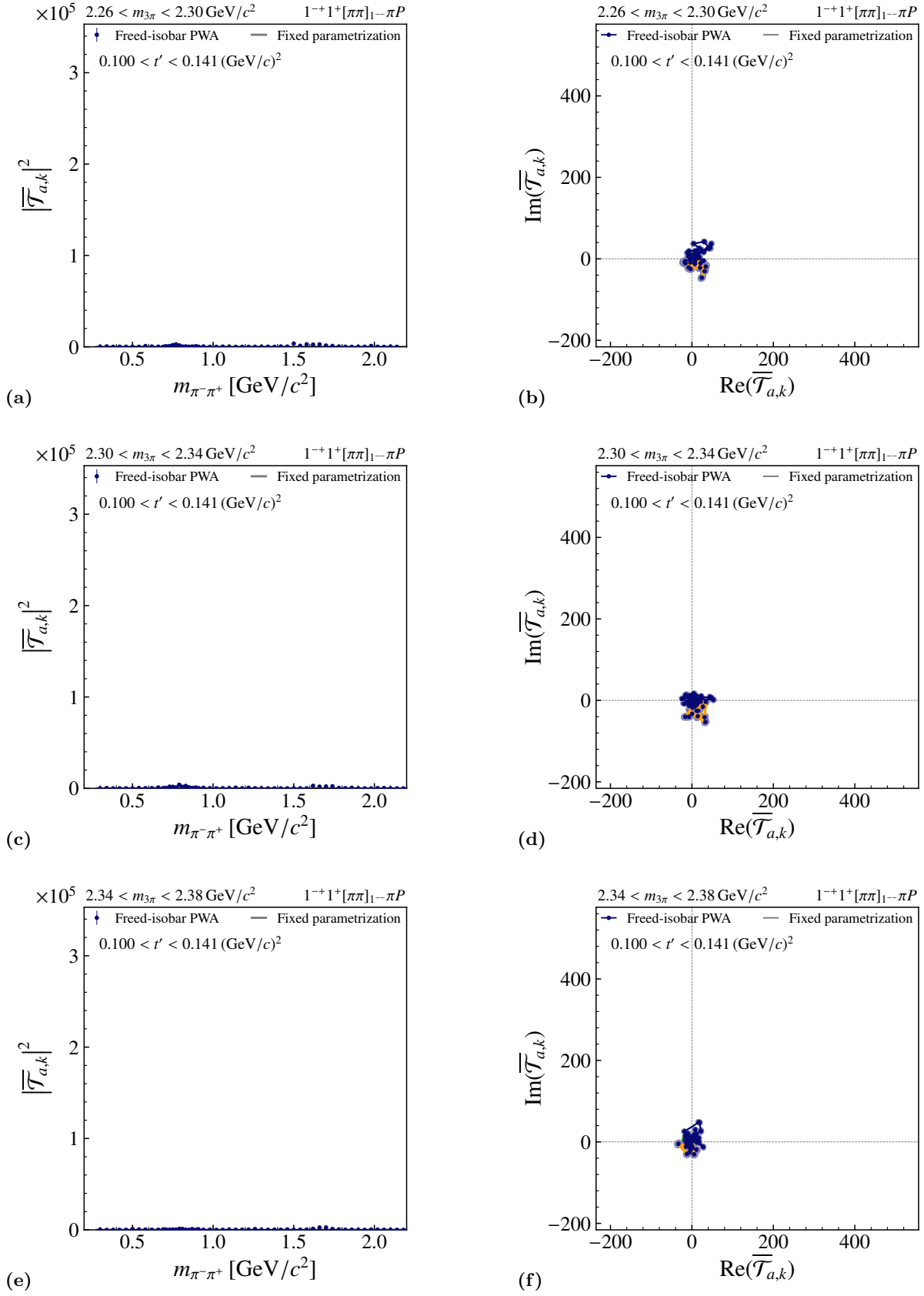
FIG. 28: Intensity distribution and Argand diagrams similar to Fig. 6 for $2.26 < m_{3\pi} < 2.38\,\text{GeV}/c^2$ and $0.100 < t' < 0.141\,(\text{GeV}/c)^2$.
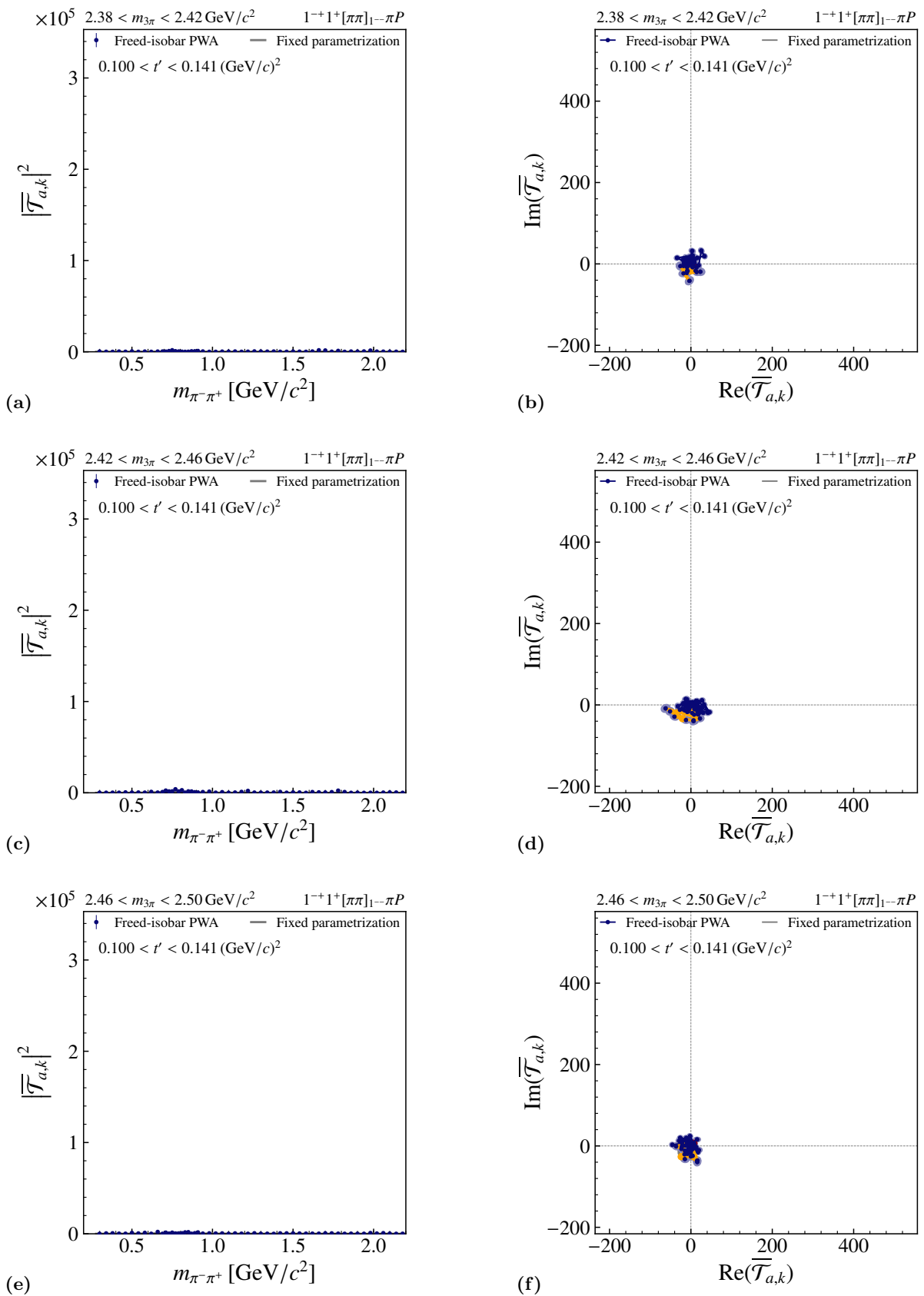
FIG. 29: Intensity distribution and Argand diagrams similar to Fig. 6 for $2.38 < m_{3\pi} < 2.50\,\mathrm{GeV}/c^2$ and $0.100 < t' < 0.141\,(\mathrm{GeV}/c)^2$.

2 $[\pi\pi]_{1^{--}}$ dynamic isobar amplitude for $0.141 < t' < 0.194\,(\mathrm{GeV}/c)^2$
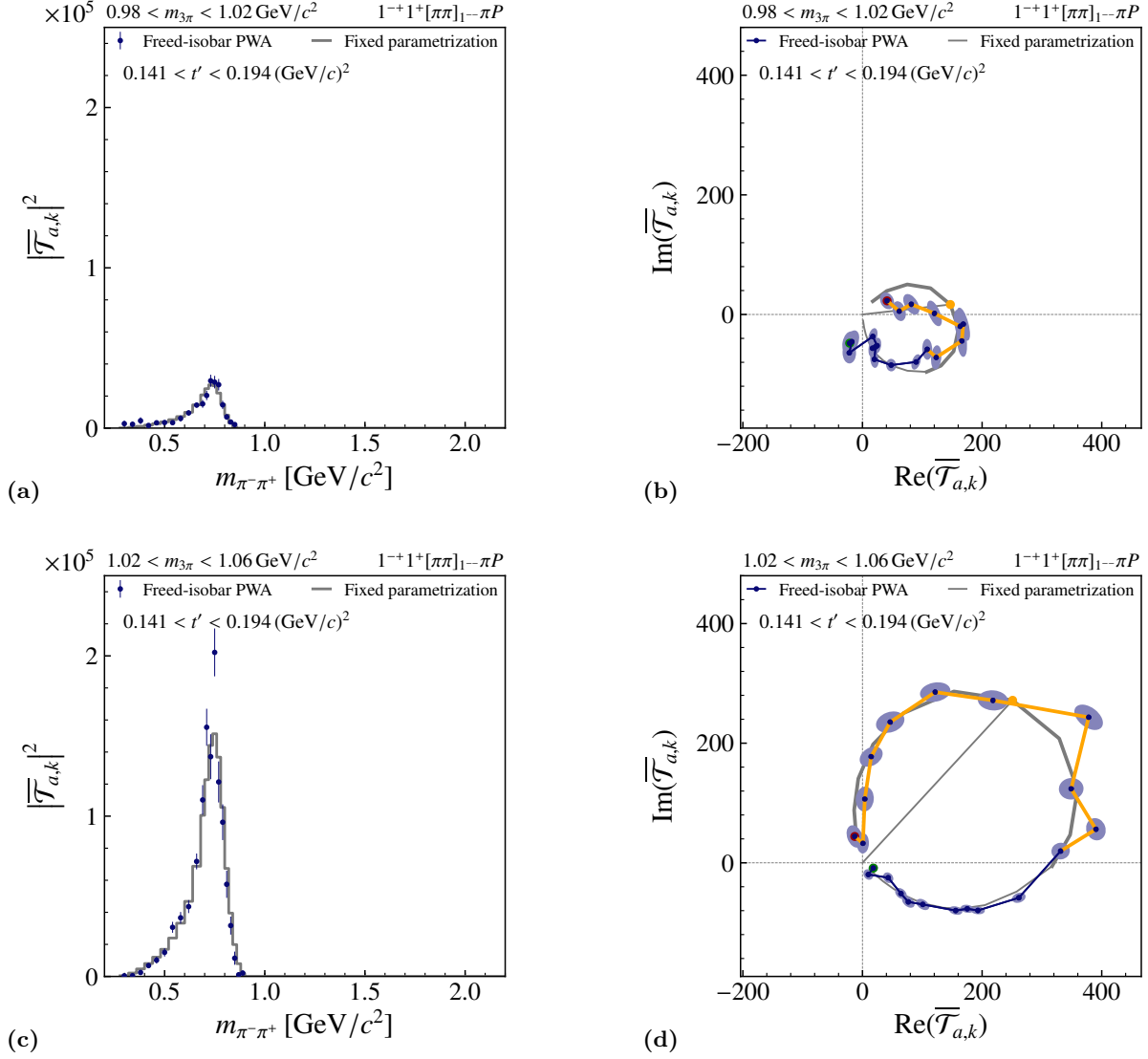
FIG. 30: Intensity distributions and Argand diagrams similar to Fig. 6 for $0.98 < m_{3\pi} < 1.06\,\mathrm{GeV}/c^2$ and $0.141 < t' < 0.194\,(\mathrm{GeV}/c)^2$.
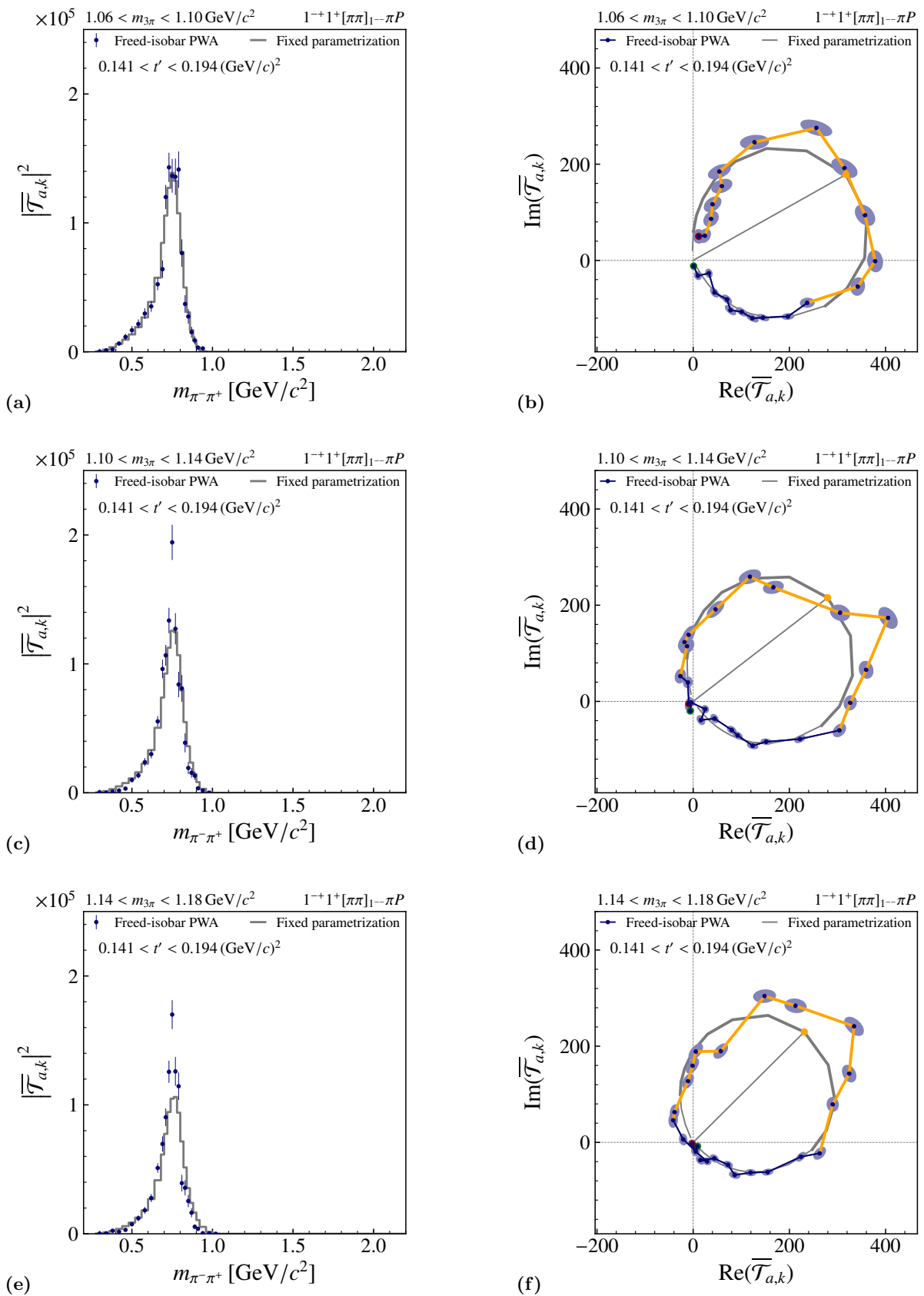
FIG. 31: Intensity distribution and Argand diagrams similar to Fig. 6 for $1.06 < m_{3\pi} < 1.18\,\mathrm{GeV}/c^2$ and $0.141 < t' < 0.194\,(\mathrm{GeV}/c)^2$.
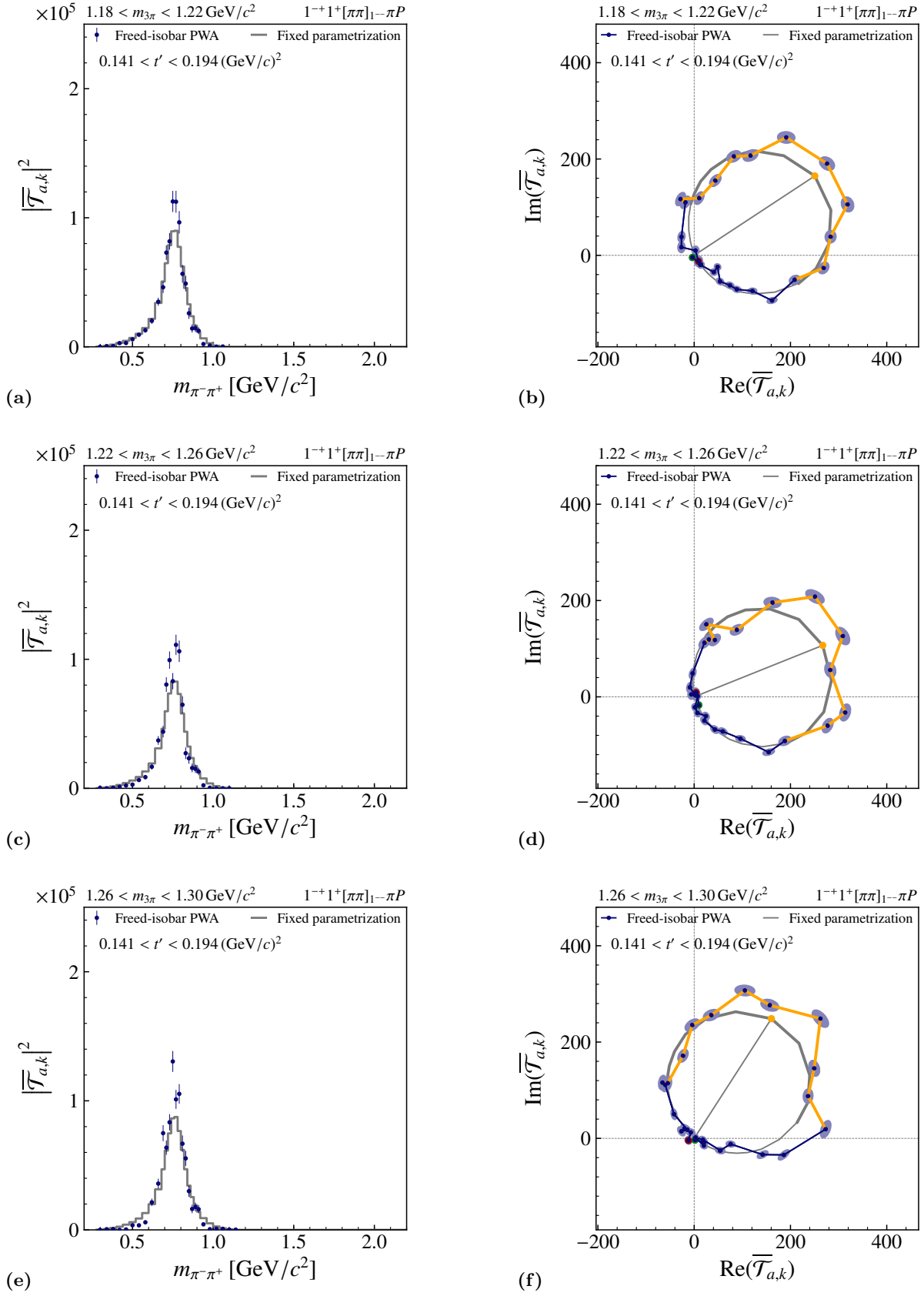
FIG. 32: Intensity distribution and Argand diagrams similar to Fig. 6 for $1.18 < m_{3\pi} < 1.30 \, \text{GeV}/c^2$ and $0.141 < t' < 0.194 \, (\text{GeV}/c)^2$.
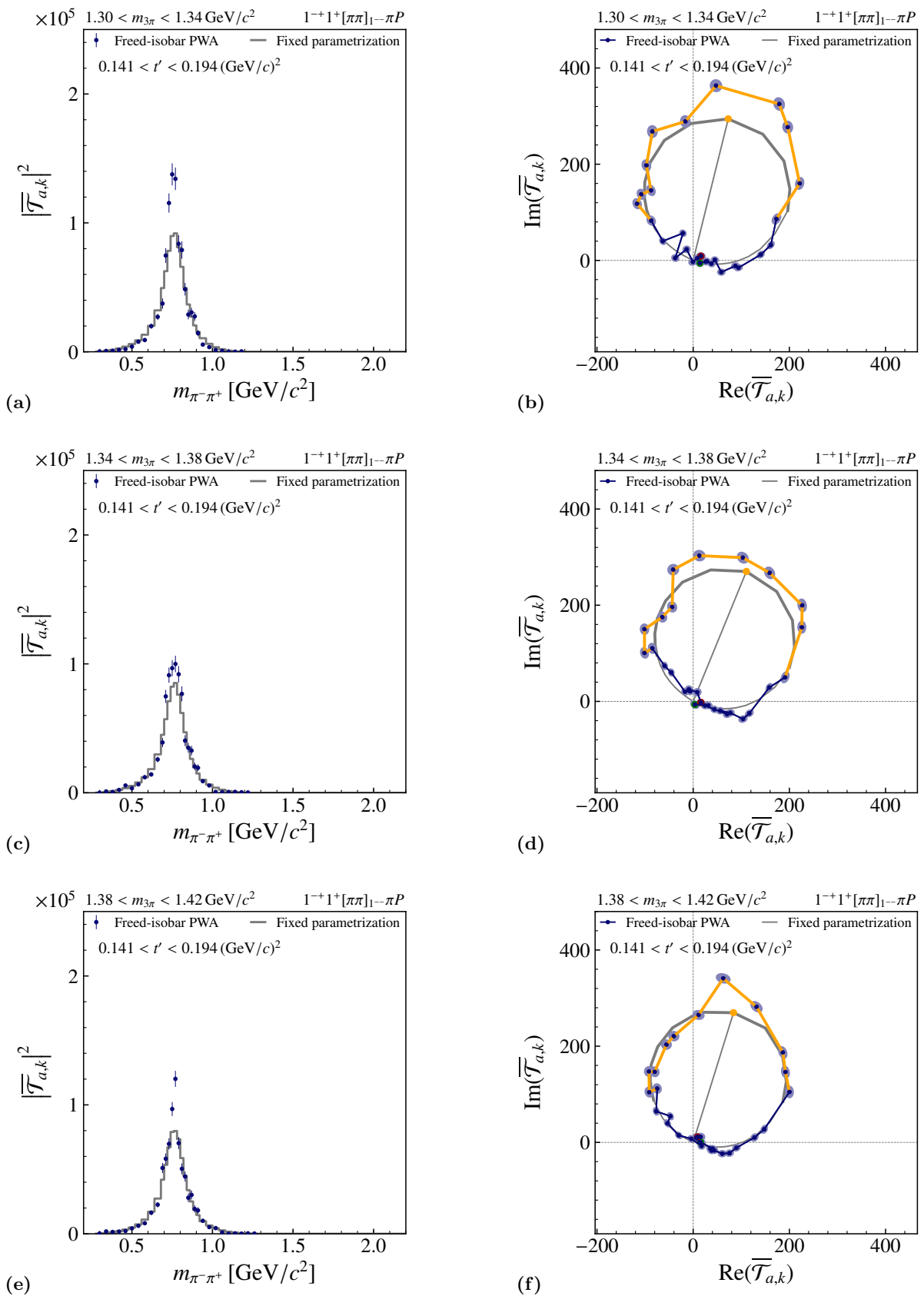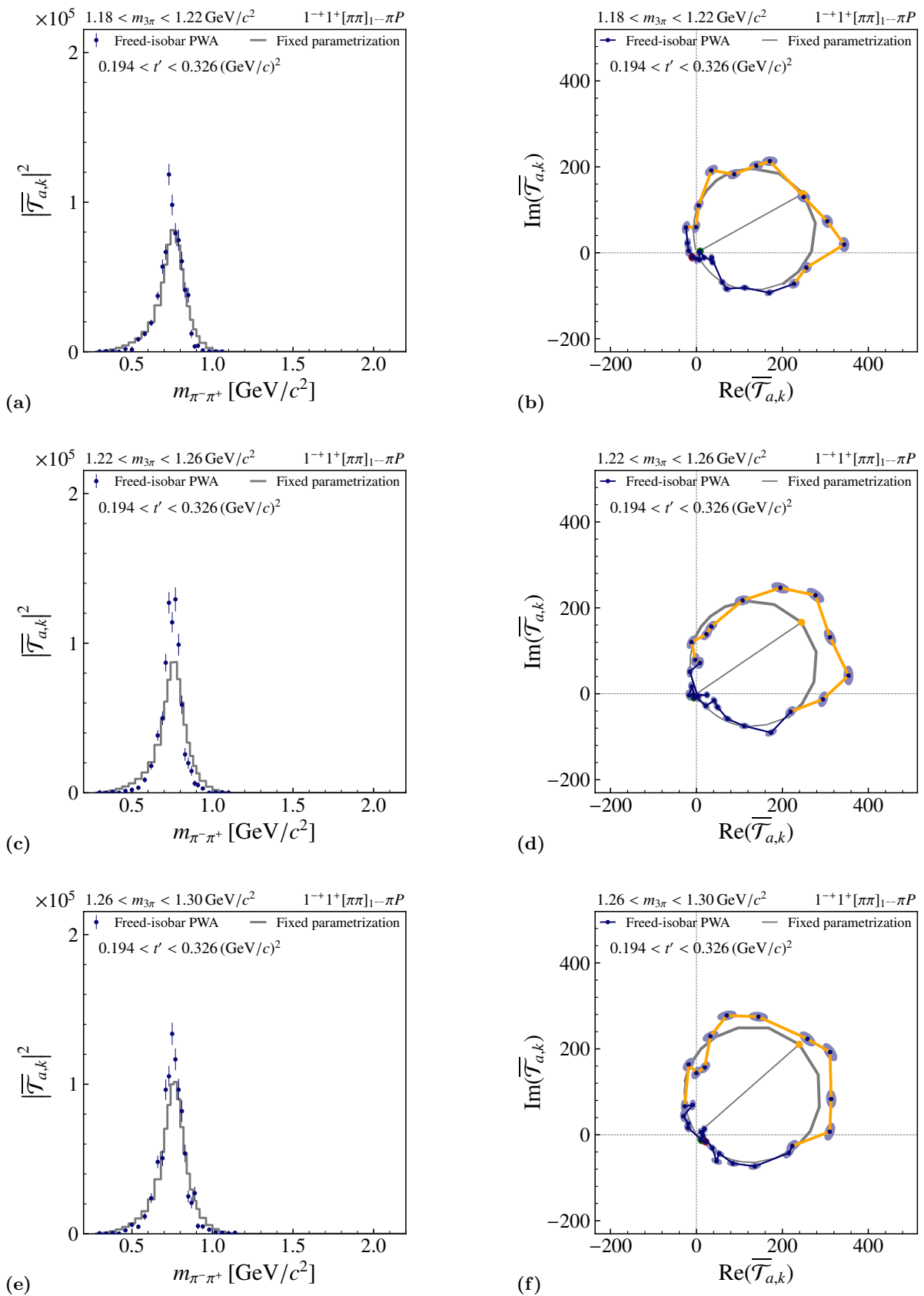
FIG. 33: Intensity distribution and Argand diagrams similar to Fig. 6 for $1.30 < m_{3\pi} < 1.42\,\mathrm{GeV}/c^2$ and $0.141 < t' < 0.194\,(\mathrm{GeV}/c)^2$.
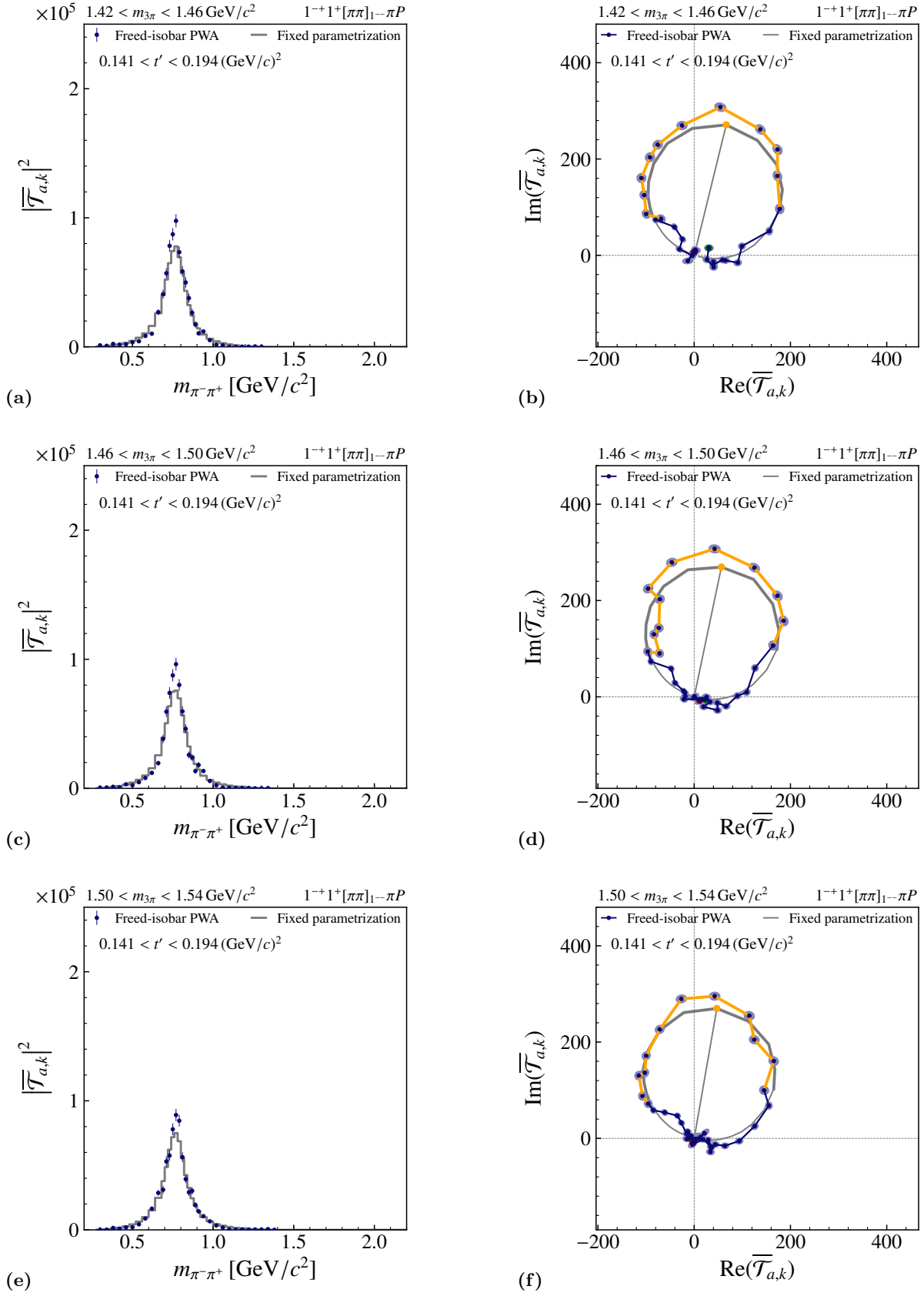
FIG. 34: Intensity distribution and Argand diagrams similar to Fig. 6 for $1.42 < m_{3\pi} < 1.54\,\text{GeV}/c^2$ and $0.141 < t' < 0.194\,(\text{GeV}/c)^2$.
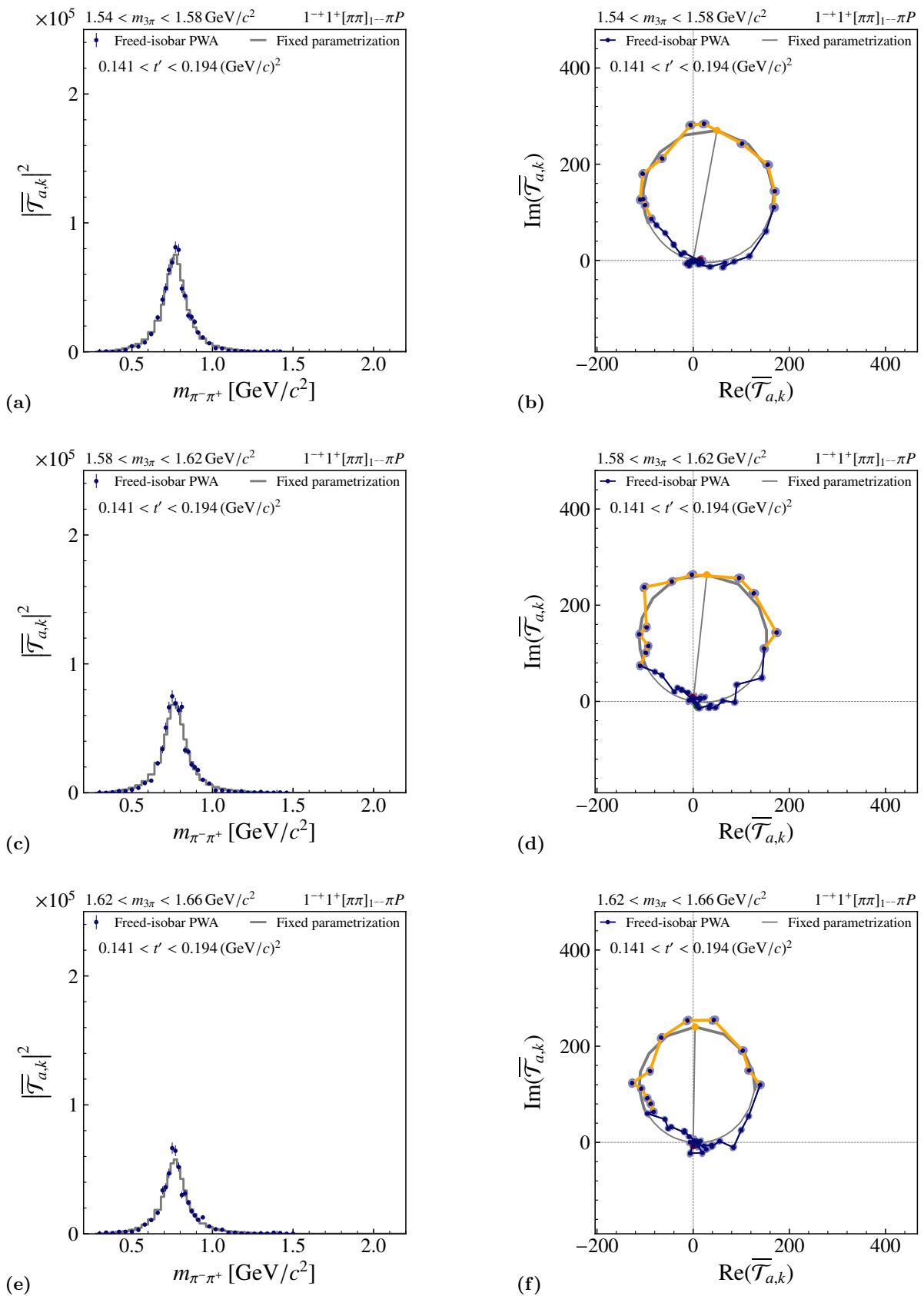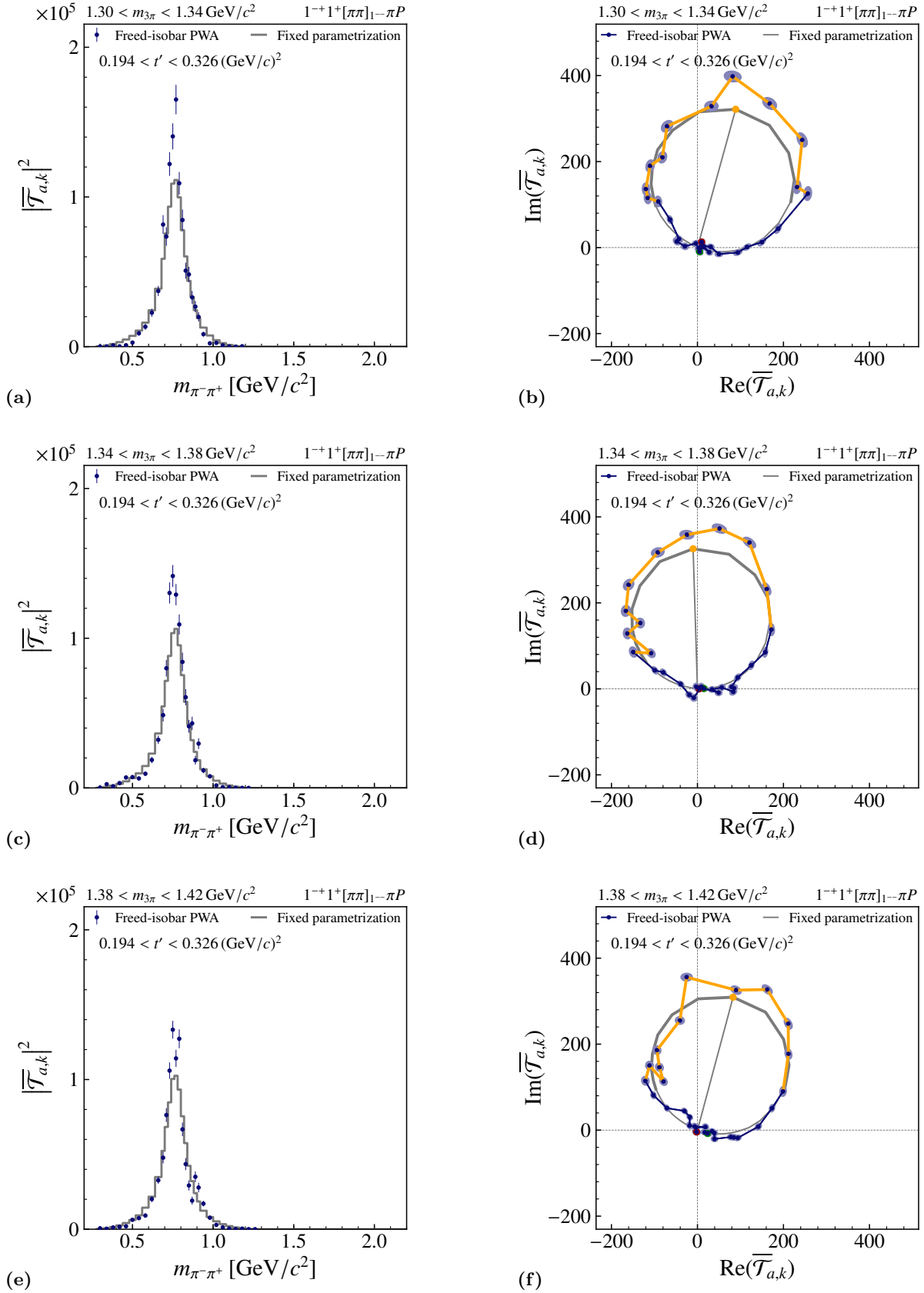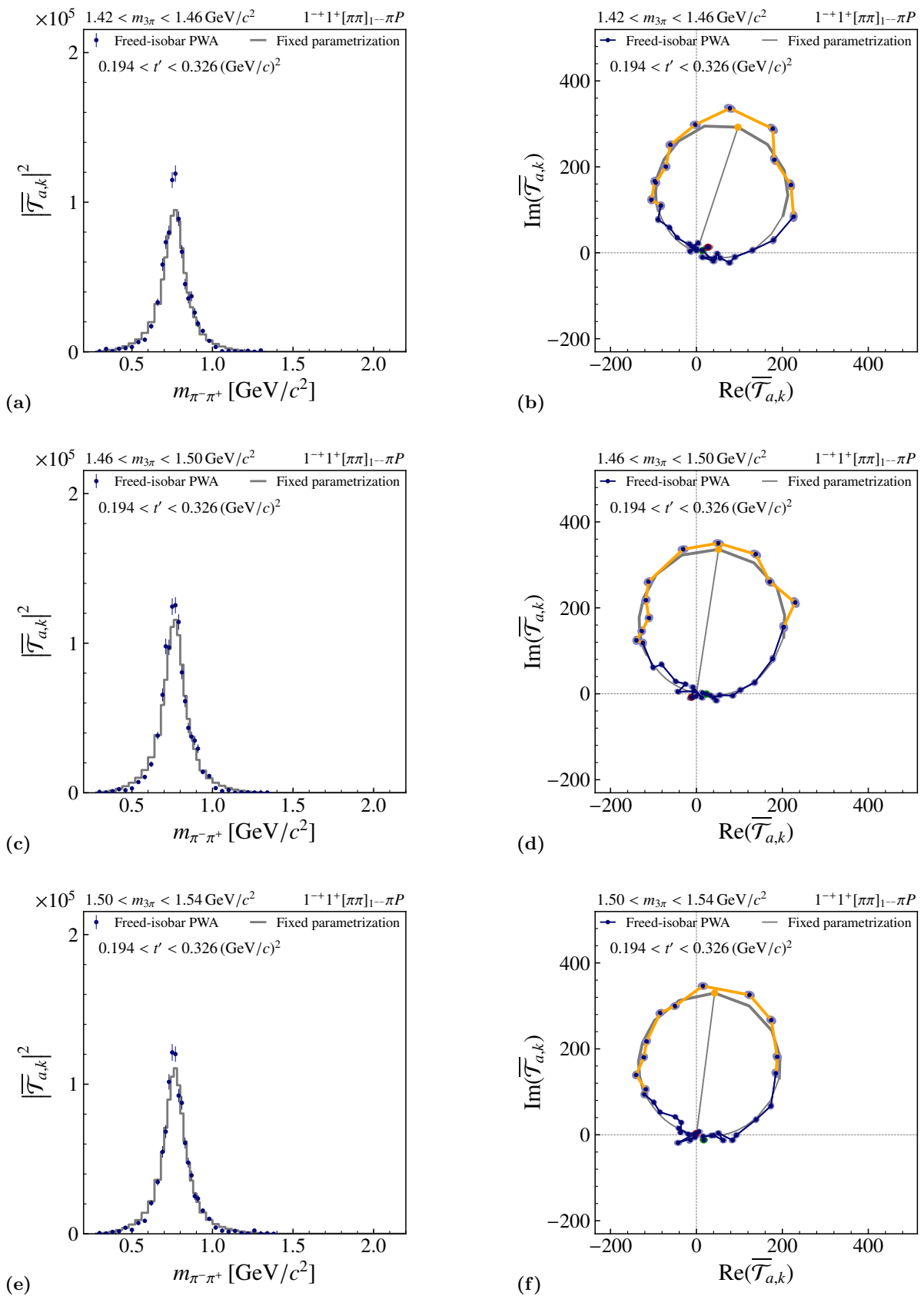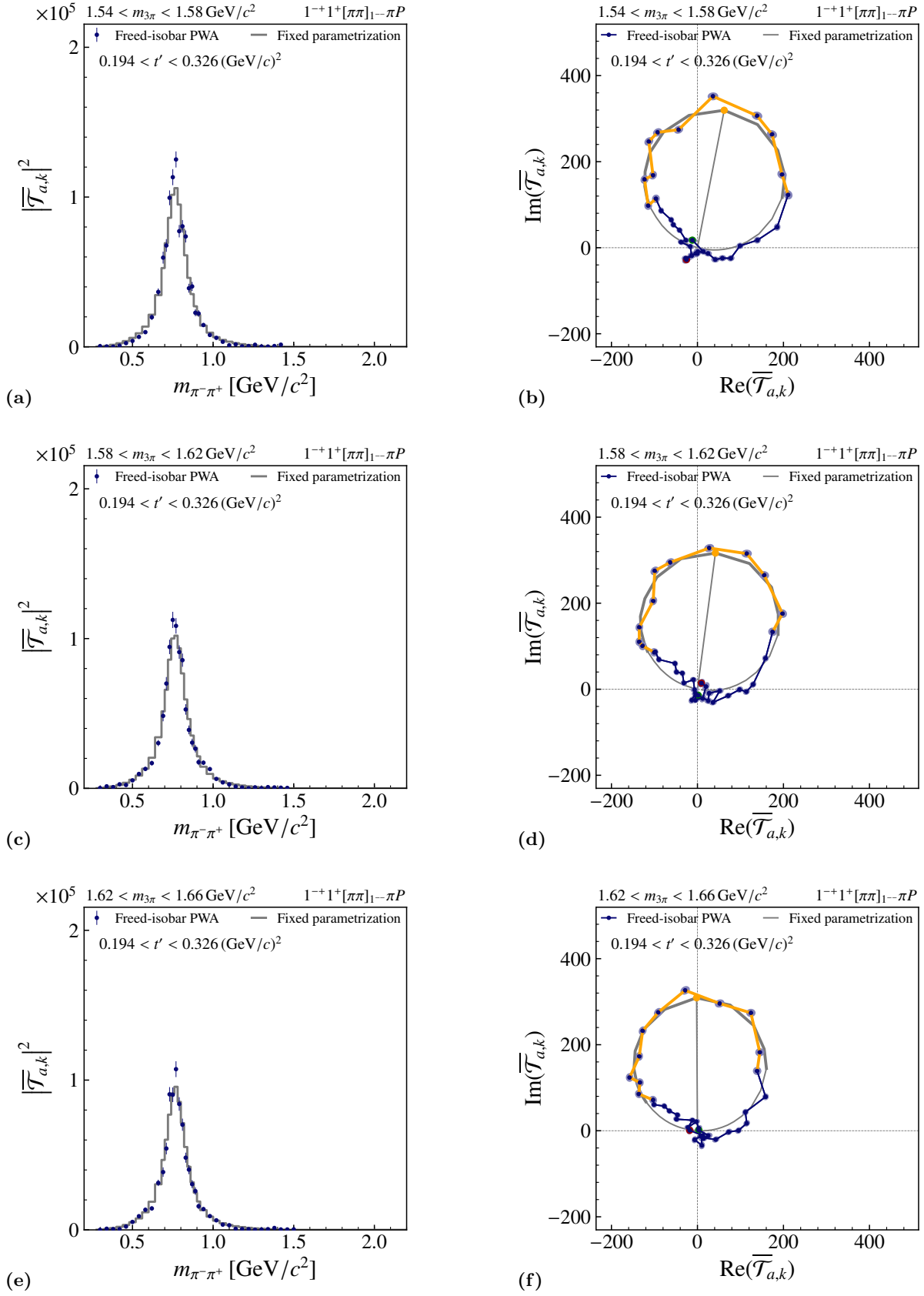
FIG. 35: Intensity distribution and Argand diagrams similar to Fig. 6 for $1.54 < m_{3\pi} < 1.66\,\mathrm{GeV}/c^2$ and $0.141 < t' < 0.194\,(\mathrm{GeV}/c)^2$.

FIG. 36: Intensity distribution and Argand diagrams similar to Fig. 6 for $1.66 < m_{3\pi} < 1.78\,\mathrm{GeV}/c^2$ and $0.141 < t' < 0.194\,(\mathrm{GeV}/c)^2$.

FIG. 37: Intensity distribution and Argand diagrams similar to Fig. 6 for $1.78 < m_{3\pi} < 1.90\,\mathrm{GeV}/c^2$ and $0.141 < t' < 0.194\,(\mathrm{GeV}/c)^2$.

$\times 10^5$ $1.90 < m_{3\pi} < 1.94\,\mathrm{GeV}/c^2$ $1^{-+}1^+[\pi\pi]_{1^{--}}\pi P$

(a)

$1.90 < m_{3\pi} < 1.94\,\mathrm{GeV}/c^2$ $1^{-+}1^+[\pi\pi]_{1^{--}}\pi P$

(b)

$\times 10^5$ $1.94 < m_{3\pi} < 1.98\,\mathrm{GeV}/c^2$ $1^{-+}1^+[\pi\pi]_{1^{--}}\pi P$

(c)

$1.94 < m_{3\pi} < 1.98\,\mathrm{GeV}/c^2$ $1^{-+}1^+[\pi\pi]_{1^{--}}\pi P$

(d)

$\times 10^5$ $1.98 < m_{3\pi} < 2.02\,\mathrm{GeV}/c^2$ $1^{-+}1^+[\pi\pi]_{1^{--}}\pi P$

(e)

$1.98 < m_{3\pi} < 2.02\,\mathrm{GeV}/c^2$ $1^{-+}1^+[\pi\pi]_{1^{--}}\pi P$

(f)

FIG. 38: Intensity distribution and Argand diagrams similar to Fig. 6 for $1.90 < m_{3\pi} < 2.02\,\mathrm{GeV}/c^2$ and $0.141 < t' < 0.194\,(\mathrm{GeV}/c)^2$.

FIG. 39: Intensity distribution and Argand diagrams similar to Fig. 6 for $2.02 < m_{3\pi} < 2.14\,\mathrm{GeV}/c^2$ and $0.141 < t' < 0.194\,(\mathrm{GeV}/c)^2$.

FIG. 40: Intensity distribution and Argand diagrams similar to Fig. 6 for $2.14 < m_{3\pi} < 2.26\,\mathrm{GeV}/c^2$ and $0.141 < t' < 0.194\,(\mathrm{GeV}/c)^2$.

FIG. 41: Intensity distribution and Argand diagrams similar to Fig. 6 for $2.26 < m_{3\pi} < 2.38\,\mathrm{GeV}/c^2$ and $0.141 < t' < 0.194\,(\mathrm{GeV}/c)^2$.

FIG. 42: Intensity distribution and Argand diagrams similar to Fig. 6 for $2.38 < m_{3\pi} < 2.50\,\mathrm{GeV}/c^2$ and $0.141 < t' < 0.194\,(\mathrm{GeV}/c)^2$.

3 $[\pi\pi]_{1^{--}}$ dynamic isobar amplitude for $0.194 < t' < 0.326\,(\mathrm{GeV}/c)^2$
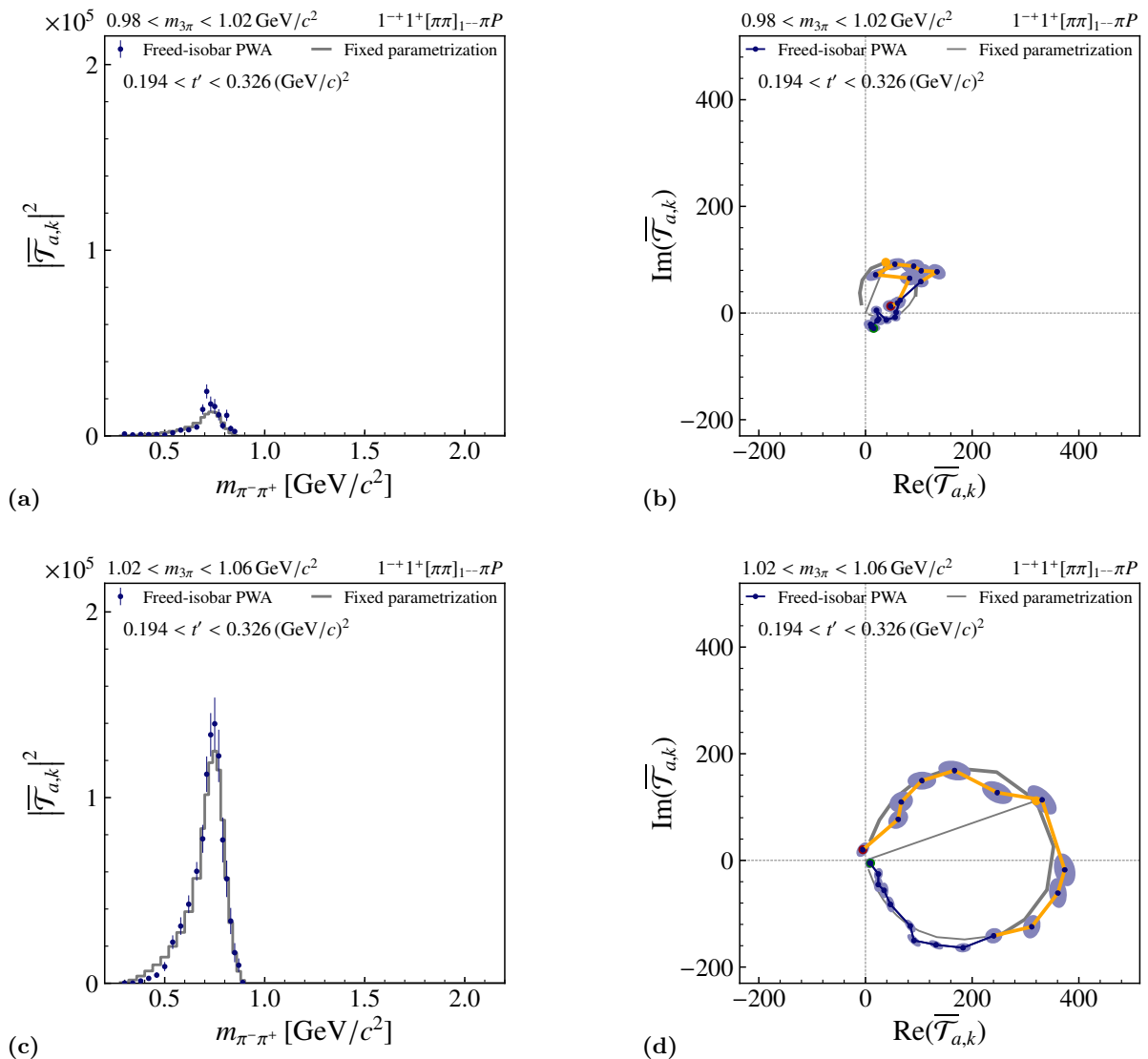
FIG. 43: Intensity distributions and Argand diagrams similar to Fig. 6 for $0.98 < m_{3\pi} < 1.06\,\mathrm{GeV}/c^2$ and $0.194 < t' < 0.326\,(\mathrm{GeV}/c)^2$.
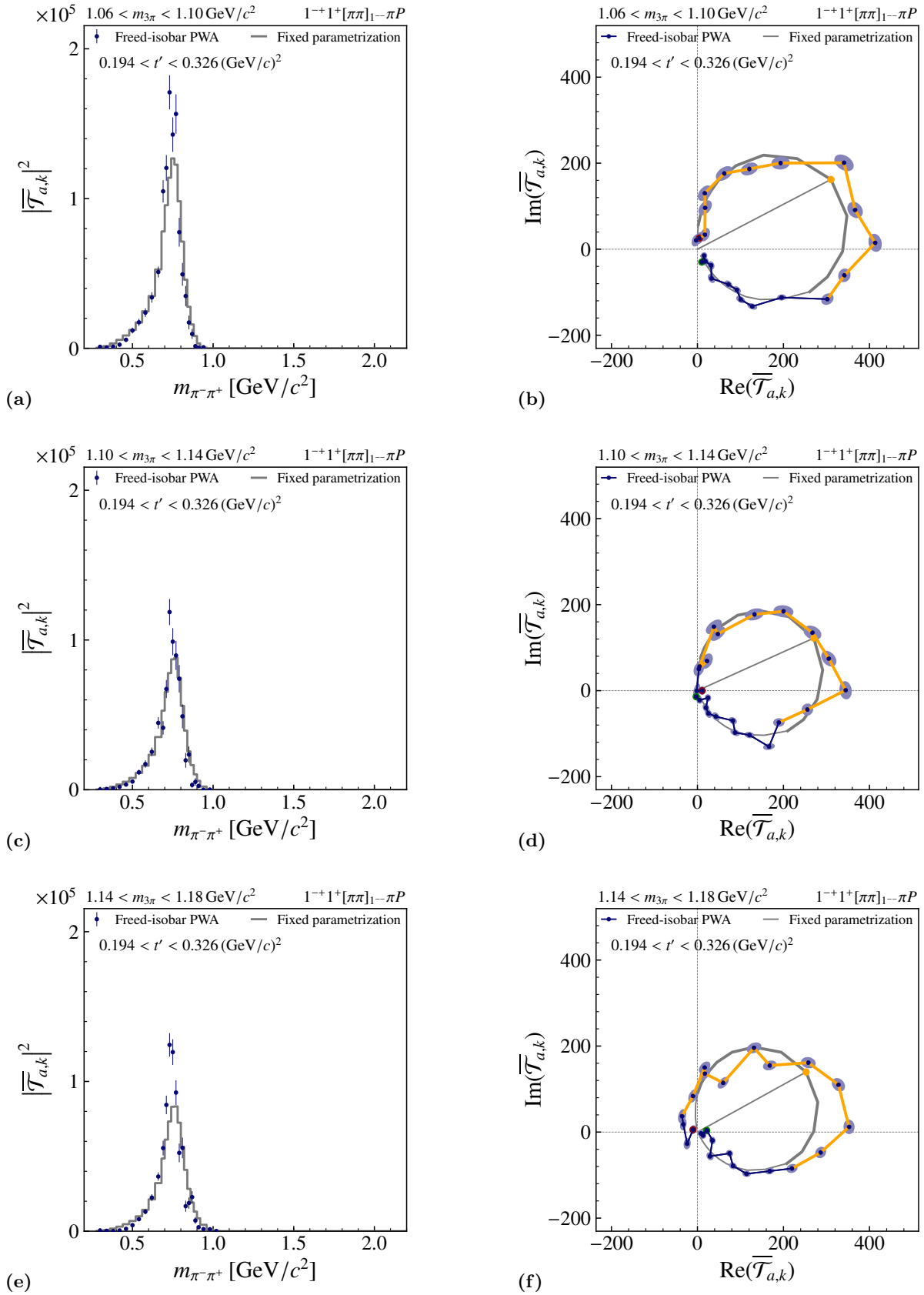
FIG. 44: Intensity distribution and Argand diagrams similar to Fig. 6 for $1.06 < m_{3\pi} < 1.18\,\text{GeV}/c^2$ and $0.194 < t' < 0.326\,(\text{GeV}/c)^2$.
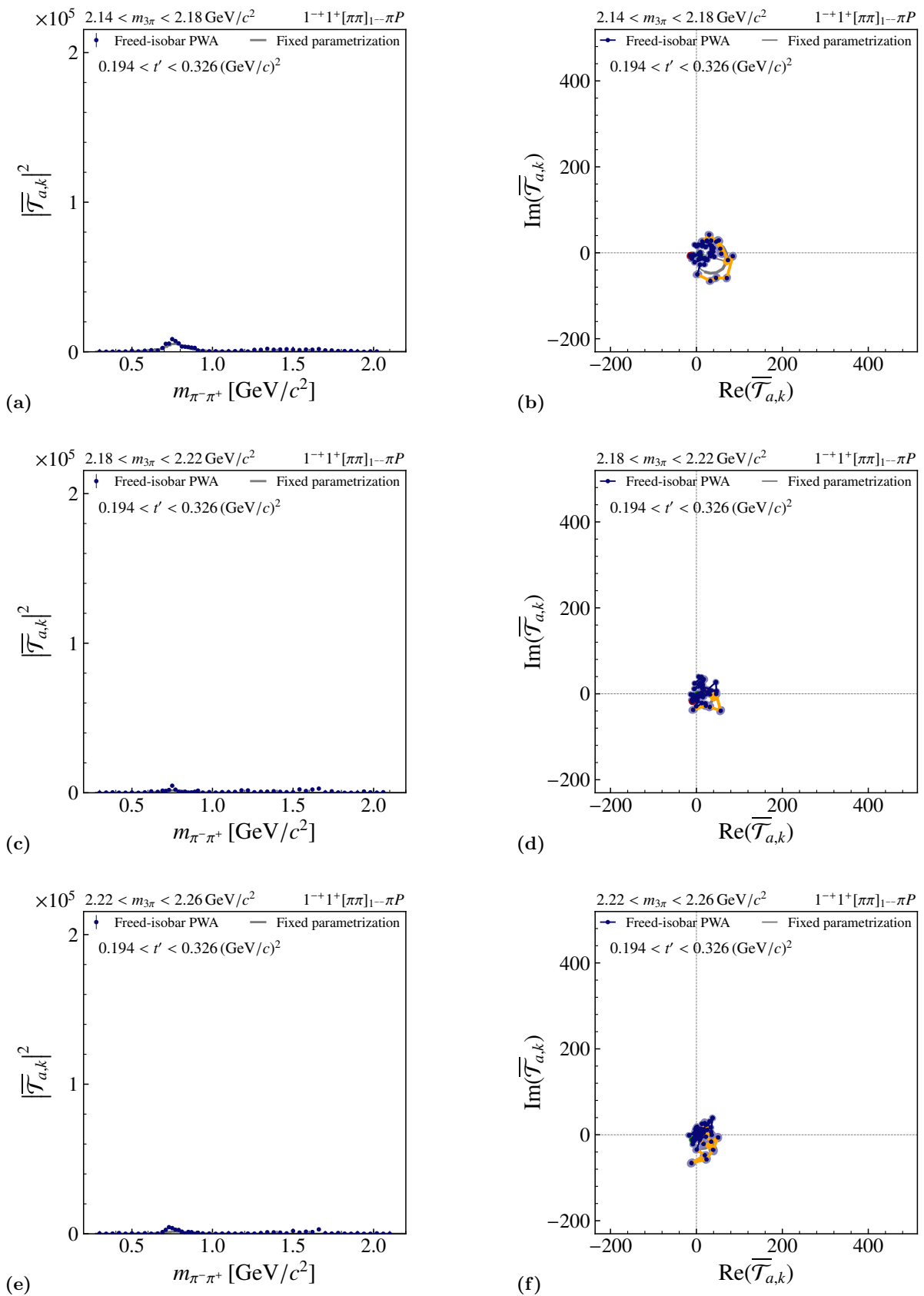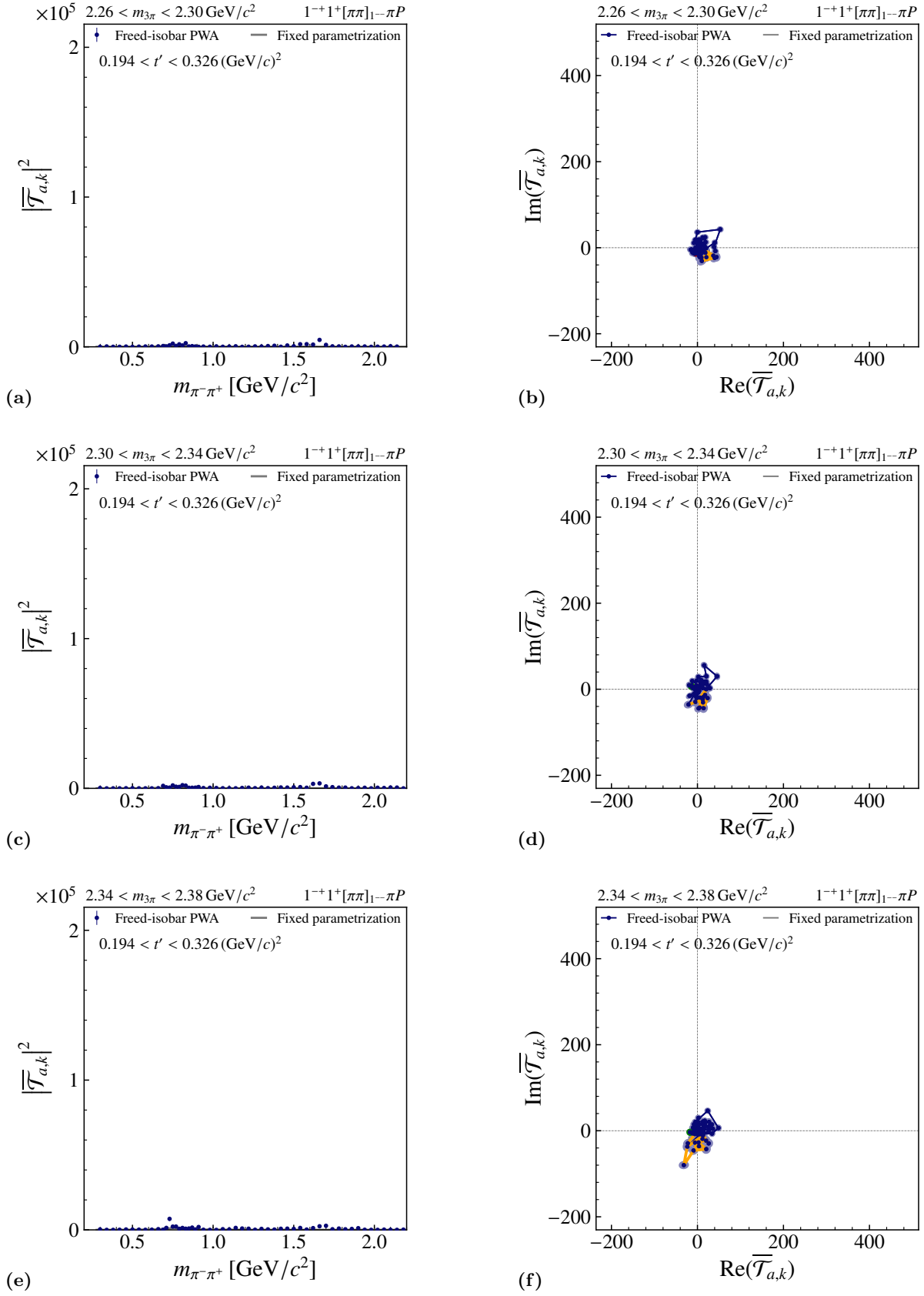
FIG. 45: Intensity distribution and Argand diagrams similar to Fig. 6 for $1.18 < m_{3\pi} < 1.30\,\mathrm{GeV}/c^2$ and $0.194 < t' < 0.326\,(\mathrm{GeV}/c)^2$.

FIG. 46: Intensity distribution and Argand diagrams similar to Fig. 6 for $1.30 < m_{3\pi} < 1.42\,\text{GeV}/c^2$ and $0.194 < t' < 0.326\,(\text{GeV}/c)^2$.
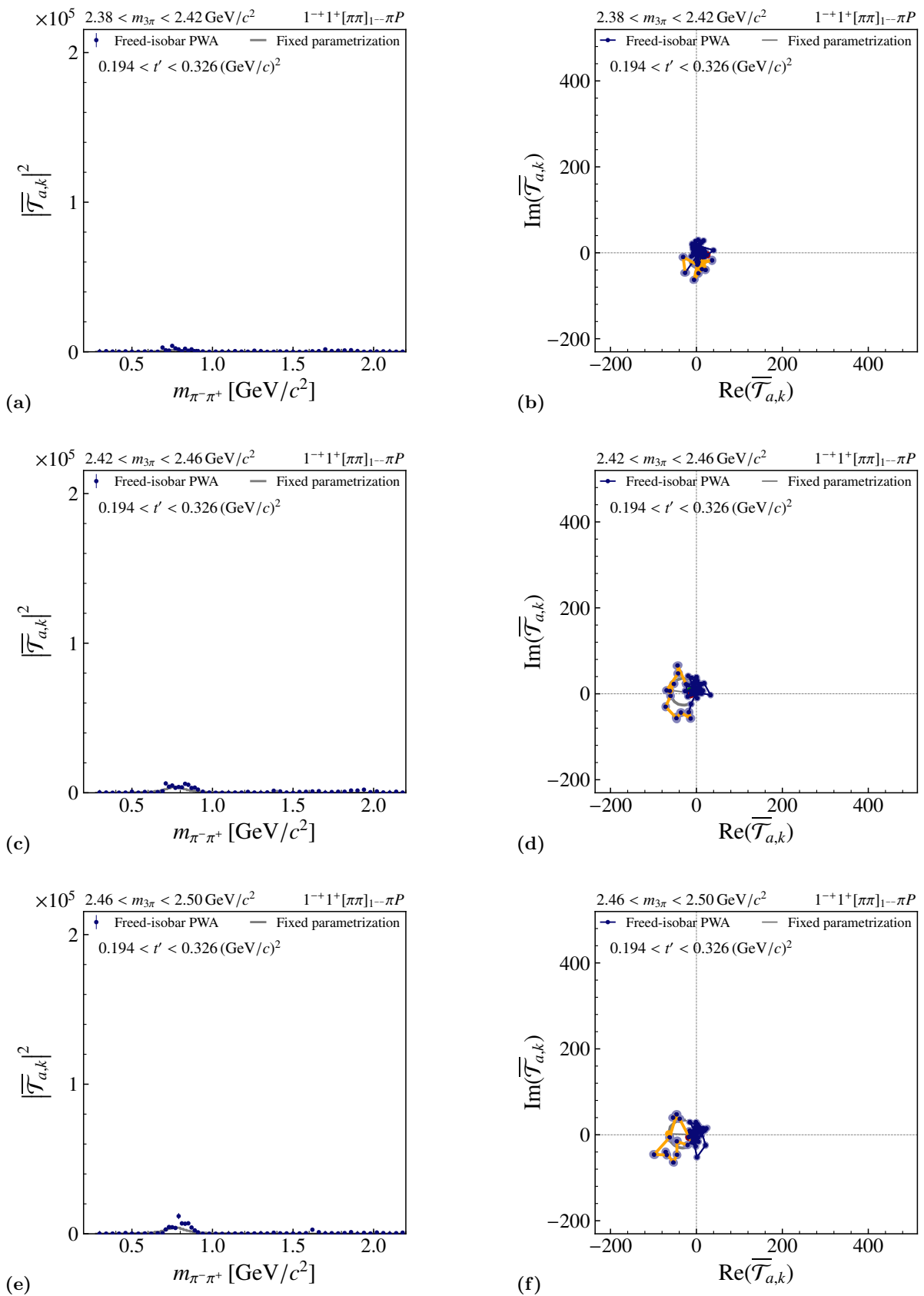
FIG. 47: Intensity distribution and Argand diagrams similar to Fig. 6 for $1.42 < m_{3\pi} < 1.54\,\mathrm{GeV}/c^2$ and $0.194 < t' < 0.326\,(\mathrm{GeV}/c)^2$.

FIG. 48: Intensity distribution and Argand diagrams similar to Fig. 6 for $1.54 < m_{3\pi} < 1.66\,\mathrm{GeV}/c^2$ and $0.194 < t' < 0.326\,(\mathrm{GeV}/c)^2$.
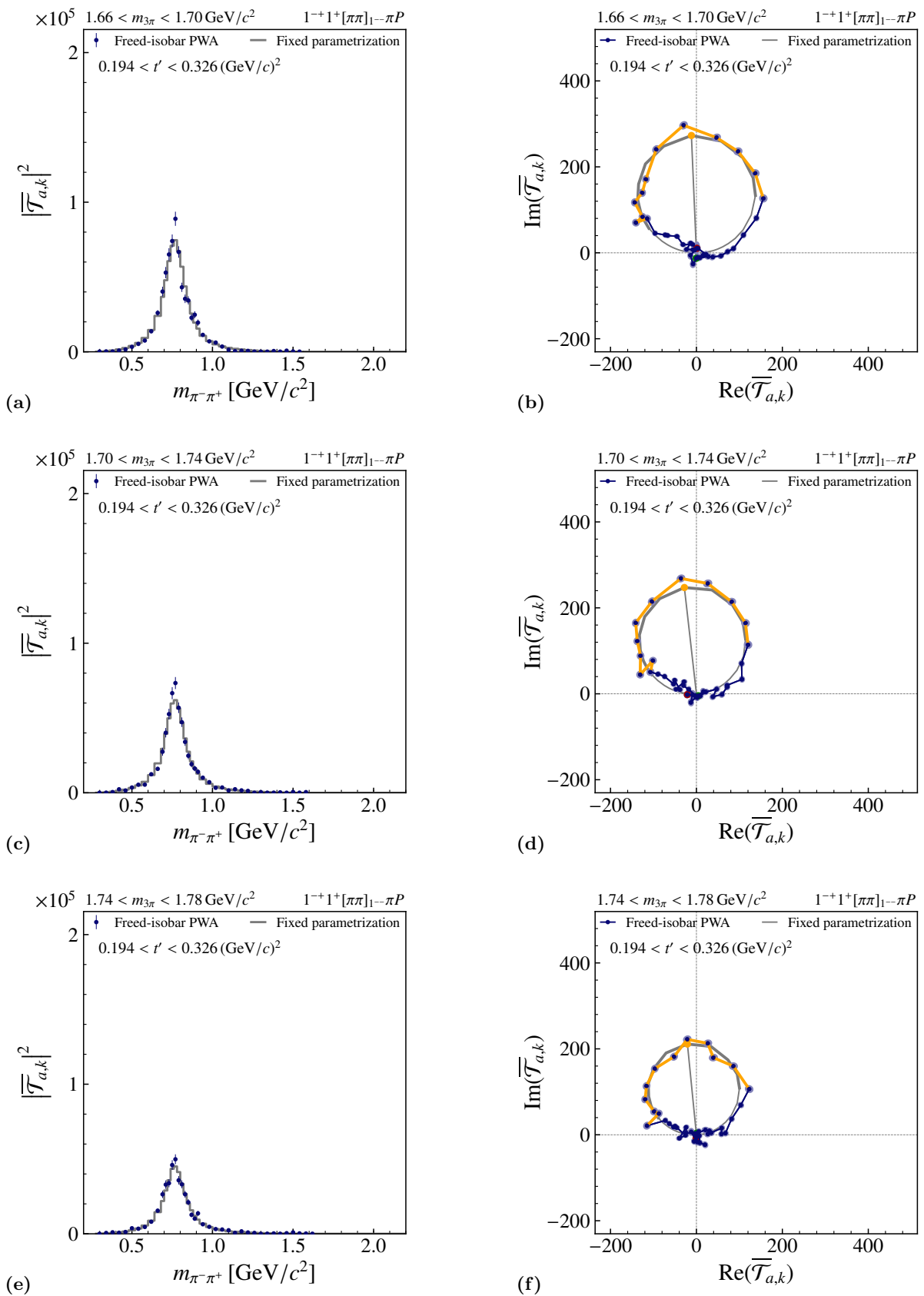
FIG. 49: Intensity distribution and Argand diagrams similar to Fig. 6 for $1.66 < m_{3\pi} < 1.78\,\text{GeV}/c^2$ and $0.194 < t' < 0.326\,(\text{GeV}/c)^2$.
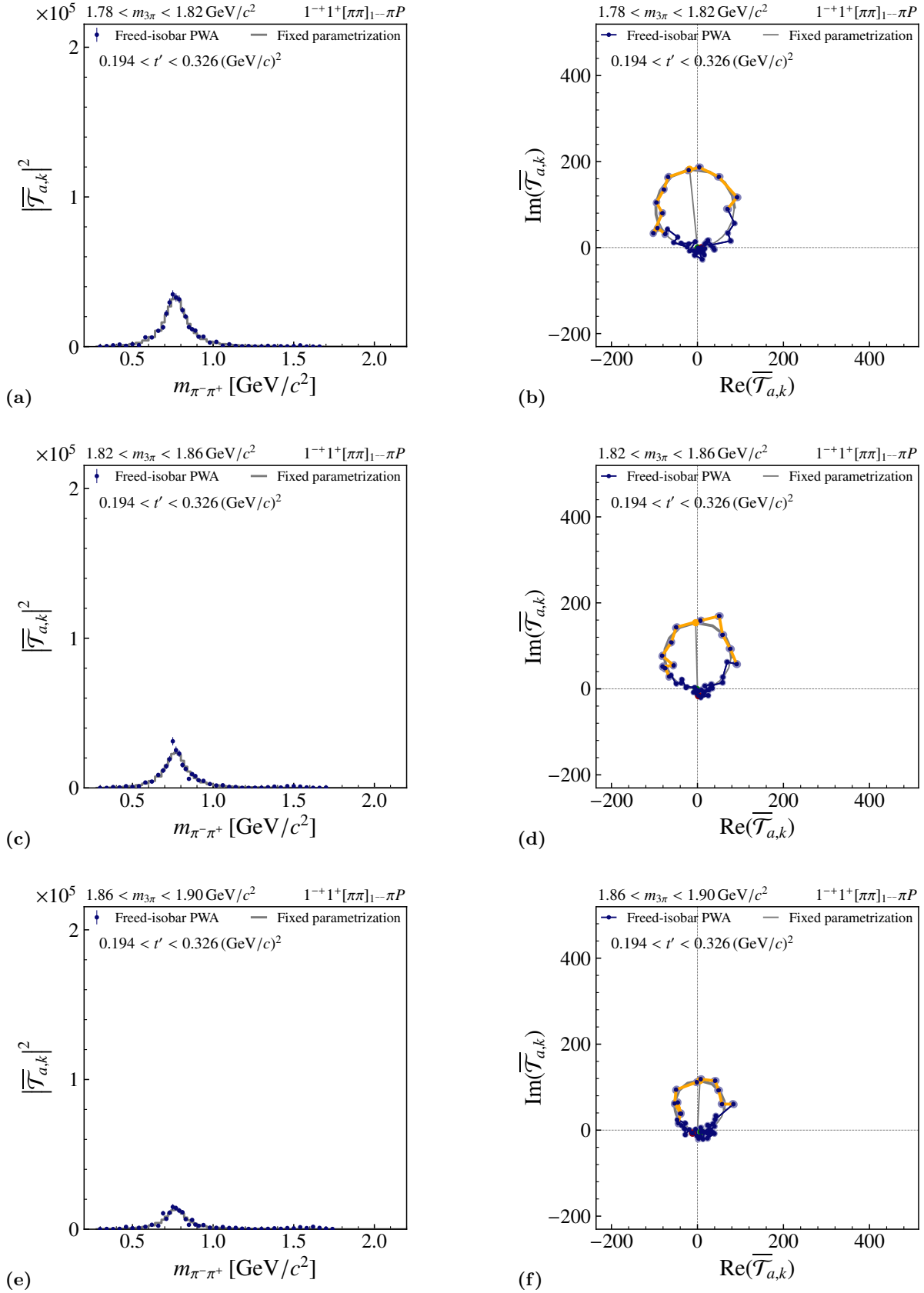
FIG. 50: Intensity distribution and Argand diagrams similar to Fig. 6 for $1.78 < m_{3\pi} < 1.90\,\text{GeV}/c^2$ and $0.194 < t' < 0.326\,(\text{GeV}/c)^2$.
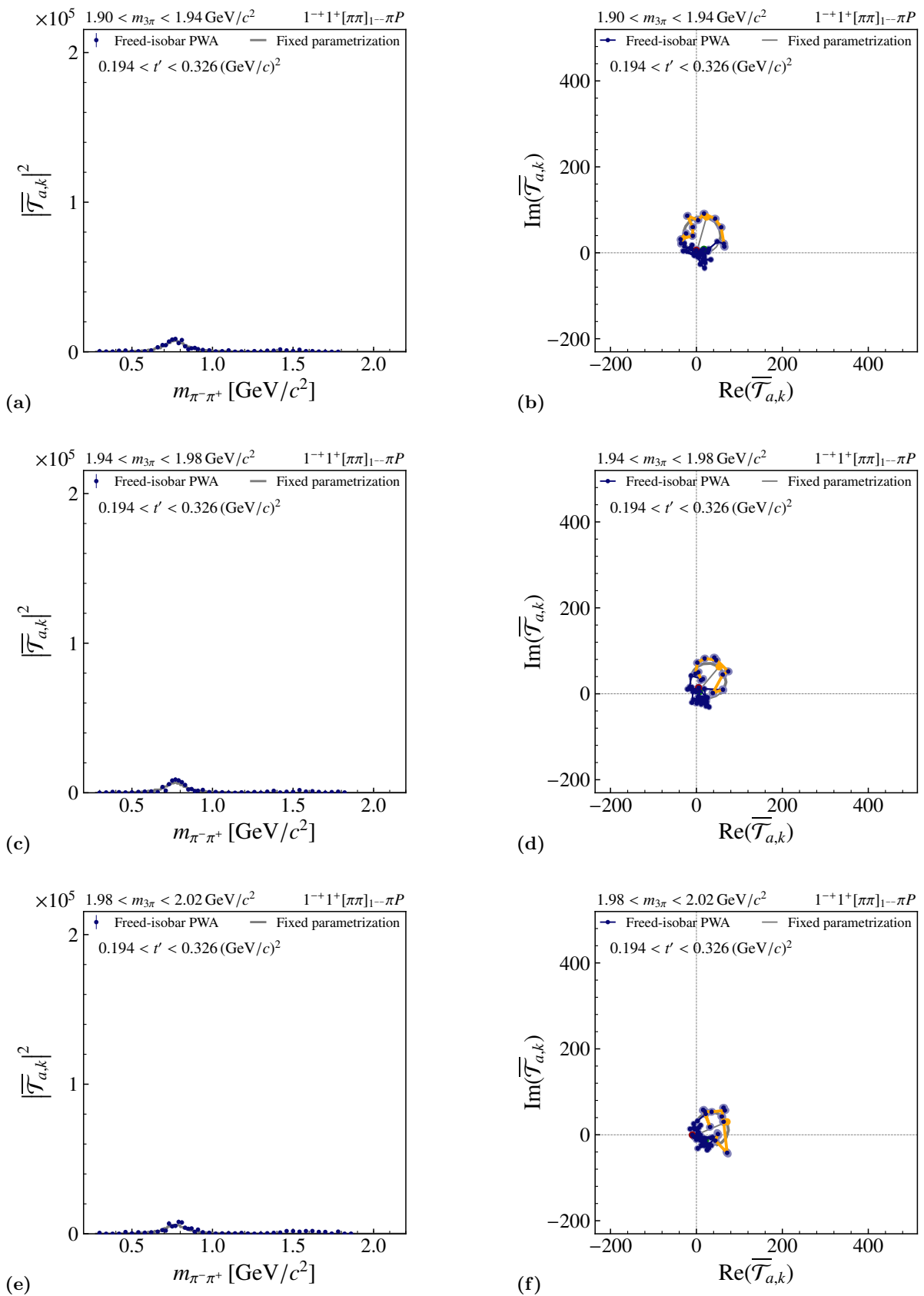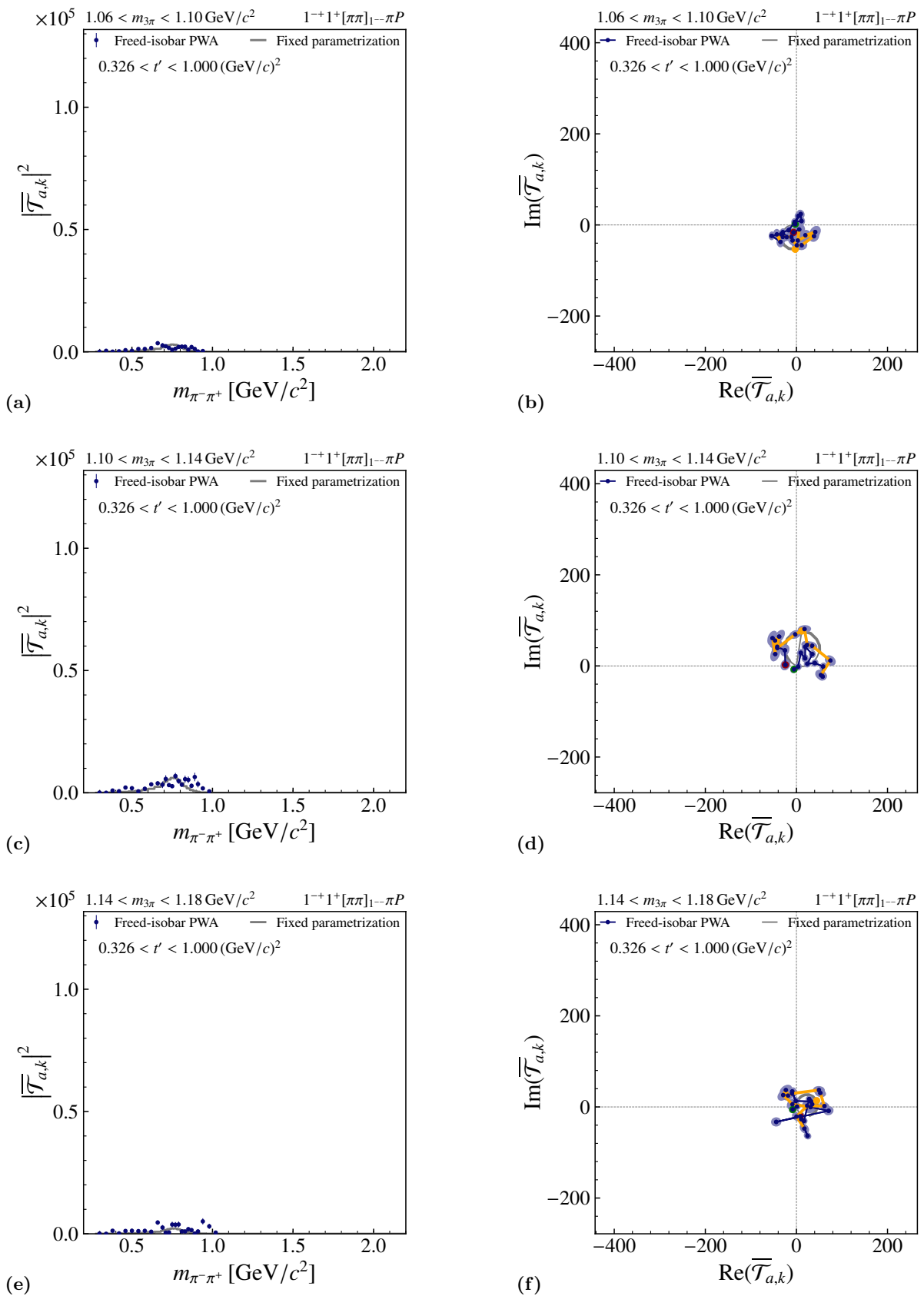
FIG. 51: Intensity distribution and Argand diagrams similar to Fig. 6 for $1.90 < m_{3\pi} < 2.02\,\text{GeV}/c^2$ and $0.194 < t' < 0.326\,(\text{GeV}/c)^2$.
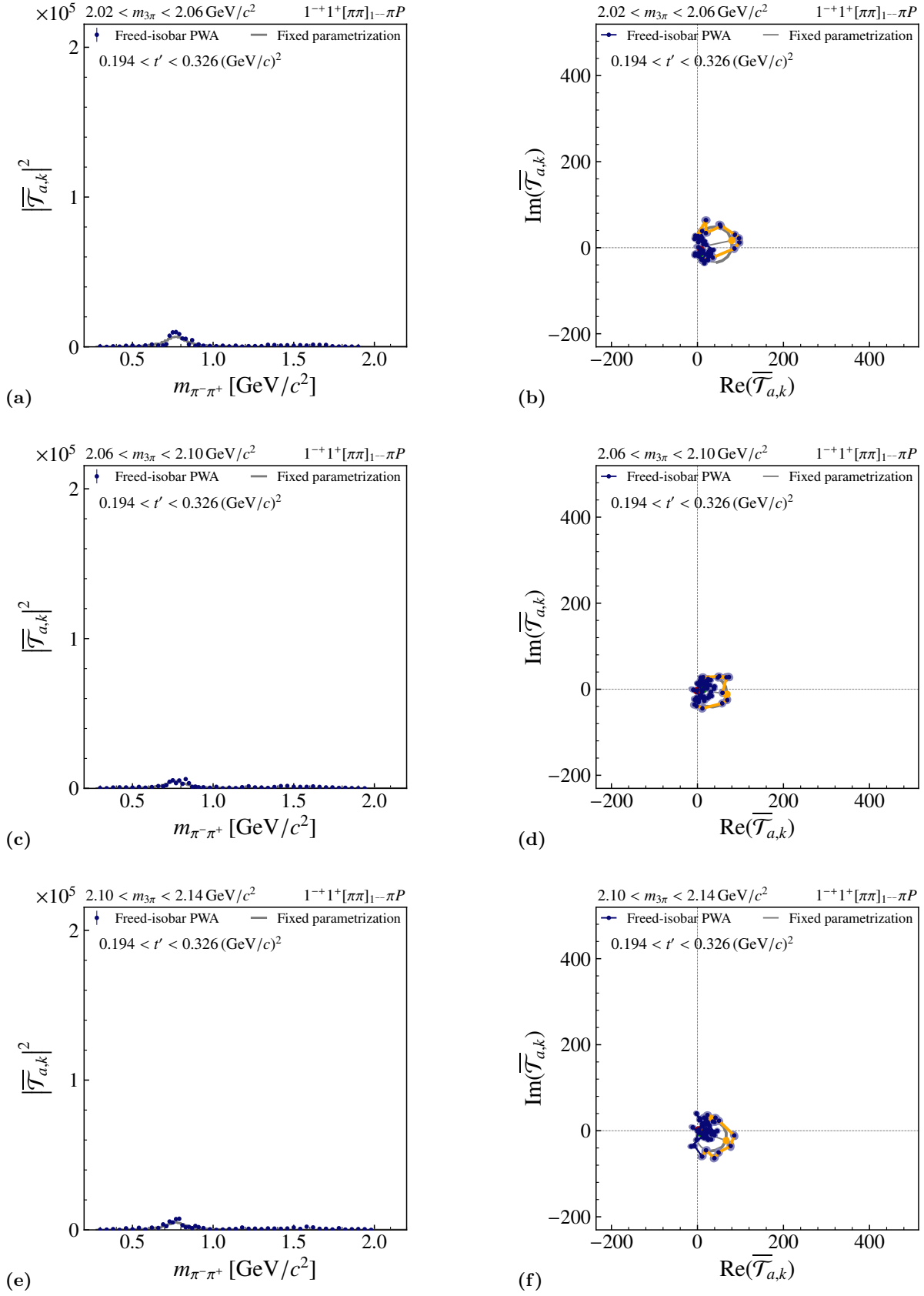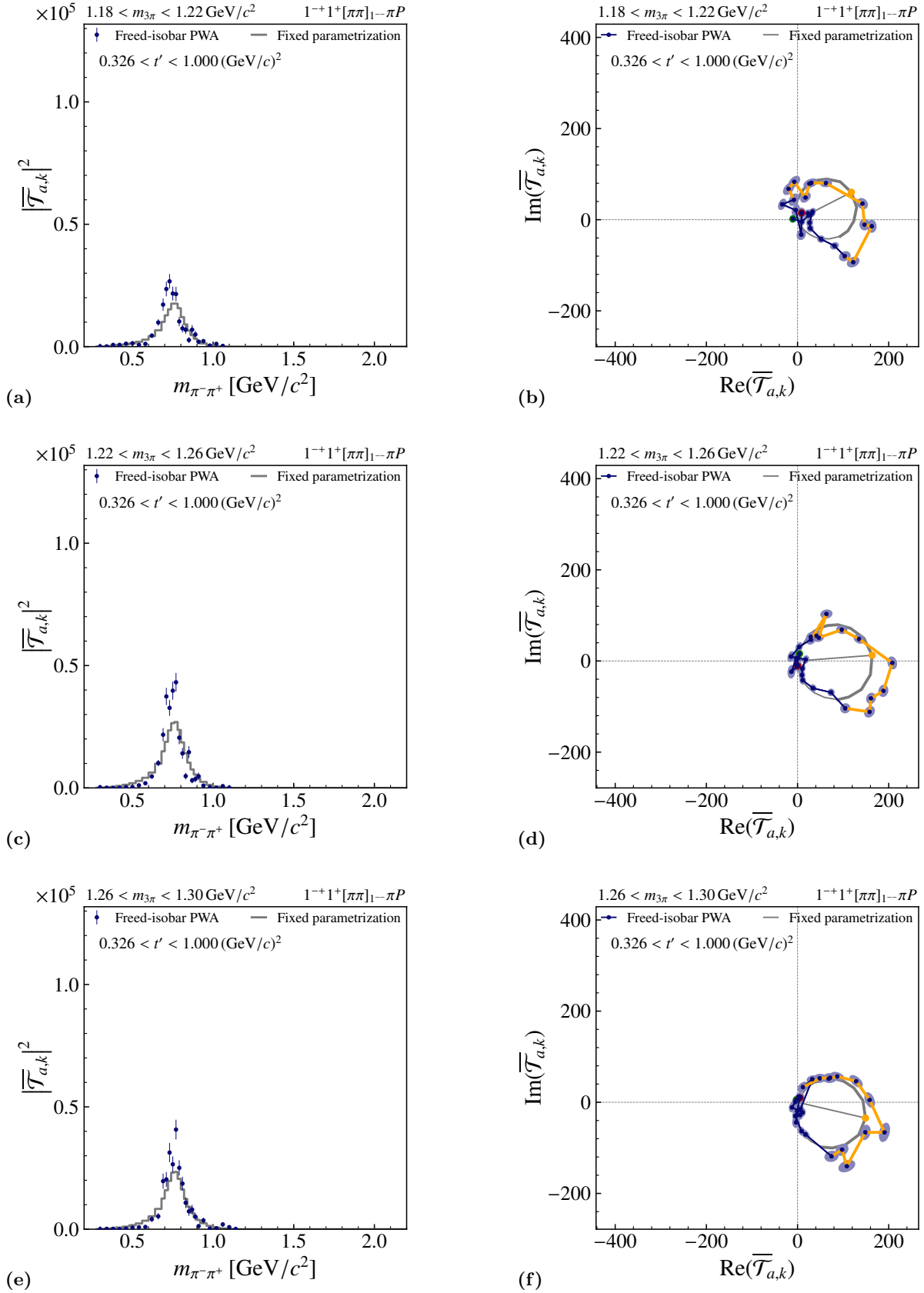
FIG. 52: Intensity distribution and Argand diagrams similar to Fig. 6 for $2.02 < m_{3\pi} < 2.14 \, \text{GeV}/c^2$ and $0.194 < t' < 0.326 \, (\text{GeV}/c)^2$.

FIG. 53: Intensity distribution and Argand diagrams similar to Fig. 6 for $2.14 < m_{3\pi} < 2.26\,\text{GeV}/c^2$ and $0.194 < t' < 0.326\,(\text{GeV}/c)^2$.

FIG. 54: Intensity distribution and Argand diagrams similar to Fig. 6 for $2.26 < m_{3\pi} < 2.38\,\text{GeV}/c^2$ and $0.194 < t' < 0.326\,(\text{GeV}/c)^2$.
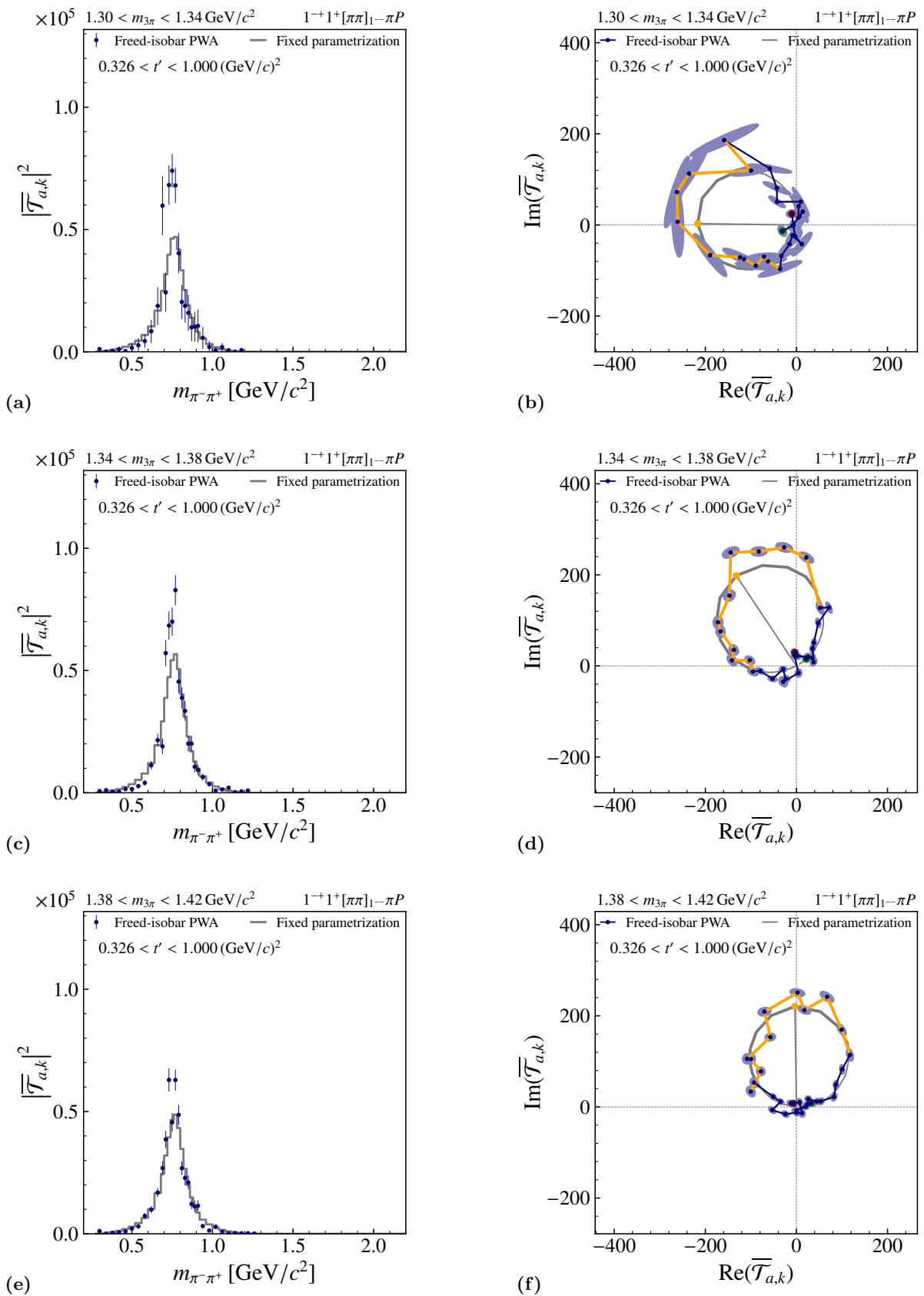
FIG. 55: Intensity distribution and Argand diagrams similar to Fig. 6 for $2.38 < m_{3\pi} < 2.50\,\mathrm{GeV}/c^2$ and $0.194 < t' < 0.326\,(\mathrm{GeV}/c)^2$.

4 $[\pi\pi]_{1^{--}}$ dynamic isobar amplitude for $0.326 < t' < 1.000 \, (\mathrm{GeV}/c)^2$
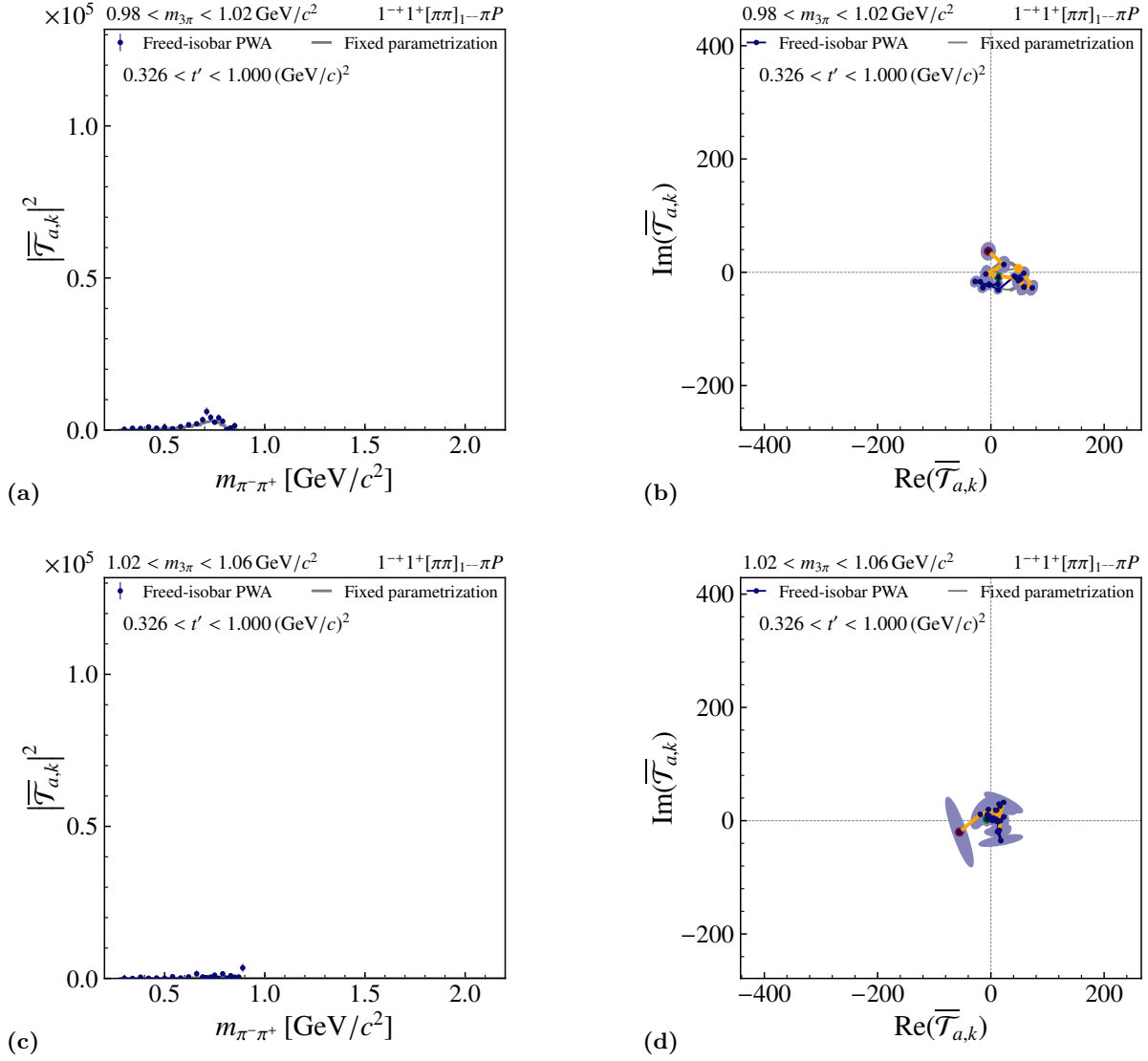
FIG. 56: Intensity distributions and Argand diagrams similar to Fig. 6 for $0.98 < m_{3\pi} < 1.06 \, \mathrm{GeV}/c^2$ and $0.326 < t' < 1.000 \, (\mathrm{GeV}/c)^2$.

FIG. 57: Intensity distribution and Argand diagrams similar to Fig. 6 for $1.06 < m_{3\pi} < 1.18\,\mathrm{GeV}/c^2$ and $0.326 < t' < 1.000\,(\mathrm{GeV}/c)^2$.

FIG. 58: Intensity distribution and Argand diagrams similar to Fig. 6 for $1.18 < m_{3\pi} < 1.30 \, \text{GeV}/c^2$ and $0.326 < t' < 1.000 \, (\text{GeV}/c)^2$.
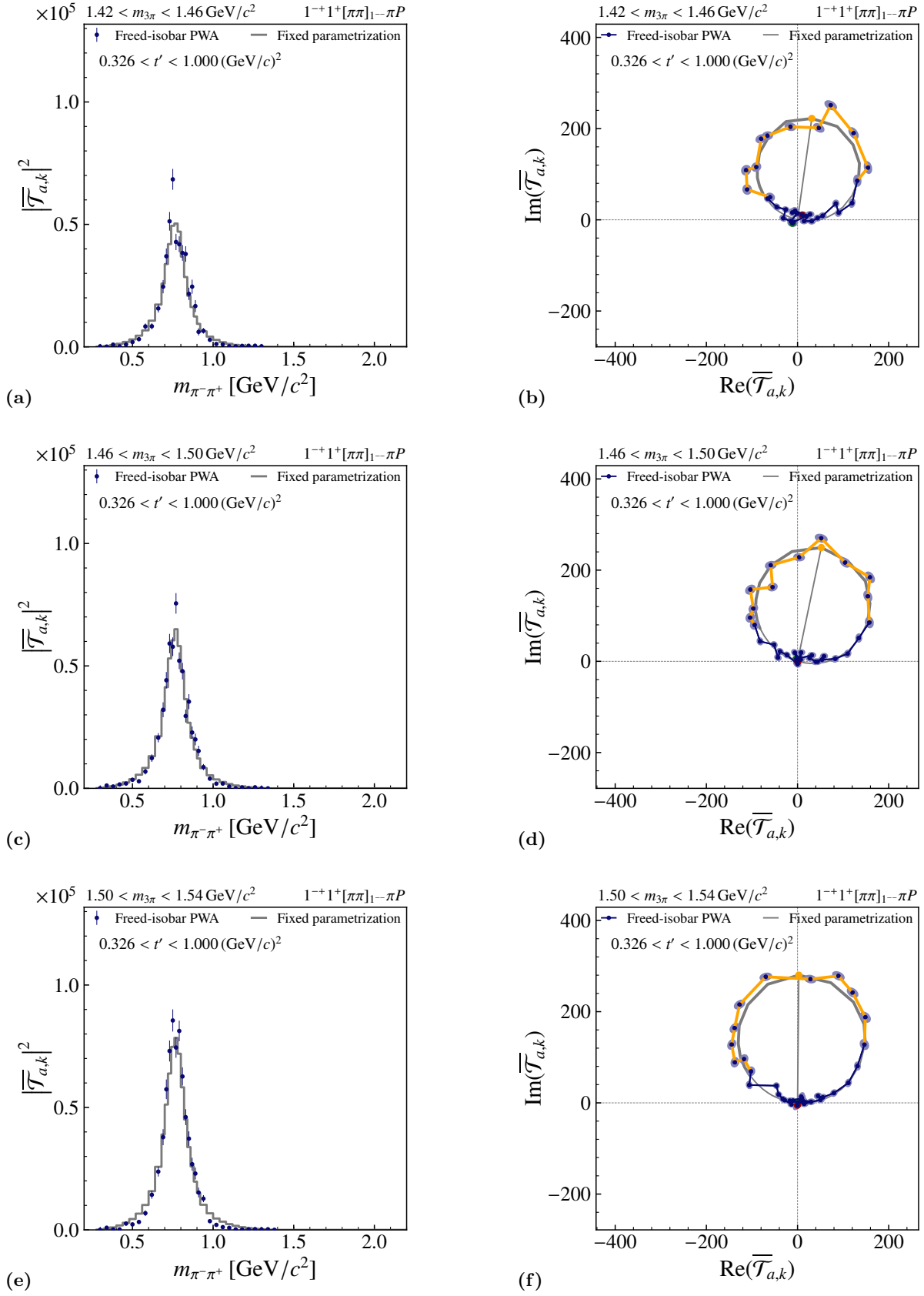
FIG. 59: Intensity distribution and Argand diagrams similar to Fig. 6 for $1.30 < m_{3\pi} < 1.42\,\text{GeV}/c^2$ and $0.326 < t' < 1.000\,(\text{GeV}/c)^2$.
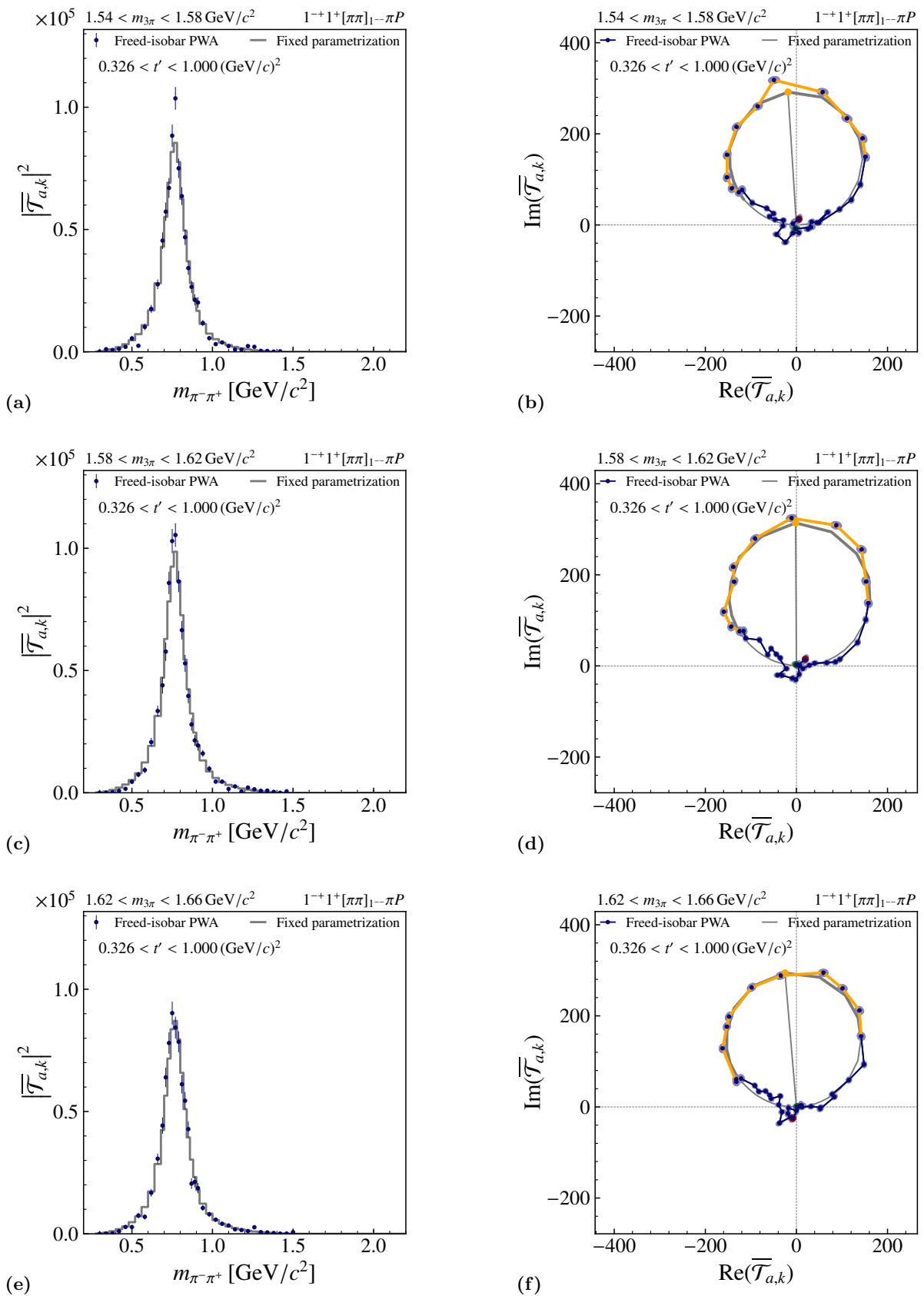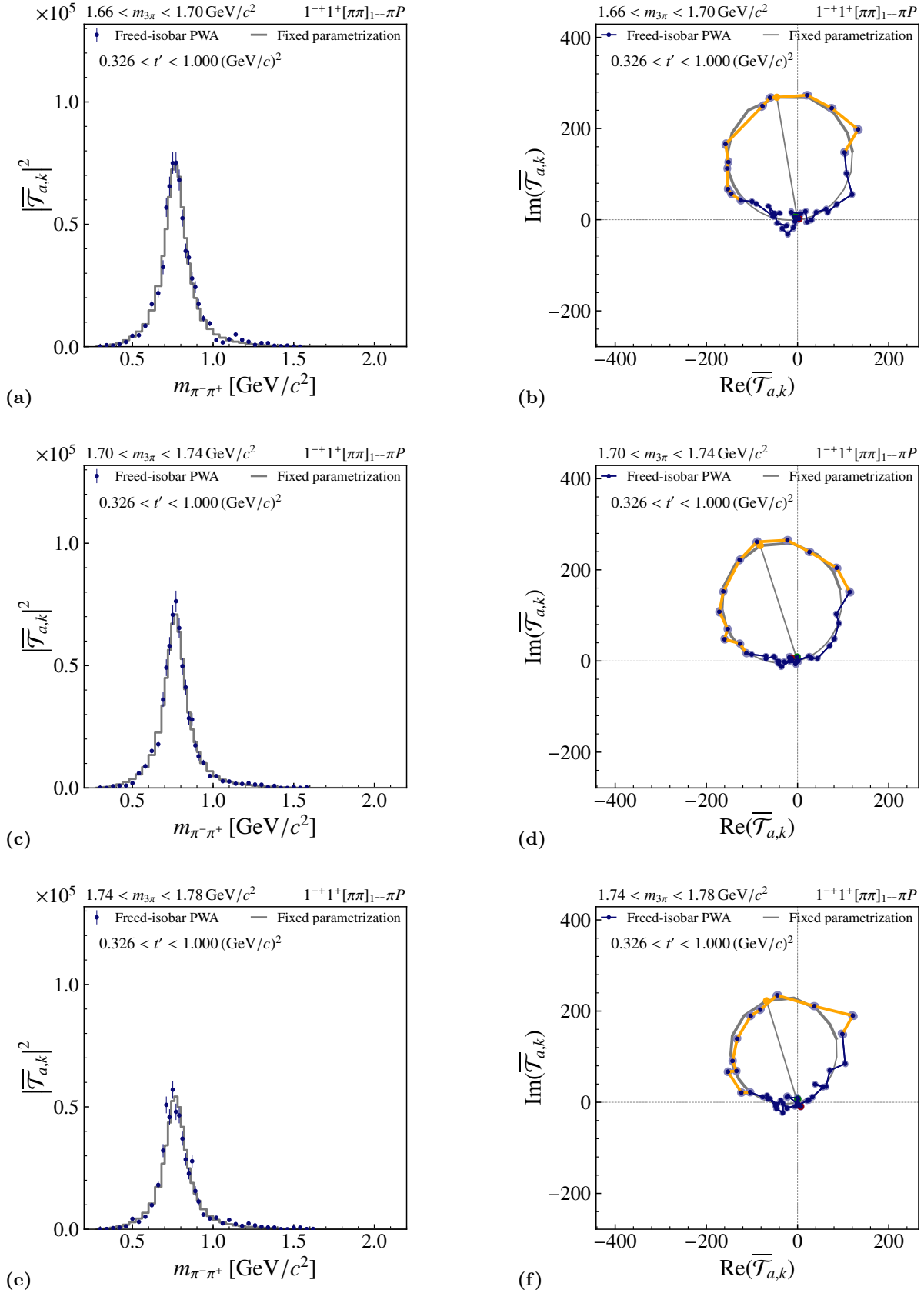
FIG. 60: Intensity distribution and Argand diagrams similar to Fig. 6 for $1.42 < m_{3\pi} < 1.54 \, \text{GeV}/c^2$ and $0.326 < t' < 1.000 \, (\text{GeV}/c)^2$.

FIG. 61: Intensity distribution and Argand diagrams similar to Fig. 6 for $1.54 < m_{3\pi} < 1.66\,\mathrm{GeV}/c^2$ and $0.326 < t' < 1.000\,(\mathrm{GeV}/c)^2$.

FIG. 62: Intensity distribution and Argand diagrams similar to Fig. 6 for $1.66 < m_{3\pi} < 1.78\,\text{GeV}/c^2$ and $0.326 < t' < 1.000\,(\text{GeV}/c)^2$.
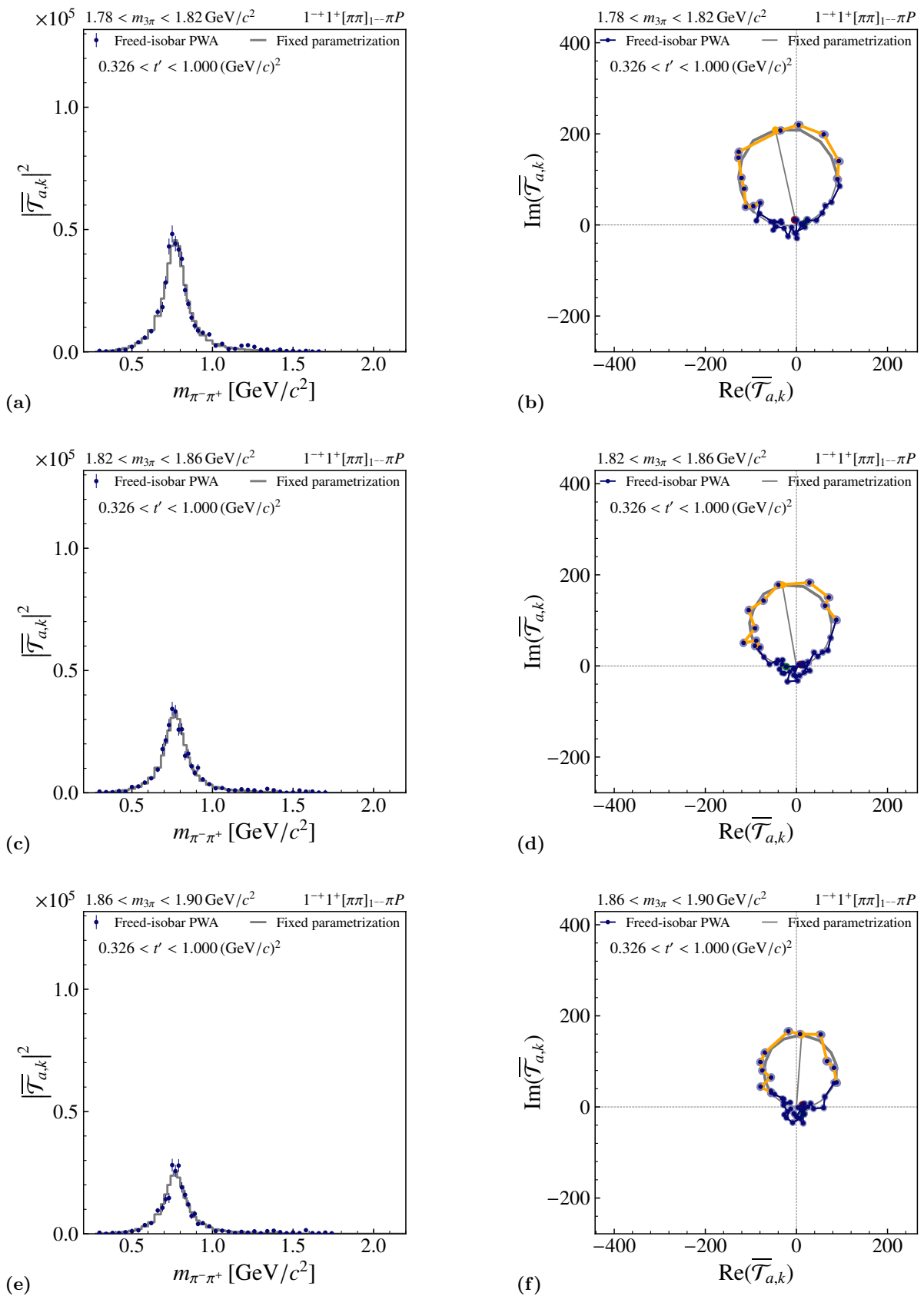
FIG. 63: Intensity distribution and Argand diagrams similar to Fig. 6 for $1.78 < m_{3\pi} < 1.90\,\mathrm{GeV}/c^2$ and $0.326 < t' < 1.000\,(\mathrm{GeV}/c)^2$.

FIG. 64: Intensity distribution and Argand diagrams similar to Fig. 6 for $1.90 < m_{3\pi} < 2.02\,\text{GeV}/c^2$ and $0.326 < t' < 1.000\,(\text{GeV}/c)^2$.
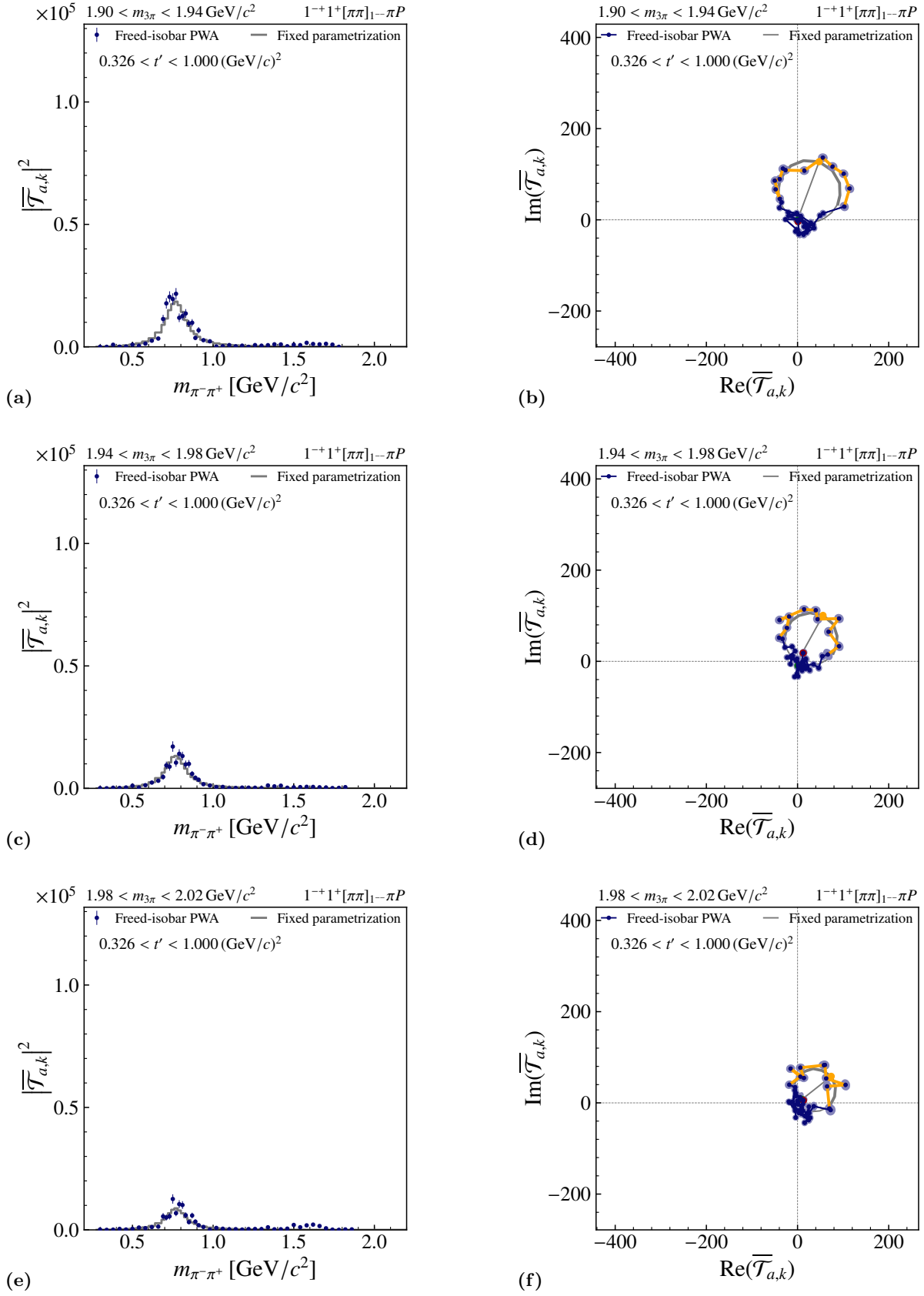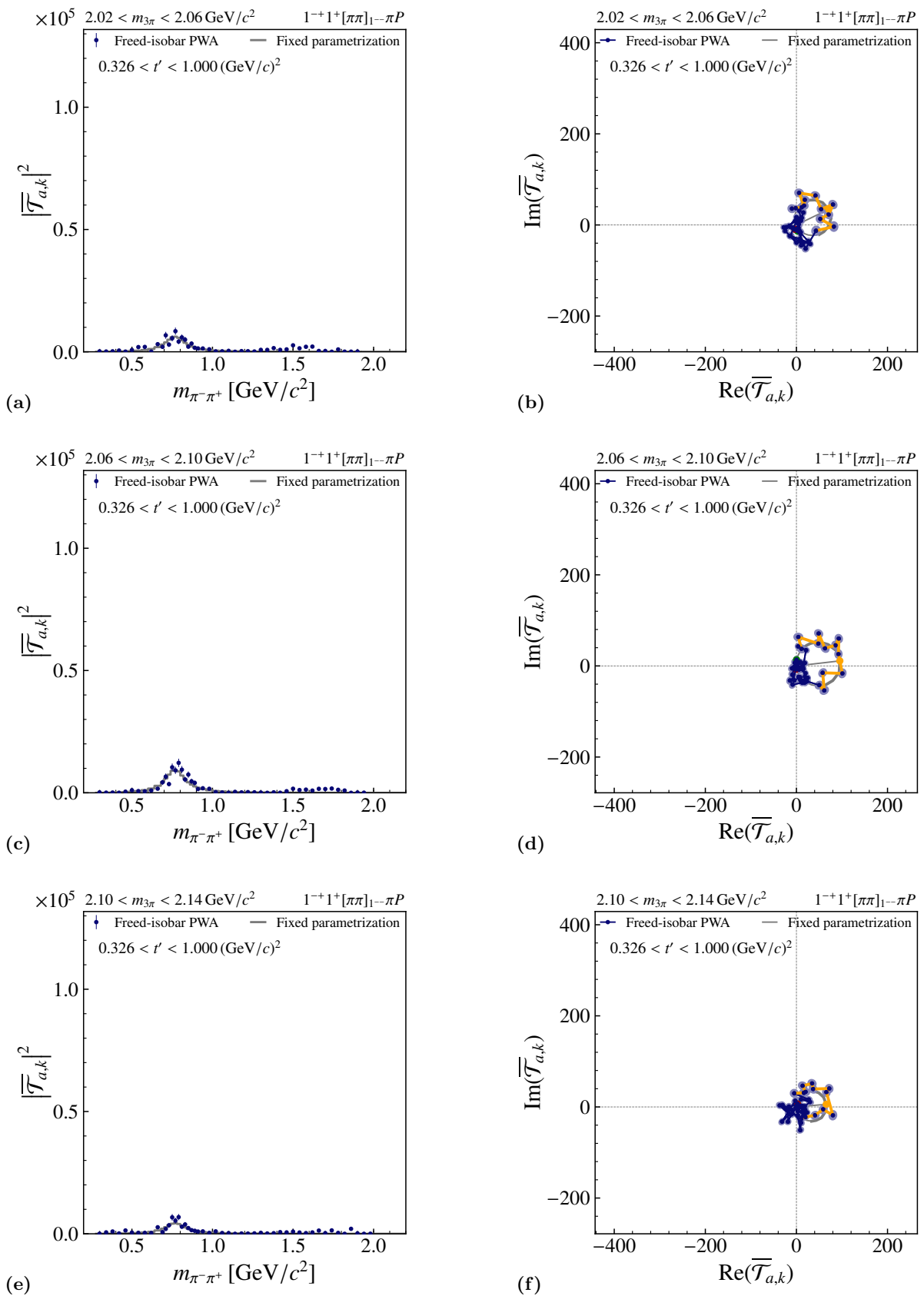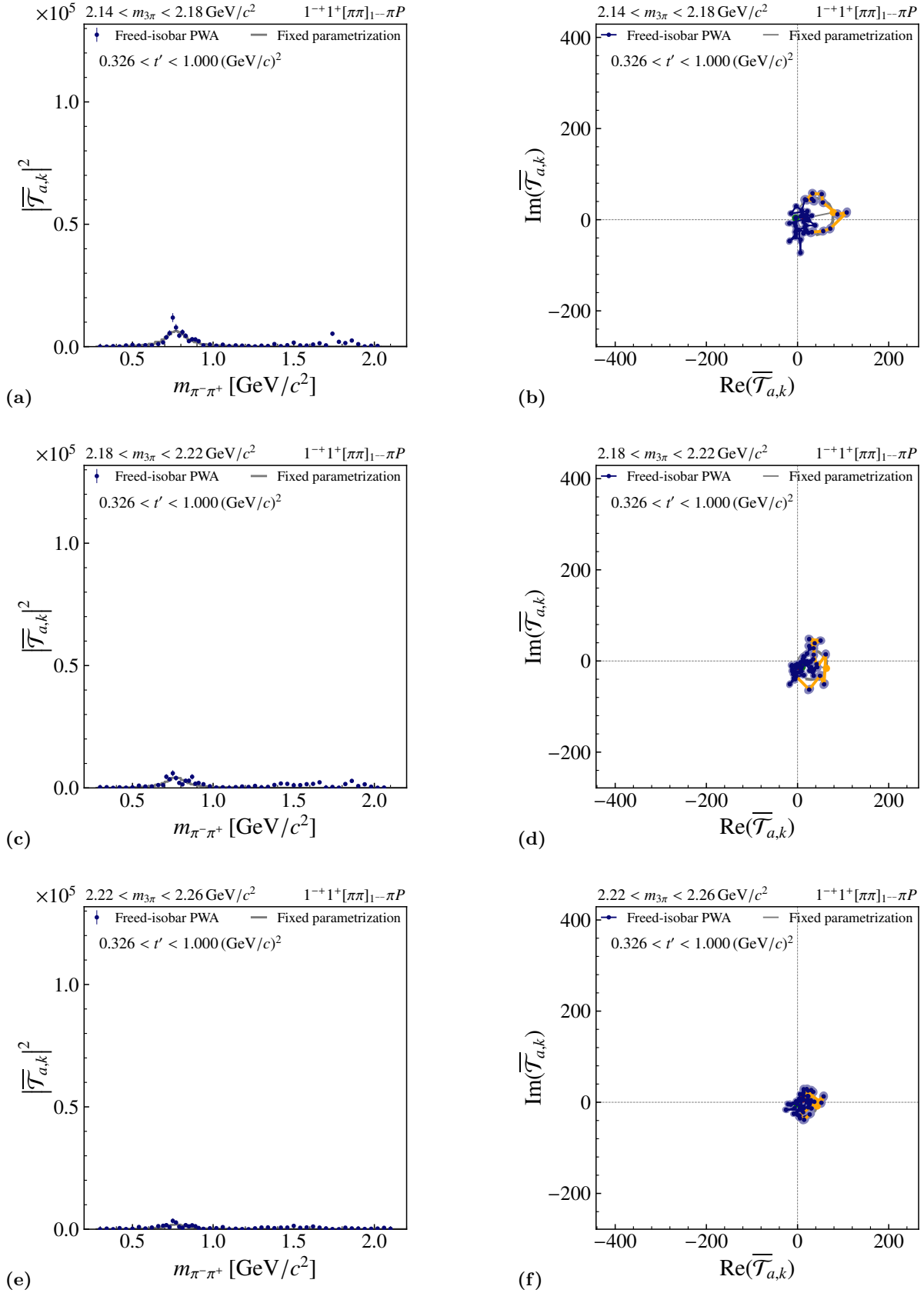
FIG. 65: Intensity distribution and Argand diagrams similar to Fig. 6 for $2.02 < m_{3\pi} < 2.14\,\mathrm{GeV}/c^2$ and $0.326 < t' < 1.000\,(\mathrm{GeV}/c)^2$.

FIG. 66: Intensity distribution and Argand diagrams similar to Fig. 6 for $2.14 < m_{3\pi} < 2.26\,\mathrm{GeV}/c^2$ and $0.326 < t' < 1.000\,(\mathrm{GeV}/c)^2$.

FIG. 67: Intensity distribution and Argand diagrams similar to Fig. 6 for $2.26 < m_{3\pi} < 2.38\,\mathrm{GeV}/c^2$ and $0.326 < t' < 1.000\,(\mathrm{GeV}/c)^2$.

$\times 10^5$ $2.38 < m_{3\pi} < 2.42\,\text{GeV}/c^2$ $1^{-+}1^+[\pi\pi]_{1^{--}}\pi P$

(a)

$2.38 < m_{3\pi} < 2.42\,\text{GeV}/c^2$ $1^{-+}1^+[\pi\pi]_{1^{--}}\pi P$

(b)

$\times 10^5$ $2.42 < m_{3\pi} < 2.46\,\text{GeV}/c^2$ $1^{-+}1^+[\pi\pi]_{1^{--}}\pi P$

(c)

$2.42 < m_{3\pi} < 2.46\,\text{GeV}/c^2$ $1^{-+}1^+[\pi\pi]_{1^{--}}\pi P$

(d)

$\times 10^5$ $2.46 < m_{3\pi} < 2.50\,\text{GeV}/c^2$ $1^{-+}1^+[\pi\pi]_{1^{--}}\pi P$

(e)

$2.46 < m_{3\pi} < 2.50\,\text{GeV}/c^2$ $1^{-+}1^+[\pi\pi]_{1^{--}}\pi P$

(f)

FIG. 68: Intensity distribution and Argand diagrams similar to Fig. 6 for $2.38 < m_{3\pi} < 2.50\,\text{GeV}/c^2$ and $0.326 <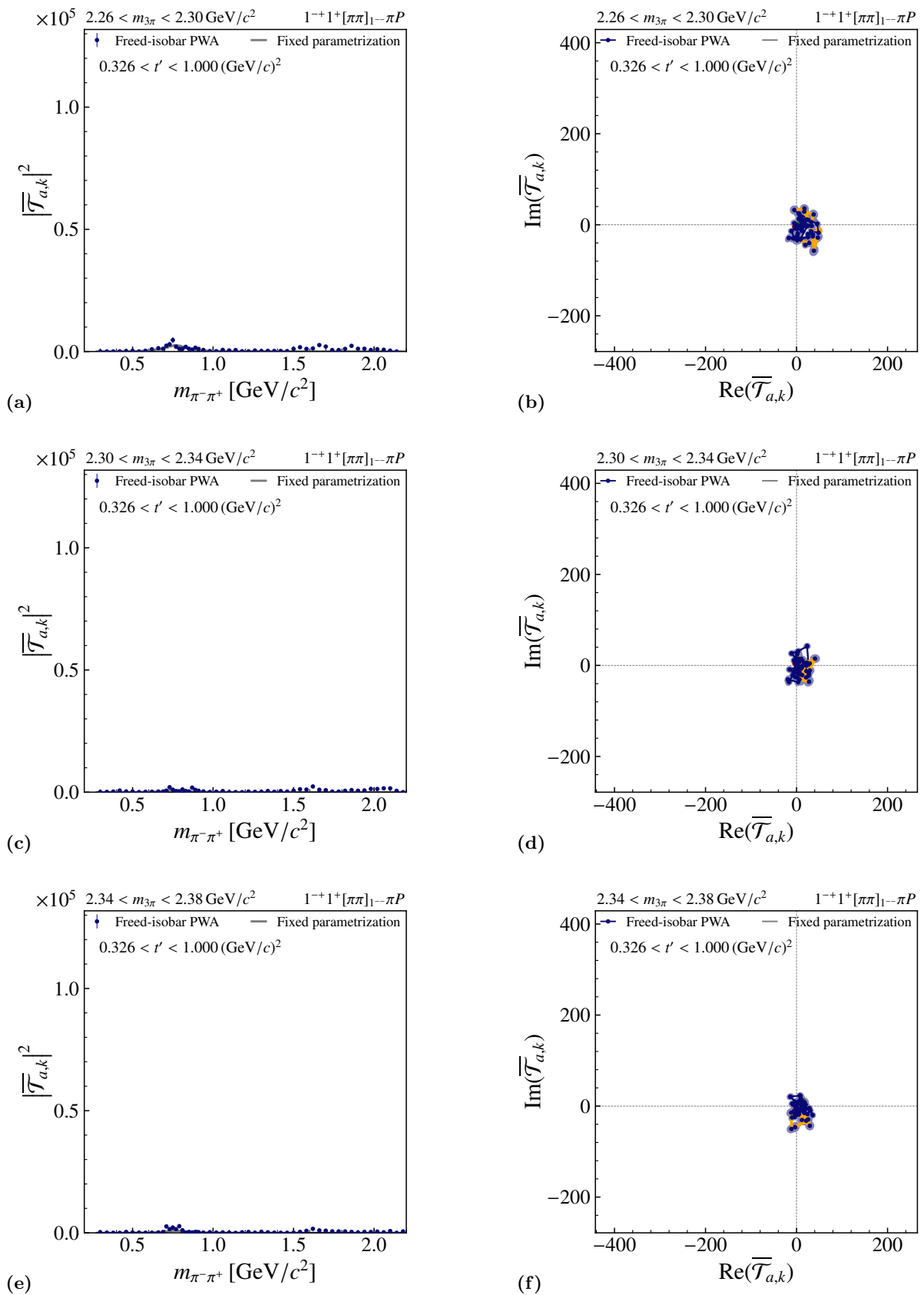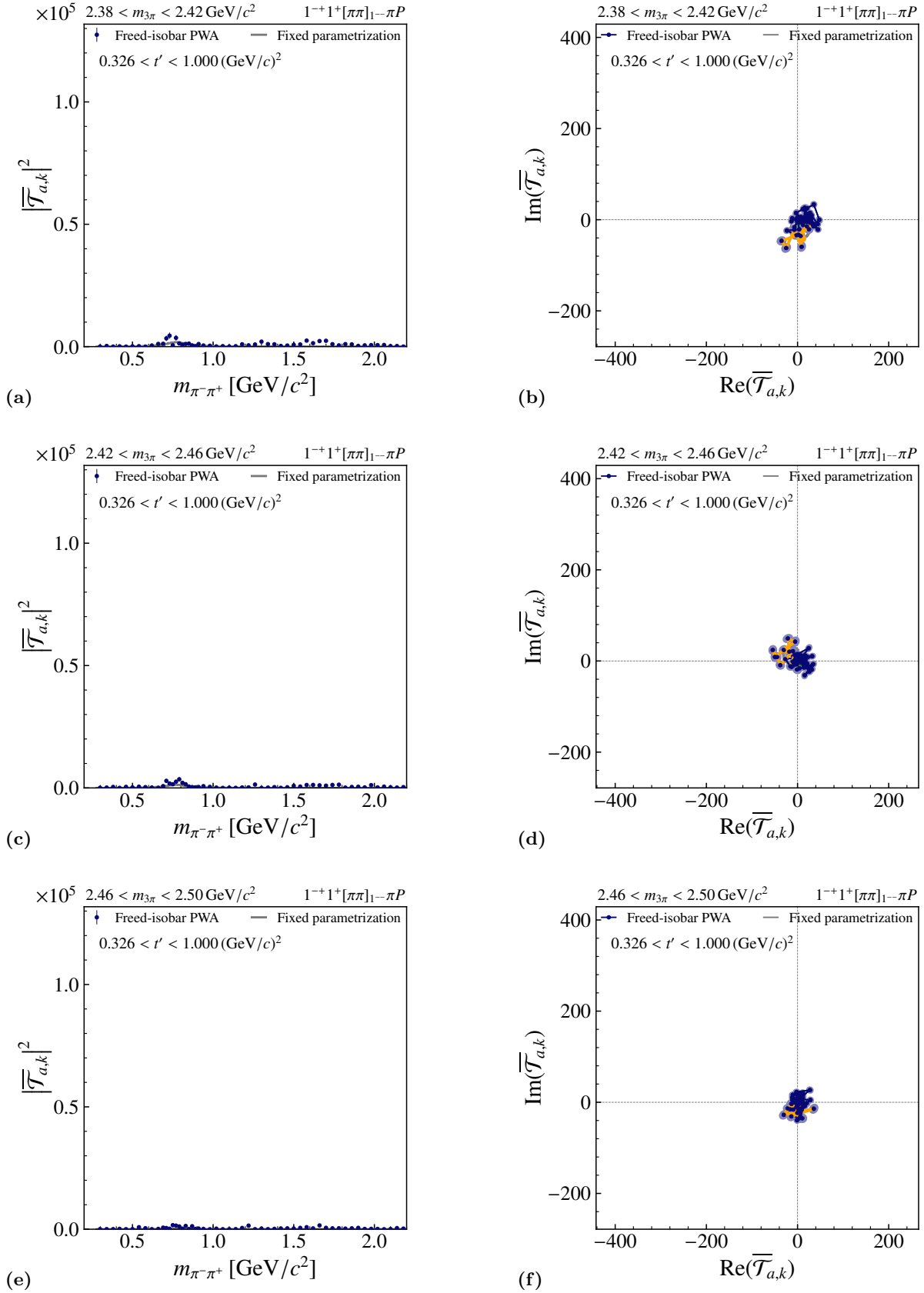 t' < 1.000\,(\text{GeV}/c)^2$.